



HAL
open science

Modeling of the negative ion extraction from a hydrogen plasma source : application to ITER neutral beam injector

Serhiy Mochalskyy

► **To cite this version:**

Serhiy Mochalskyy. Modeling of the negative ion extraction from a hydrogen plasma source : application to ITER neutral beam injector. Other [cond-mat.other]. Université Paris Sud - Paris XI, 2011. English. NNT : 2011PA112351 . tel-00672140

HAL Id: tel-00672140

<https://theses.hal.science/tel-00672140>

Submitted on 20 Feb 2012

HAL is a multi-disciplinary open access archive for the deposit and dissemination of scientific research documents, whether they are published or not. The documents may come from teaching and research institutions in France or abroad, or from public or private research centers.

L'archive ouverte pluridisciplinaire **HAL**, est destinée au dépôt et à la diffusion de documents scientifiques de niveau recherche, publiés ou non, émanant des établissements d'enseignement et de recherche français ou étrangers, des laboratoires publics ou privés.

UNIVERSITY PARIS-SUD 11
DOCTORAL SCHOOL EDOM
Ecole Doctorale Ondes Matiere

P H D T H E S I S

to obtain the title of

PhD of Science

of the University Paris-Sud

Defended by

Serhiy MOCHALSKYY

Modeling of the negative ion extraction from a hydrogen plasma source. Application to ITER Neutral Beam Injector

Thesis Advisor: Tiberiu MINEA

prepared at LABORATOIRE DE PHYSIQUE DES GAZ ET
DES PLASMAS

December 20, 2011

Jury :

<i>Reviewers :</i>	Ursel FANTZ	- IPP, Garching
	Guy BONNAUD	- CEA-INSTN, Saclay
<i>Advisor :</i>	Tiberiu MINEA	- University Paris-Sud, Orsay
<i>Examinators :</i>	Christophe BLONDEL	- University Paris-Sud, Orsay
	Alain SIMONIN	- CEA-IRFM, Cadarache

Abstract

The development of a high performance negative ion (NI) source constitutes a crucial step in the construction of Neutral Beam Injector of the future fusion reactor ITER. NI source should deliver 60 A of H^- (or 40 A D^-), which is a technical and scientific challenge, and requires a deep understanding of the underlying physics of the source including the role of the magnetic filter. The present knowledge of the ion extraction mechanism from the negative ion source is mainly based on experimental work involving among other difficulties the complex magnetized plasma sheaths used to avoid electrons being co-extracted from the plasma together with NI. Moreover, due to the asymmetry induced by the crossed magnetic configuration used to filter and further to deflect the electrons, any realistic study of this problem must consider the three space dimensions.

To properly address this problem, 3D Particle-in-Cell electrostatic collisional code was developed within the framework of this thesis. Binary collisions between the particles are introduced using Monte Carlo Collision approach. The code estimates the solution of Boltzmann equation, bringing detailed information about the density and energy distribution of the different species. The code uses Cartesian coordinate system, but it can deal with curve boundary geometry as it is the case of the extraction apertures. Complex orthogonal magnetic fields are also taken into account. This code, called ONIX (Orsay Negative Ion eXtraction), was used to investigate the plasma properties and the transport of the charged particles close to a typical extraction aperture.

The main results obtained from this code are presented in this thesis. They include:

- negative ions and electrons 3D trajectories in the extraction region of ITER Neutral Beam Injector plasma source system;
- the meniscus formation in the plasma in front of the extraction aperture by the repelling of positive ions;
- negative ion and electron current density profiles for different local magnetic field configurations;
- production, destruction, and transport of H^- in the plasma volume, close to the extraction region. Production of H^- in the volume is investigated via electron dissociative attachment to the vibrationally excited molecules $H_2(v)$ collision. The negative ion destruction processes are: (i) mutual neutralization, (ii) electron detachment and (iii) associative and non-associative detachment with H ;
- negative ion surface production is examined via (i) interaction of the positive ions H^+ and H_2^+ with the aperture surface and (ii) collisions of the neutral gas H with plasma grid wall.

- extraction efficiency of the negative ion produced from the volume and the plasma grid surface;
- the role of sheath behavior in the vicinity of the aperture and the NI extraction limitation due to the double layer structure induced by negative ion flux from the surface;
- influence of the external extracted potential value on the formation of negative sheath and the strength of the magnetic filter on the total extracted NI and co-extracted electron current;
- the suppression of the electron beam by the negative ion produced at the plasma grid wall.

Most of these results are in good agreement with experimental data obtained by IPP group (Garching, Germany). The performance predicted for the extractor fulfills the ITER NBI requirements in terms of extracted NI and electron currents and current densities. Thus, it opens a large field of possible configurations being a valuable tool for future optimizations of the NI source.

Acknowledgement

Here I would like to express my sincere gratitude to people who have been undoubtedly helping me to complete this thesis.

I would like to first thank my academic advisors Professor Tiberiu Minea and Dr. Agustin Lifschitz for their continual guidance and for the opportunity to conduct this work. They introduced me exciting problem of the negative ion extraction for ITER NBI system and supported me a lot during all stages of the model developing and analysis of the results. They have faithfully helped me not only with research problems, but also with problems in daily life in foreign country. They supported me in one way or another for three years and have been the best advisors I could imagine having.

I want further thank my colleagues in the laboratory LPGP for all their help and friendship. I wish them all large inspiration in all their next undertaking. I would like to express my special thank to the laboratory director Dr. Gilles Maynard, CNRS Research Director for his generous help throughout my work.

This research could not have been possible without financial support of the "Centre National de la Recherche Scientifique" and "Commissariat l'Energie Atomique et aux Energies Alternatives". I would like to express also my sincere thank to Dr. Alain Simonin, the scientific coordinator from CEA for his perpetual support and helpful discussions.

Of course, last but certainly not least, I would like to thank my family and all my friends from France and Ukraine for their patience, support and understanding.

List of Figures

1.1	Evolution of the world energy consumption - y axis (in Gigatons of Oil Equivalent) <i>versus</i> time evolution - x axis (in years). Inlay figure presents the world population growth [1]	14
1.2	Cross-section for different fusion reactions	15
1.3	Research progress towards the Lawson criterion at the world's most important machines with magnetic confinement. The triple product (density n , temperature T and energy confinement time τ) - y axis plotted against the center plasma temperature T - x axis. The open symbols represent the experiments with deuterium plasmas, the solid symbols shows the experiments with a mixture of deuterium and tritium plasmas	17
1.4	Sketch of (a) tokamak and (b) stellarator (picture taken from the CEA and IPP web sites)	18
1.5	Cutaway of the ITER project [21]	22
2.1	Schematic view of the ITER Neutral Beam Injector	26
2.2	The cross-section of the SINGAP accelerator [38]	27
2.3	The cross-section of the MAMuG accelerator in the Japanese test facility [39]	27
2.4	Cutaway ITER NBI neutralizer system [16]	28
2.5	Schematic set-up of the prototype radio-frequency negative ion source ITER NBI system	30
2.6	Geometry of the single extraction channel at the ITER source [16]	30
2.7	Accelerated negative ion current densities via CEA (yellow cycle) and LAG (blue triangle) acceleration systems from the hydrogen source plasma (at the bottom). The electron/negative ion current ratio is shown at the top [52]	33
2.8	The example of 1 h Hydrogen plasma run on the MANITU test bed machine. The blue line shows the extracted negative ion current. The red line corresponds to the co-extracted electron current [61]	34
2.9	a) - Positive ion density distribution in the horizontal direction for different magnetic field strength; b)- Positive ion density distribution in the vertical direction for different magnetic field strength. Pressure of 0.6 Pa and power of 40kW per driver have been used [31]	35
2.10	The density distribution of the charged particles (a) and the neutral gas (b) along the simulation domain of the NBI plasma source (0 m corresponds to the driver position). The constant values of the pressure – 0.3 Pa and the power 60 kW were used in all simulations [65]	38

2.11	The negative ion trajectories (magenta) calculated by the SLACCAD code. Blue lines indicate the external positive potential distribution [68]	38
2.12	Negative ion (a) and electron (b) trajectories calculated by the EAMCC code. The power heat load on each grid corresponding to the whole accelerator system (1280 beamlets) is presented at the bottom [68]	40
2.13	Calculated extraction probability versus initial energy of the surface produced negative ions in chamfered and flat configurations of the plasma grid aperture (a). The extraction probability versus the filter magnetic field strength for different starting ion energies (b) [72]	41
2.14	Distribution of the electron and negative ion densities close to the plasma grid grounded (0 V - dashed line) and biased (36 V - solid line) [76]	42
2.15	The electron and negative ion densities along the extraction axis without (dashed line) and with (solid line) magnetic filter field: $B_{peak} = 4$ mT. PG is grounded in both cases [76]	43
2.16	The evolution of the total extracted negative ion (a) and electrons (b) currents as a function of the simulation time [79]	44
3.1	Schematic view of the simulation domain. The cross section in (y, z) plane is a square with side-length of 20 mm. The conical aperture has the larger diameter of 18 mm (plasma side - left-hand side) and the smaller diameter of 14 mm (extraction grid side - right-hand side)	46
3.2	The potential distribution along the large simulation domain (including EG) without plasma. The right border plane represents the extraction grid	47
3.3	Chartflow of the ONIX code	50
3.4	The initial positive ion density (H^+) distribution along the simulation domain. The plasma grid is centered at the distance of 20 mm	51
3.5	The potential distribution along the symmetry axis at $y = 10$ mm $z = 10$ mm plane. Red solid line - simulation with $\Delta t = 3 \times 10^{-12}$ s, green dot line - $\Delta t = 1.5 \times 10^{-12}$ s	53
3.6	The Probability Density Function (PDF) of the initial electron velocity distribution	55
3.7	Three numerical technique to generate the plasma tested in the ONIX code. The particles re-injection procedure is shown in the left. The particles flux injection is shown in the middle. The particle injection from the neutral plane - in the right	56
3.8	Example of linear $2D$ charge assignment on the mesh points with computational particle located at (x, y) . Eq. 3.8 is used to distribute the charge onto the grid nodes	58
3.9	Chartflow of the CG method implemented in the ONIX program (Poisson Solver part of Fig. 3.3), where r, ϕ, d, Ad are matrices of equal size $(0 : i, 0 : j, 0 : k)$. The tolerance corresponds to the required accuracy	61
3.10	The irregular region of simulation domain. The solid line is the real boundary; the open circle indicates the problematic points	63

3.11	Potential created by a given charge distribution inside a grounded cylinder calculated without the boundary correction in the Poisson solver (a) and with the correction (b) Eq. 3.23. In the case without boundary correction (a) the gridded structure is presented at the edges (yellow and blue isolines). This artifact is suppressed when potential boundary correction technique is applied (b)	64
3.12	Distribution of magnetic field along the simulation domain. Red line represents the magnetic filter field in the vertical z direction, green line – deflecting magnetic field in the horizontal y direction. Plasma grid is located between $x = 19$ mm and $x = 21$ mm (blue line)	66
3.13	The schematic view of the leapfrog method. Particle position is evaluated at integral time step, while the velocity is calculated at half time step	67
3.14	Chartflow diagram of the particles motion subroutine using Boris leapfrog methodology (Move Particles part of the general chartflow Fig. 3.3)	68
3.15	Chartflow diagram of the collision event (Collisions part of the general chartflow Fig. 3.3)	71
3.16	Cross section of the electron dissociative attachment reaction	72
3.17	The cross-sections of the most important negative ion loss processes [54, 102]	72
3.18	Charge assignment procedure of the particles that are located between the processes boundaries	76
3.19	Schematic view of the boundaries potential data exchanging between parallel tasks	77
3.20	Computational time as the function of amount of the processors working in parallel	78
3.21	Trajectories of three charged particles released from the middle of the computation domain in the absence of electric and magnetic fields. All particles pass the same distance retaining accurately straight trace	80
3.22	Trajectories of three particles with negative charge (red line), positive charge (green line) and zero charge (blue line) in the constant magnetic field of $B_z = 0.0005$ T	81
3.23	Trajectories of the negative charged particles with mass ratio 2 in the constant magnetic field $B_z = 0.0005$ T	82
3.24	Trajectories of the negatively charged (red line), positively charged (green line) and neutral particles under the influence of the $E \times B$ drift	83
3.25	The electric dipole potential distribution computing by the Poisson solver implemented in the ONIX code	84
3.26	The distribution of the electric dipole field in x direction calculated by the ONIX code	84
3.27	Snap shots of the potential distribution at four simulation instants separated by \sim half plasma period	85
3.28	Parallel computation of the electron trajectory. Each color indicates different processor corresponding to the domain through which the test electron moves	86

4.1	Spatial distribution of ion density in the plane $y = 10$ mm at the beginning of the simulation (a) and at $t = 0.3 \mu s$ (b)	88
4.2	Spatial distribution of ion density in the $x - z$ plane at the beginning of the simulation (a) and at $t = 0.3 \mu s$ (b). The pre-sheath lies from $x = 5$ to $x = 10$ mm	89
4.3	Spatial distribution of electric potential in the $x - z$ plane at the beginning of the simulation (a) and at $t = 0.3 \mu s$ (b) for the "large" initial plasma. The pre-sheath lies from $x = 5$ to $x = 15$ mm	90
4.4	Extracted electron current vs. time for an electropositive hydrogen plasma	91
4.5	Quasi steady-state potential profile at the axis ($y = 10$ mm, $z = 10$ mm) without NI and with 10% of NI in the plasma volume (the figure is cut at point $x = 20$ mm in order to distinguish the potential difference between two cases)	92
4.6	Extracted electron and NI current vs. time for the plasma with 10% of negative ions in the plasma volume	92
4.7	Positive ion charge distribution in the vertical midplane (a) and in the horizontal midplane (b). The plasma is composed by the electron and H^+	93
4.8	Electron charge distribution without (a) and with (b) the deflecting field in two different planes (a:x-y plane, b:x-z plane)	94
4.9	Negative ions distribution on the exit plane without (a) and with (b) plasma. Filter and deflecting magnetic fields are present in both simulations	95
4.10	Trajectories of NI released from the aperture inner wall (a) and over the PG (b) - surface production. Initial energy 1 eV	96
4.11	Zoom of the spatial distribution of electric potential close to the PG	96
4.12	Trajectories of NI created in the volume, close to the aperture. Initial energy 1 eV	97
4.13	Fraction of extracted negative ions created in the volume as a function of the initial x position. The same data in semi log scale is shown in the inset	97
5.1	Spatial distribution (x,y) of positive ion density in the mid-plane ($z = 10$ mm) of the simulation box at the beginning of the simulation ($t = 0$, left) and close to the steady-state ($t = 0.3 \mu s$, right)	100
5.2	Spatial potential distribution for the same situation as in Fig. 5.1	100
5.3	Time evolution of the extracted electron and negative ion currents. Blue line(+) - co-extracted electron current. Red line (\square)- NI extracted current from the PG inner aperture surface produced by neutrals impact. Pink line (*)- NI extracted current from the PG outer surface produced by neutrals impact Green line (\cdot) - NI extracted current from the volume, produced <i>via</i> electron dissociative attachment collisions	101
5.4	Extracted NI current by the surface production mechanism for different emission rates	103

5.5	(a) Spatial distribution of the electric potential close to the PG (PG is located between $x = 19$ mm and $x = 21$ mm). The optimal emission rate from the PG was used. (b) transverse profile of the electric potential at three different location along the aperture: (A) corresponds to $x=19.04$ mm, (B) $x=20.16$ mm, (C) $x=20.72$ mm	104
5.6	Number of extracted NI as a function of the born axial position (along PG surface) for different emission rates. The plasma grid goes from $x = 19$ mm and $x = 21$ mm	105
5.7	Total extracted NI current vs. positive external potential. Red line - ONIX calculations, blue line - experimental BATMAN results [58]	106
5.8	Negative ion current/electron current ratio vs. positive external potential. Red line - ONIX calculations, blue line - experimental BATMAN results [58]	107
5.9	Electron (\times) and negative ion ($+$) currents vs magnetic fields strength .	108
5.10	Electron current vs. magnetic filter field strength γ_f	108
5.11	Intensity of the extracted NI at the exit plane ($y - z$) with a) and without b) magnetic fields	109
5.12	The potential distribution along the simulation volume in two cases: a) – without negative ions production from the PG surface (corresponds to Cs free experimental regime) and b) with NI emitted from the PG wall . . .	110

List of Tables

1.1	Technical data and plasma parameters of the future tokamak ITER [18, 21]	21
2.1	Main parameters of the NBI negative ion source facilities [52, 16]	36
3.1	Main initial plasma parameters	49
3.2	Simulation units and physical constants used in the ONIX code	51
3.3	The comparison of time performance for solving the Poisson equation using the Conjugate Gradient and the Precondition Conjugate Gradient methods	62
3.4	Main volume reactions into the hydrogen plasma. * indicates the reactions included in the simulation model	74

Contents

1	Introduction	13
1.1	Fusion energy	14
1.2	Plasma confinement	16
1.3	Plasma heating	19
1.4	ITER tokamak	20
1.5	Scope of this work	22
2	ITER Neutral Beam Injector System	24
2.1	Conceptual Design of the ITER NBI	24
2.2	ITER Neutral Beam Injector Plasma Source	29
2.2.1	BATMAN Experimental 1/8 Size ITER Negative Ion Source Test Bed	32
2.2.2	The MANITU Experimental 1/8 size ITER Negative Ion Source Test Bed Machine	32
2.2.3	RADI – Experimental Source Machine with Large Plasma Area	34
2.2.4	ELISE – the Half-size ITER Negative Ion Source Test Bed Machine	35
2.3	Numerical Approaches for Plasma Source Modeling	36
2.3.1	2D Fluid Simulation of the Plasma Source	37
2.3.2	SLACCAD 2D Monte Carlo Code	37
2.3.3	EAMCC 3D Monte Carlo Code	39
2.3.4	Monte Carlo Code TRAJAN	40
2.3.5	1-2D PIC Simulation of Negative Ion Extraction	41
2.3.6	Three-dimensional PIC Simulation	42
3	Numerical Approach	45
3.1	Extraction Region and Simulation Domain	45
3.2	General Description of the ONIX Code	47
3.3	Computation Parameters	49
3.3.1	Initial Plasma Conditions	49
3.3.2	Simulation Units	50
3.3.2.1	Length Scale	51
3.3.2.2	Time Scale	52
3.3.3	Weighting Scheme	52
3.4	Boundaries Conditions	53
3.5	Initial Velocity Distribution	54
3.6	Different Types of Plasma Formation	55

3.7	Particle-in-Cell Method in the ONIX Code	57
3.8	Poisson Solver	58
	3.8.1 Discretization	58
	3.8.2 Conjugate Gradient Method	59
	3.8.3 Potential Boundaries Correction	62
	3.8.4 Potential Boundaries Conditions	64
3.9	Electric and Magnetic Fields Calculation	65
3.10	Particle Movement	66
3.11	Model for Collision Events	69
	3.11.1 Basic Probability Calculation for Particle Collision Events	69
	3.11.2 Volume Collisions	70
	3.11.3 Plasma Wall Interaction Collisions	70
3.12	Parallelization	74
	3.12.1 Initialization	74
	3.12.2 Particles Injection	75
	3.12.3 Charge Assignment and Field Projection	75
	3.12.4 Poisson Solver	76
	3.12.5 Particle Movement	77
	3.12.6 Parallelization Efficiency	78
3.13	Numerical Check-up	79
	3.13.1 Particle Motion Tests in Constant Field	79
	3.13.2 Particle Motion Test at Constant B Field	79
	3.13.3 Mass Checking	80
	3.13.4 Particle Motion Test in Constant $E \times B$ Field	81
3.14	Electric Potential Test	82
3.15	Plasma Oscillation Test	83
3.16	Parallelization Test	85
4	Results in Collisionless Approximation	87
4.1	Self-consistence of the Meniscus Formation	87
4.2	Calculation of Potential Distribution	90
4.3	Extracted Electron Current	90
4.4	Simulation with Negative Ions	91
4.5	Symmetry Breakup	92
4.6	Magnetic Fields Effect on the Extracted Electron Current	93
4.7	NI Extraction	94
	4.7.1 Negative Ion Extraction from the Plasma Grid Wall	95
	4.7.2 Negative Ion Extraction from the Volume	96
5	Results Including Plasma Kinetics	99
5.1	General Behaviour	99
	5.1.1 Self-consistency of the Meniscus Formation	99
	5.1.2 Potential Calculation	100
5.2	Evolution of the Extracted Electron and Negative Ion Current	101
5.3	Saturation of Negative Ion Current	102
5.4	Limitation of the Negative Ion Extraction	103

5.5	Effect of the External Positive Potential on the NI Extraction	105
5.6	Effect of the Magnetic Field on the Electron Extraction	106
5.6.1	Study of the Deflecting Field Effect	107
5.6.2	Study of the Filter Field Effect	107
5.6.3	Halo of the Negative Ion Beam	109
5.7	Suppression of Electron Current by Production of NI From PG Wall . . .	109
6	Conclusions and Future Work	111
6.1	Unique Numerical Tool	111
6.2	Summary of Results	111
6.3	Future Plans	113

Chapter 1

Introduction

The world energy consumption has been continuously growing since the dawn of the industrial revolution in the nineteenth century. After the second world war, the growth of the energy demand strongly accelerated, following the spreading of the industrialization to underdeveloped countries and the global population growth. The growth of the energy consumption constitutes a worldwide tendency, and it concerns specially emerging economies as China, India and Brazil. Fig. 1.1 shows three scenarios of the future evolution of the world energy consumption [1]. **A** - “High Growth” describes a future of extreme economic growth and impressive technological improvements. **B** - “Middle Course” represents a future of more realistic technological improvements and more intermediate economic growth. The scenario **C** - “Rich and Green” shows future that includes both strong technological improvements and strict environmental control. However, even in the most promising case (**C**) the twice more energy is required in comparison with the present moment.

Fossil fuels (gas, oil and coal) provide at the present more than 80 % of the energy consumed in the world. Reserves of oil and gas are expected to be exhausted in next decades, whereas for coal the estimations vary between 40 to 200 years. The use of fossil fuels, on the other hand, constitutes a risk for the environment. Their burning produces huge amounts of CO₂, that is emitted to the atmosphere. There exists a scientific consensus on the fact that these emissions contribute significantly to the greenhouse effect responsible of the global warming. Renewable energy sources constitutes today a rapidly evolving alternative to fossil fuels. Nevertheless, the currently envisaged sources present serious drawbacks. The construction of hydroelectric power plants by artificial damming of rivers is limited by the small number of potential sites still unexploited. On the other hand, very large dams damage the ecosystem. Solar and wind power plants delivering powers comparable to that of fossil or nuclear plants would be huge, and they would also constitutes an environmental problem. Moreover, as the power provided by these centrals cannot be controlled, they require a way to store the energy. Nuclear fission plants present the problem of producing important amounts of radioactive waste and the risk of potentially catastrophic accidents. One of the alternative energy sources can be the fusion which doesn't use exhaustible resources and not require specific location. The electric power stations based on the fusion could become the alternative “clean” energy source in the nearest future, replacing nuclear and fossil-fuel power stations.

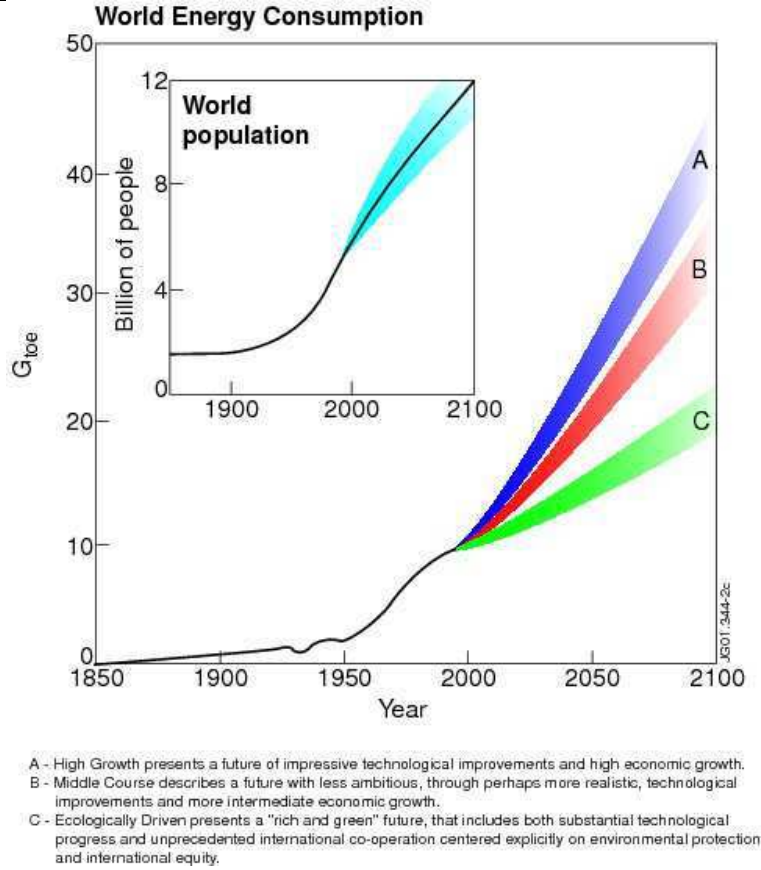


Figure 1.1: Evolution of the world energy consumption - y axis (in Gigatons of Oil Equivalent) *versus* time evolution - x axis (in years). Inlay figure presents the world population growth [1]

1.1 Fusion energy

The fusion reaction was recognized as the power source of the Sun and other stars in 1938 [2]. Since then, fusion research has been planned in many laboratories all over the world, in order to reproduce it on the Earth in a controlled manner. The fusion has become one of the most promising new energy sources. It is a process where two light nuclei fuse together to form a new heavier element, thereby releasing energy. The fusion reaction in the Sun is a multi step process, during which hydrogen's nuclei transform into helium. The process begins with thermal collision of two protons. The colliding protons create a deuteron, with simultaneous emission of a positron and a neutrino (Reac. 1.2a). To overcome the electrical repulsing barrier the energy of 2.298×10^{-13} J is required. The created deuteron hits another proton, thus forming ${}^3\text{He}$ nucleus (Reac. 1.2b). Finally, two ${}^3\text{He}$ find each other and rearrange into one stable ${}^4\text{He}$ nucleus and two protons (Reac. 1.2c). The energy released in this process is:

$$\Delta E = [4 * 1.007825u - 4.002603u] * [931\text{MeV}/u] = 26.7\text{MeV}, \quad (1.1)$$

where $1.007825u$ and $4.002603u$ are masses of the proton and helium atoms, respectively; neutrino and photons are considered to have no mass.



Reaction (1.2a) requires the weak interaction in order to transform protons into a neutron. The likelihood of such weak interaction is almost zero; thereby, the fusion process is very slow. Nevertheless, the Sun and other stars overcame the low reaction rate due to their large mass. On the Earth, such fusion process can't be achieved, since fusion reactor is much smaller than that of a star. The most appropriate candidates for fusion on the Earth are:



The production rate of the reactions 1.3 is proportional to cross section of the reactants, which in its turn depends on their kinetic energy (See Fig. 1.3 [3, 4]).

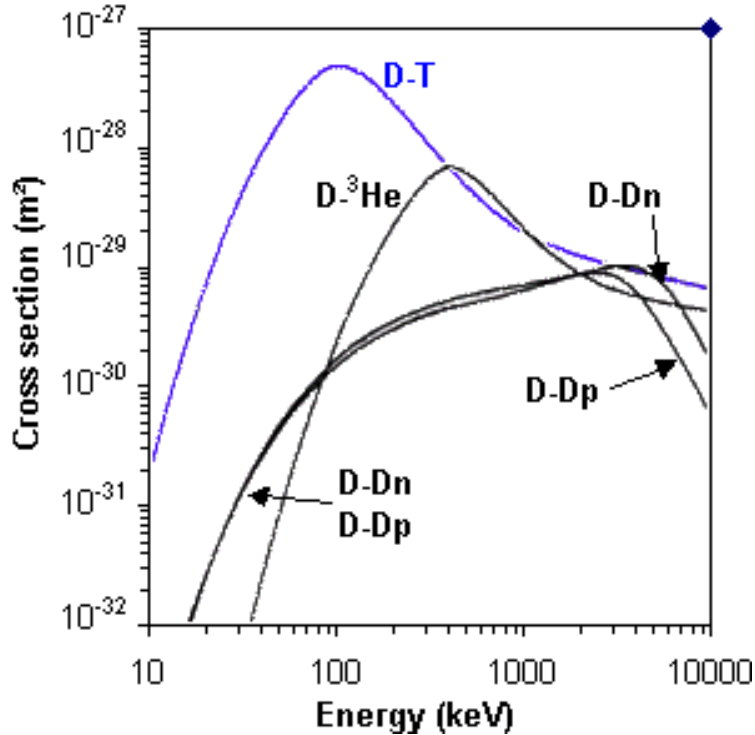


Figure 1.2: Cross-section for different fusion reactions

At low energies, the cross-sections of the fusion reactions are small due to the Coulomb barrier that repels the two nuclei and does not allow them approach close enough in order

to fuse [5, 6]. However, this electrostatic barrier is eventually overcome when kinetic energy of the reactants increase. As Fig. 1.2 shows, reaction 1.3a has the highest cross-section value at relatively low energies (about 70 keV). Moreover, the produced energy is one of the highest in the group of the perspective fusion reactions – 17.6 MeV. Thereby, it becomes the most promising candidate for fusion on the Earth so called "controlled fusion".

The principal reactants for reaction 1.3a are two hydrogen's isotopes: deuterium and tritium. Deuterium occurs naturally and could be extracted from the seawater (about 30 g from one cubic meter of water). Tritium is unstable radioactive hydrogen's isotope, with half-life around 12 years. It can be produced in nuclear reactor from lithium, which exists in large quantities in the Earth's crust. The energy produced from 1 kg of deuterium and 1.5 kg of tritium equals the energy released by burning of 19000 tons of oil, which makes fusion very attractive from the point of view of resources consumption.

In order to achieve ignition, when fusion reaction becomes self-sustained, the deuterium and tritium atoms must be heated from an external source. At thermonuclear temperature gas atoms are ionized. This hot gas, when electrons and nuclei are not bound together, is called plasma. Ignition condition also requires high plasma density in order to obtain enough fusion collisions. In addition to the plasma heating, hot electrons and nuclei must be trapped in a specific volume to minimize the energy loss. If plasma loses its energy faster than it can be obtained from the fusion reaction or external heating, the process will fade out. Eventually, if all conditions are satisfied the fusion reaction will provide itself enough energy to heat plasma.

The progress towards the plasma ignition can be expressed by the Lawson criterion, which includes triple product $nT\tau$, where n stands for plasma density, T - temperature and τ - energy confinement time. The last parameter gives the quality of the heat insulation and the rate of plasma energy losses $1/\tau$. The energy confinement time increases simultaneously with the plasma volume, as large plasma has better confinement in the core than a small one. The fusion reaction will be self-sustained, when the product of aforesaid parameters is sufficiently high. For instance, for the deuterium and tritium reaction it must be:

$$nT\tau \geq 10^{21} \text{ keVs/m}^3 \tag{1.4}$$

Fig. 1.3 shows the research progress towards ignition of the most important fusion devices with magnetic confinement in the world. Considerable progress of the triple product has been achieved in the last 40 years. It is expected that the next generation of the fusion device will achieve the ignition conditions in 2020-2025.

1.2 Plasma confinement

The fusion reactions on the Sun and other stars are balanced out and confined by high gravitation force, which prevents plasma cooling and dispersing. On the Earth, the gravitation confinement is impossible, hence other methods of confining plasma had to be found. At present, two technologies are well developed: the inertial and magnetic confinement.

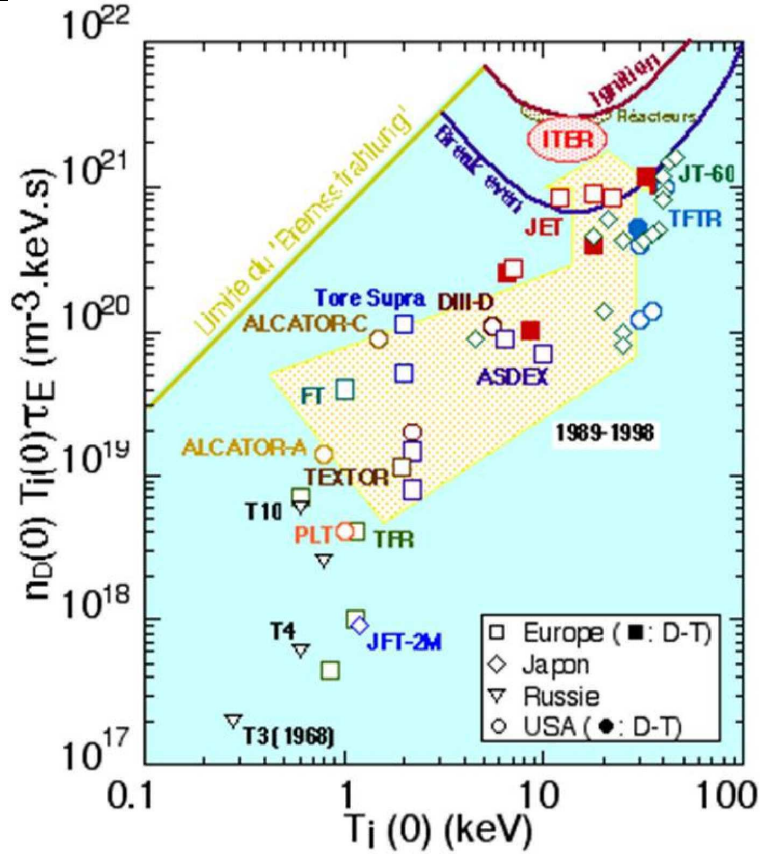


Figure 1.3: Research progress towards the Lawson criterion at the world's most important machines with magnetic confinement. The triple product (density n , temperature T and energy confinement time τ) - y axis plotted against the center plasma temperature T - x axis. The open symbols represent the experiments with deuterium plasmas, the solid symbols shows the experiments with a mixture of deuterium and tritium plasmas

In the inertial confinement, high energy beams (generally a laser beam) are focused on small volume of deuterium-tritium solid target, which commonly has the form of a pellet. It ionizes and evaporates the outer layer of material, thus creating a plasma envelope surrounding the target sphere. The heated layer explodes outwards, and generates reaction force moving inwards, in the direction of the inner layers of the target, simultaneously sending shock waves into the center. The core of the target may be compressed and heated so intensely, that the fusion reaction occurs. The thermonuclear blow-off spreads quickly inside the sphere, yielding several times more energy than it was spent on initial heating. The aim of the inertial fusion is to produce continuous chain of such reactions to achieve the ignition conditions during very short time (less than a nanosecond). This time is limited by the inertia of the fuel, which gave the name to inertial confinement [7, 8].

In the magnetically confined high-temperature plasma, the particles are completely ionized and their behavior can be described as a mixture of charged particles. Their movement can be restricted by the magnetic field due to the Lorentz force. All charged particles gyrate around the magnetic field lines with a cyclotron frequency $\omega_c = |q|B/m$

and the Larmor radius $r_L = mv_{\perp}/|q|B$, where q is the charge of a particle, B - the magnetic field, m - the mass of particle, and v_{\perp} - the velocity component perpendicular to the magnetic field direction. Thus, it is possible to efficiently confine the plasma by the magnetic field. The goal of the magnetic confinement is to avoid the hot particles flow coming onto the reactor wall. The particles will cool down within scrape-off layer of the reactor vessel, and thereby will lose their energy.

A linear device is unsuitable for the fusion due to large energy losses at the ends. To efficiently confine the plasma, the magnetic field lines must be closed in themselves, thereby creating a toroidal structure. However, such configuration with a pure toroidal magnetic field causes particle losses arising from various drifts and instabilities. For instance, the gradient of the magnetic field creates the so-called grad B drift, which separates electrons and ions in the vertical direction. This causes rise of electric field E , that leads to an outward $\vec{E} \times \vec{B}$ drift of the whole plasma. This undesirable drift can be suppressed by adding another magnetic field (poloidal) perpendicular to the toroidal one. When toroidal and poloidal components come together, they create a helical structure of the twisted magnetic lines, thus suppressing the drift and improving the plasma confinement [9, 10].

Presently, the magnetic helical confinement is applied in two types of fusion machines: the tokamak and the stellarator (Fig. 1.4.).

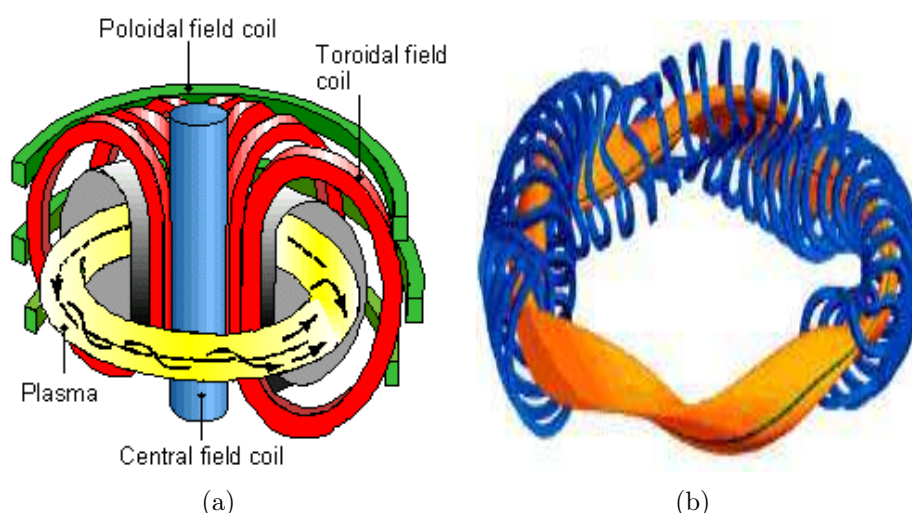


Figure 1.4: Sketch of (a) tokamak and (b) stellarator (picture taken from the CEA and IPP web sites)

The tokamak (in Russian – toroidal chamber with a magnetic coils) was designed in USSR in 1951 by Andrey Sakharov and Igor Tamm [11]. The tokamak includes a set of coils, evenly surrounding the vacuum vessel to generate the magnetic field in the toroidal direction. The poloidal magnetic field is created by a strong toroidal plasma current which is generated in the plasma itself by a transformer placed in the middle of the torus. The additional poloidal field coils are used mainly for the plasma shaping and stability (Fig. 1.4(a)). In the stellarator, the poloidal magnetic component is composed of complicated windings of external coils, thus the complex helical magnetic structure is generated from the coils themselves (Fig. 1.4(b)). The advantage of such device is the

potential to maintain the steady-state plasma. On the other hand, in the tokamak the poloidal current, which causes most of the instabilities, also serves to heat the plasma. In the stellarator all plasma heating has to be done from the outside. However, the complex configuration of the magnetic coils is the main disadvantages of the stellarator from the engineering point of view.

A measure of helicity of the resulting magnetic field is given by the safety factor:

$$q = \frac{m}{n} = \frac{rB_\varphi}{RB_\theta} \quad (1.5)$$

where B_φ and B_θ are toroidal and poloidal magnetic fields respectively, r is the minor radius, and R is the major radius of the torus. The safety factor describes the number of the toroidal winding needed before a field line returns to the same poloidal coordinate. It also shows the ratio of the toroidal magnetic field to the poloidal one. In the tokamak it varies from 1 at the plasma center to 8 at the plasma edge. More details about the tokamak structure are presented in Section 1.4, where the ITER tokamak reactor is described.

1.3 Plasma heating

The fusion reaction occurs when the plasma temperature reaches about 10 – 20 keV (about 100 million degree Celsius), according to the Lawson criterion. None of the known ways of plasma creation on the Earth gets this condition initially. The heating of the plasma plays a decisive role in achieving such high temperatures. At present, there are three most developed methods of heating the plasma: the ohmic heating [12], the waves heating [15, 14, 13], and heating by injection of energetic heavy particles [16].

In a tokamak, The toroidal current flowing through the plasma is responsible of the poloidal magnetic field. However, it has also the property of heating the plasma via the natural Joule effect (ohmic heating). The same principle is utilized in the electric light bulb, when current is passing through a filament. The ohmic heating depends on the plasma resistivity and the applied current, in accordance with the Joule effect. Unfortunately, the rise of the plasma temperature tends to decrease its resistivity and this heating mechanism becomes inefficient. The maximum temperature produced by the ohmic heating is limited to 10-20 million degrees. This means, that in order to achieve the fusion temperature condition the external additional heating must be applied.

The second method of increasing the plasma temperature is the antenna waves heating. The plasma has ability to absorb the electromagnetic waves, which will transfer their energy to particles. There are two main mechanisms of the radio-frequency heating to enable the particles obtain the energy from the wave: the cyclotron and the Landau absorption. In both cases, the particles have to turn with the same frequencies as the waves, thereby to be in the resonance. In the cyclotron absorption the wave couples to the plasma at the same frequencies as the particles rotation induced by the magnetic field. The Landau absorption is based on the waves coupling to the particles at the same population frequencies in such way that particles and waves have the same propagation velocity. Nowadays, there are three mechanisms of the antenna heating applied at the fusion reactors. They are classified by the range of propagation frequencies: the ion cy-

clotron heating (in range of MHz), the electron cyclotron heating (about hundred GHz), and the hybrid heating (few GHz).

The last mechanism of the plasma heating consist of the injection of high energetic particles (neutrals) into the plasma. The injected particles transfer their energy to the plasma ion/electron via collisions. Strong electric fields are used to accelerate the hydrogen/deuterium ions in order to obtain the high energy beam. Generally, the charged particles are neutralized before being injected into the tokamak vessel. This is done with the aim of preventing the effect of magnetic field which could trap them at the machine's entrance. To deliver the neutrals into the plasma core inside the fusion reactor, the beam must be injected with sufficiently high energy (depending on the reactor size and the plasma parameters). Because of the low value of the electron-ion mutual neutralization cross section, the neutral beam injection based on acceleration and neutralization of positive ions is efficient only for small scale tokamak. Thereby, a negative ions concept has to be introduced in order to achieve the higher energies. The negative ions are more problematic in the sense of their production and subsequent extraction from the plasma, but they have much better neutralization efficiency than positive ions.

The combination of all heating systems will provide enough energy to increase the plasma temperature and thus achieve the fusion in the plasma reactor. When the number of reactions exceed the threshold, the helium nuclei themselves will produce enough energy to maintain the process. As a result, contribution of the external heating will be no longer necessary, and the plasma will reach the self-ignition condition.

This thesis is dedicated to understanding of the mechanisms and physics of the negative ion production and their extraction from the plasma source in the neutral beam injector (NBI) system of the future thermonuclear reactor ITER. More details about ITER tokamak are presented in the next section, while the principle of the ITER NBI is described in details in Chapter 2.

1.4 ITER tokamak

The ITER (International Thermonuclear Experimental Reactor) is the future experimental thermonuclear reactor with magnetic confinement [17, 18, 19, 20, 21]. The main goal of the ITER is to demonstrate the possibility and feasibility of fusion power on the Earth. The amplification factor Q , showing the ratio between the power produced by the fusion to the input external power supplying the reactor in ITER, should achieve value of about 10. It means that from 50 MW of the input power (73 MW designed) tokamak will produce 500 MW of the output power from the fusion. Thereby, ITER will be the first fusion machine that gets more energy out of the fusion process, than it uses to generate it, which has never been shown before at other experimental facilities. Consequently, ITER should achieve ignition condition when switching off all additional heating systems, and plasma becomes self-sustained. The main technical data and parameters of the reactor are listed in Table 1.1.

The ITER plasma parameters were chosen to satisfy the steady state ignition condition during long pulse time (~ 400 s for H plasma). ITER will combine the advantages of 2 most successful existing fusion reactors: JET [22] and Tore Supra [23]. JET is close to ignition conditions because of the large dimensions of the torus, while Tore Supra has

CHAPTER 1. INTRODUCTION

ability for the long discharge time due to the super-conductive toroidal magnetic coils. The major radius of ITER torus is measured of 6.2 m, while the plasma minor radius is 2.0 m. The toroidal plasma current that is responsible for the generation of the poloidal magnetic field is planned to be ~ 15 MA. The toroidal magnetic field reaches value of about 5.3 T. The electron density and temperature are $10^{20} m^{-3}$ and 20 keV respectively.

Schematic view of the ITER is shown in Fig. 1.5. The Vacuum Vessel of the reactor is surrounded by a large stainless steel structure called Cryostat. It provides the vacuum environment and protect the reactor from an external damage. The Blanked covers the interior part of the Vacuum Vessel and protect it from the heat load and neutron fluxes of the fusion reaction. The neutrons will transform their kinetic energy into heat energy that will be in turn collected by the coolants. The Divertor is positioned at the bottom of the Vacuum Vessel. It is main interface between the hot plasma and surface material. Its main function is to extract heat, Helium ash and other impurities from the plasma.

Table 1.1: Technical data and plasma parameters of the future tokamak ITER [18, 21]

Total fusion power	500 MW
Q=fusion power/addition heating power	~ 10
Plasma inductive burn time	≥ 400 s
Plasma major radius (R_0)	6.2 m
Plasma minor radius (r)	2.0 m
Plasma current (I_p)	15 MA
Safety factor (q)	3
Toroidal magnetic field (B)	5.3 T
Electron density (n_e)	$10^{20} m^{-3}$
Temperature (T)	20 keV
Plasma total heating	~ 50 MW
Neutral Beam Injector	33 MW
Electron cyclotron antenna	20 MW (170 GHz)
Ion cyclotron antenna	20 MW (50 MHz)
Plasma type	deuterium-tritium
Plasma volume	$837 m^3$

ITER design includes three auxiliary heating systems. They are the neutral beam, the ion cyclotron and the electron cyclotron heating. These systems will supply maximum of 73 MW heating power with contribution of the neutral beam injectors of 33 MW. The NBI heating system includes two injectors, each of which delivering 16.5 MW power into the ITER plasma. In the NBI a beam of the hydrogen/deuterium ions is produced and accelerated by the electric field. In order to penetrate into the ITER plasma core and generate sufficiently high toroidal current, responsible of the poloidal magnetic field in tokamak configuration, the neutral beam has to be injected with the energy of order 1 MeV supplying current of 40 A. As it has been described above, neutralization of the positive ions is not efficient at such energy. Therefore, a concept of neutralization of negative ions will be used in the ITER NBI system. However, the production and further extraction of negative ions together with acceleration of 40 A beam to the energy of 1 MeV are the most problematic issues in the NBI plasma source system. On the one hand,

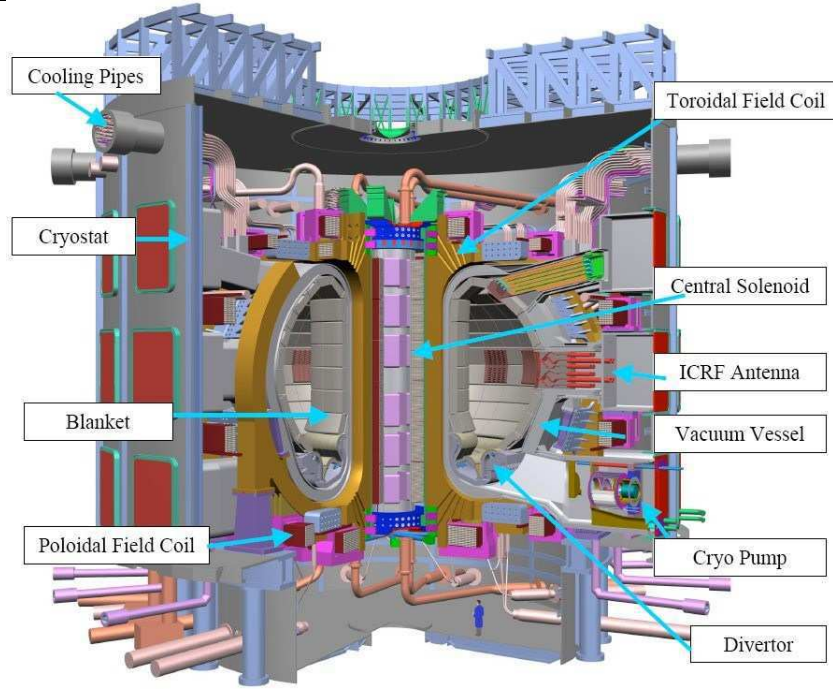


Figure 1.5: Cutaway of the ITER project [21]

undesirable co-extracted electron beam consumes the acceleration machine power, thus causing addition heat load onto the acceleration grids. On the other hand, the negative ion surviving length in the source plasma is few centimeters. It means that negative ions created only in vicinity of the acceleration system could be extracted. Moreover, negative ions could be destroyed even after extraction due to the electron detachment process ($H^- + H_2 \rightarrow H + H_2 + e$).

1.5 Scope of this work

The development of suitable negative ion source and an extraction system constitutes crucial step in the construction of the neutral beam injector of ITER. The understanding of the mechanism of ion extraction from the negative ion source requires to know the physics of electronegative plasmas under magnetic fields.

The purpose of this thesis is to explain by the means of the numerical simulations the different mechanisms of the negative ion extraction (produced at the surface and in the volume) from the electronegative plasma source, and to find the best parameters of the extractor for maximizing the negative ion extracted current and minimizing co-extracted electron current.

In this thesis a full 3D Particles-in-Cell electrostatic code has been developed to investigate the transport of the NI and electrons in the extraction region of the ITER NBI plasma source system. The collisions between particles are introduced using a Monte Carlo Collisions scheme. The code gives the Boltzmann equation solution, providing detailed information about the density and energy distribution of different species. The code uses Cartesian coordinate system and can deal with complex boundary geometry,

CHAPTER 1. INTRODUCTION

as it is in the case of extraction holes. Two local real magnetic fields are applied, one to avoid e co-extraction and second to deflect the electrons that could however cross the grid. Both B fields are taken into account.

The thesis has the following structure: Chapter 2 reviews the structure of the ITER Neutral Beam Injector system and presents details about the NI source setup. An overview of the recent NBI plasma source testbed facilities is also given. In the end of Chapter 2 current simulation models of the plasma source, and their numerical approaches, are presented. The description of the developed code and numerical algorithms is given in Chapter 3. Chapter 4 includes results of the plasma screening effect in the collisionless approximation, proving necessity for full 3D model. In Chapter 5 the results of collisional plasma approximation (in particular, optimization and limitation of the NI extraction) are discussed. Finally, conclusions and perspectives for the future research are presented in Chapter 6.

Chapter 2

ITER Neutral Beam Injector System

Achieving and sustaining of thermonuclear temperature in the ITER plasma requires the use of external heating sources. One of the methods of transferring power to the plasma ions is the injection of energetic neutrals. In addition to plasma heating, it also contributes to the generation of the toroidal current responsible for the tokamak poloidal magnetic field. To increase toroidal current in the tokamak vessel up to 15 MA the neutral beams must be injected with energies of the order 1 MeV, which is a challenging task. In this section a detailed overview of the ITER Neutral Beam Injector system will be presented.

2.1 Conceptual Design of the ITER NBI

Initially, ITER will consist of two NBI, which should provide 33 MW power to the tokamak plasma. The layout of the injectors around the reactor allows future installation of the third diagnostic NBI system [24]. The system can supply the H_0 or D_0 energetic neutrals, depending on the ITER requirements. The beam power has to be deposited inside the plasma core. Thus, to overcome the magnetic confinement mode barrier it has to be injected with the sufficient high energy. Moreover, to maintain the T^+/D^+ ions ratio in the plasma close to 1 for the efficient fusion reaction, the beam energy must be even higher than 400 keV [25]. Due to the low value of the electron-ion mutual neutralization cross section at these energies [26], the NBI based on the acceleration and neutralization positive ions has become unpractical. Therefore, the negative ion concept has to be used due to their much higher neutralization efficiency for energies > 500 keV.

Beside a power deposition, the NBI system will be used to drive current in the tokamak plasma which is responsible for the poloidal magnetic field [27]. Two parameters represent effectiveness of the current drive: the tangential radius R_{tan} and the energy of the beam E_{beam} . The first has to be higher than the major tokamak radius $R_{tan} > R$, while the second should reach value of about 1 MeV to satisfy the ITER requirements [25]. The tangential radius is restricted by the exit injector's port size, which is placed between two toroidal magnetic coils. The beam energy depends on the applied acceleration voltage. Eventually, the estimated value of the current drive produced by NBI in the ITER reactor is between 1.8 and 2.8 MA [28].

The main drawback of the NBI system based on the acceleration of negative ions is their production and following extraction from the plasma. The negative ions are

produced in a low pressure plasma source (< 0.3 Pa) with a bulk plasma density $n_0 \sim 5 \times 10^{18} m^{-3}$. They are created via collisions into the plasma volume or by neutral gas/positive ions impact with the first grid of the extraction system called plasma grid (PG). However, a surviving length of the negative ions in such conditions is limited to few centimeters, thus only NI created in the vicinity of the plasma grid can be extracted. Moreover, the negative ions can be destroyed by the collisions with other particles (H_2, e) even after their extraction. Considering all the difficulties mentioned above, the ITER NBI plasma source is designed to produce 40 A extracted current and 200 A/m² current density of negative ions [16, 29]. During the neutralization procedure the negative ion current significantly decrease. Thus, ITER NBI system will deposit 16.5 MW neutral beam with energy 1 MeV.

The ITER neutral beam injector consists of four main parts: the source, the acceleration grids, the neutralizer and the residual ion dump (RID), see Fig. 2.1. In the source region negative ions are produced and extracted through the large number of small apertures made in the extraction grids. They are further accelerated to the energy of 1 MeV in five stages through the accelerator grids. In the neutralizer, most negative ions are converted into neutrals via collisions with deuterium (D_2) gas. After, a set of parallel plates biased such as they generate a transverse electric field which deflects all charged particles. It is the principle of the electrostatic RID system. Finally, neutral beam goes on the calorimeter or it is injected into the reactor vessel.

In the NI source region the hydrogen plasma is created by the radio frequency inductively coupled (ICP) coils. It diffuses in the expansion chamber and takes actual form there. To enhance the production of the negative ions, Cs atoms are introduced in the expansion chamber. The extraction system is placed at the end of the expansion chamber; it consists of two grids: the plasma grid (PG) and the extraction grid (EG). The first grid can be positively biased against the source (10 to 20 V) to reduce the fraction of the co-extracted electron current. A positive potential (~ 10 kV) is applied between EG and PG to drain out the negative ions, and to repel the positive ions. Each grid contains a bidimensional set of extraction apertures. The main problem of this system is the co-extraction of the plasma electrons. To limit the co-extracted electron current, a magnetic filter field is placed close to the PG. A second magnetic field, orthogonal to the first one, is generated by magnets embedded in the EG in order to deflect escaping electrons towards the grid's wall. These magnetic fields are strong enough to trap the electrons, but they only slightly disturb the ions trajectories [30]. More details about NBI plasma source are presented in Sec. 2.2.

After the extraction, negative ions enter to the accelerator, where they increase their energy up to 1 MeV [32]. Two designs of the accelerator system have been proposed for ITER NBI: MAMuG (Multi-Aperture Multi-Grid) developed by JAEA, Japan [33] and SINGAP (Single-Aperture Single-Gap) created by CEA Cadarache [34]. The main difference between them is the number of accelerating stages and size of the apertures. The first one achieves the beam energy of 1 MeV in five steps (200 kV each), whereas the second does it in one pre-accelerating (40 kV-200 kV) step. The advantage of the SINGAP (Fig. 2.2) is its simple structure, because intermediate accelerating grids are absent. However, electrons are created inside the machine by a variety of collisions [35], and are accelerated to full energy. Therefore, the efficiency of power consumption is decreased. Moreover, these energetic electrons cause extreme heat load on the beam line

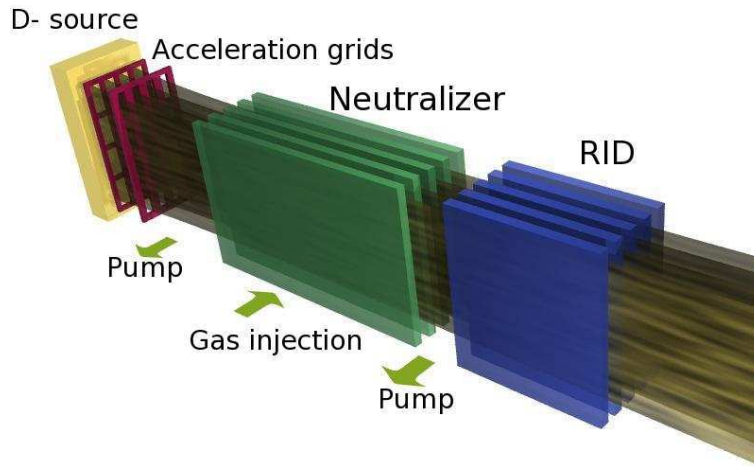


Figure 2.1: Schematic view of the ITER Neutral Beam Injector

components. On the other hand, MAMuG accelerator has a more complex structure, but undesirable electron beam can be suppressed by the intermediate grids before it gains full energy. The experiments show that power carried by electrons is much higher at the end of the SINGAP accelerator than in the MAMuG system [36, 37]. Consequently, the five stage machine has been accepted as the reference design for the future ITER NBI accelerating system.

The MAMuG accelerator as used in the Japanese test facility includes four intermediate grids (A1G, A2G, A3G, A4G) and the grounded grid GRG (Fig. 2.3) [39]. Each grid has a set of apertures of 16 mm diameter arranged in matrix. The negative ions are accelerated by the potential difference between two successive grids. One accelerating potential step is 200 kV, thus the total energy gained by the NI is 1 MeV.

One of the problems in such system is the production of D^+ by NI stripping in interaction with the neutral gas D_2 . It leads to the backward acceleration of the positive ions that causes additional heat load on the accelerating grids (3.6 MW/m^2 [36]) and can also damage the NI source wall. This problem has been partially resolved by adding the water cooling component inside the grids. However, the suppression of both, co-extracted electrons and the backward positive ion remains a challenging task.

From the accelerator the high energetic negative ion beam penetrates into the neutralizer, where NI are mainly converted in neutrals via the stripping collision. The D_2 gas neutralizer has been chosen for the ITER NBI due to its relatively simple structure and important stripping cross section. The alternative concepts of the neutralizer are: the plasma neutralizer [40], the lithium neutralizer [41] or the neutralizer based on photodetachment using intense laser beams [42]. The D_2 neutral gas is injected in the middle of the 3 m long neutralizer to have a relatively smooth profile of the gas targets all along. In order to reduce the gas flow, the neutralizer is divided onto 4 channels separated by copper plates (Fig. 2.4). Each wall measures 3 m long, 1.7 m high, and the gap between the plates is 10.5 cm. The water cooled swirl tubes are embedded inside the plate to limit the wall temperature [16].

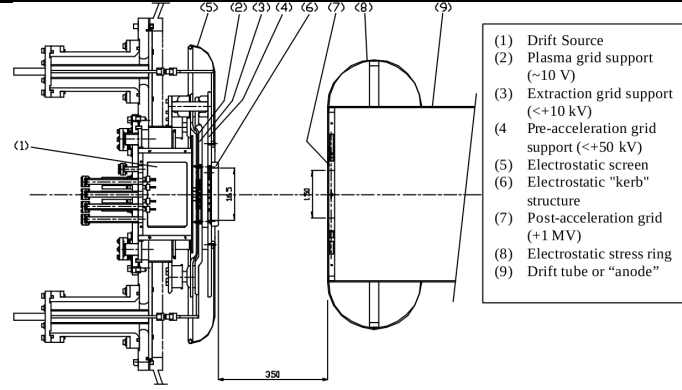


Figure 2.2: The cross-section of the SINGAP accelerator [38]

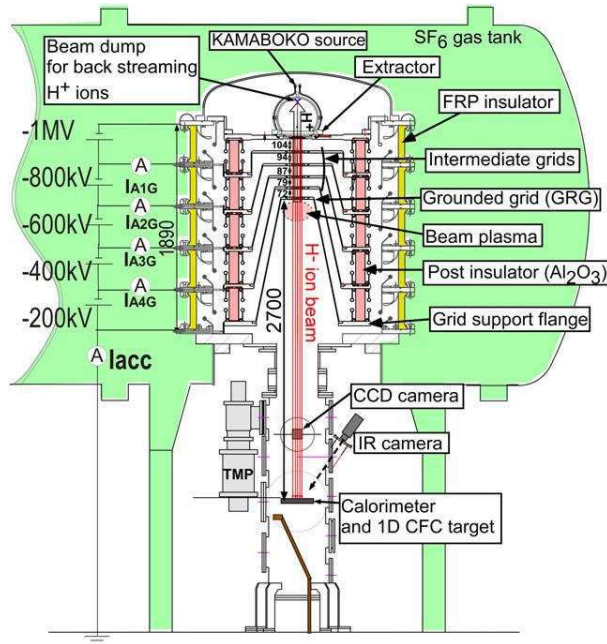


Figure 2.3: The cross-section of the MAMuG accelerator in the Japanese test facility [39]

The most important reactions that occur in the neutralizer are:



The neutral deuterium D_0 beam is created by the stripping of the weakly bounded electron from the negative ions (Reac. 2.1a). The double stripping reaction leads to the direct production of D^+ (Reac. 2.1b). The D_0 particles beam can be also destroyed by ionization giving D^+ as well (Reac. 2.1c). Moreover, the efficiency of the beam neutralization is decreased by the indirect gas heating process ???. Theoretically, the

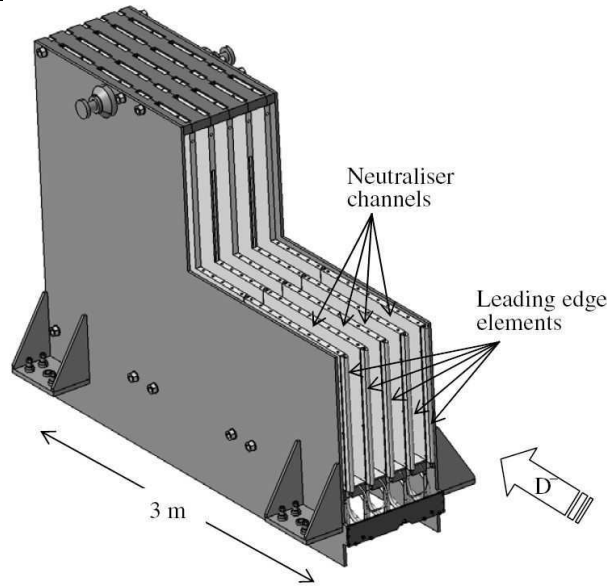


Figure 2.4: Cutaway ITER NBI neutralizer system [16]

beam with the energy of 1 MeV passing through the optimum gas target at the exit plane of the neutralizer is composed of $\sim 56\% D_0$, $\sim 23\% D^+$ and $\sim 21\% D^-$ [16].

The charged particles surviving in the neutralizer are deflected from the beam by the electrostatic residual ion dump (ERID) system. It has a structure similar to that of the neutralizer and consists of 4 narrow channels formed by 5 vertical panels. Each panel has the same high as the neutralizer plates, it measures 1.8 m long in the beam direction, and two plates are separated by about 10 cm [16]. The transverse electric field, which is created by a potential difference between two neighboring plates, traps charged particles. The first, third and fifth panels are grounded, whereas the -20 kV is applied to the second and fourth panels. The particles are deflected onto the plate's walls, with the power deposition of about 17 MW across the surface. The water cooled swirl tubes are placed inside the panels in order to decrease the heat load.

The ERID system has advantages over more conventional magnetic residual ion dump design (MRID). First of all, the power load of the deflected charged particles will be distributed among 5 plates. The second advantage of the ERID is the absence of the strong magnetic field that may affect the charged particles outside the machine. The main disadvantage of the ERID is the secondary electron emission in the collision of positive ions with the panel's walls. These electrons will be accelerated towards the opposite plate up to 20 kV, causing additional power load. Another problem may be plasma formation inside the channels that will screen electric field and, therefore, decrease efficiency of ERID. However, the numerical models show that the density of the created ions between two plates is 2 orders of magnitude smaller than critical threshold of the plasma production [44]. The last issue of ERID is formation of the hot spots at the walls due to inhomogeneous ion dump. However, recent numerical calculations [45, 46] have proven that maximum peak of the power load at the wall is lower than 8 MWm^{-2} , which is acceptable from an engineering point of view.

After the ERID system the neutral D^0 beam passes to the V-shaped calorimeter

formed by two panels. The calorimeter is 2.6 m long in the axial direction, with an open end 531 mm wide facing the ERID system [47]. Such configuration gives a possibility of an independent exploitation of the NBI system from the ITER reactor. The panels can be fully opened, thus the beam moves through the calorimeter to the NBI duct and further to the reactor vessel. The calorimeter allows performing measurements of the neutral power coming to ITER, as the difference between the power arriving to the calorimeter and downstream losses. In spite of energies losses during all stages of the beam formation in the NBI system the neutrals should be injected into the ITER tokamak vessel with the power ~ 16.7 MW.

2.2 ITER Neutral Beam Injector Plasma Source

Two types of the negative ion plasma source have been tested for the ITER NBI: the arc [48, 49] and the radio-frequency driven source. The latter one, developed by IPP Garching, Germany [50, 51] has been chosen as more appropriate, because it does not require the regular filament replacement. This is an important issue for the reactor, since NBI and consequently the ion source will be remotely operated during the ITER discharge.

Nowadays, there are few ion source machines developed at IPP: BATMAN (Bavarian Test Machine for Negative Ion), MANITU (Multi-Aperture Negative Ion Test Unit), RADI and under construction ELISE (Extraction from a Large Ion Experiment) [52]. They have different dimensions relative to the ITER requirements, but similar design. The Fig.2.5 shows schematic set-up of the negative ion source system. It consists of three main parts: the driver, the expansion chamber and the extractor. The plasma is generated in the driver by inductively coupled radio-frequency coils. The driver of BATMAN machine is represented by alumina cylindrically shaped of 140 mm long and 245 mm diameter. The coils are rolled around the driver and connected to the 1 MHz high power supply (~ 100 kW) oscillator. The D_2 or H_2 is injected inside the driver and it diffuses together with the ICP plasma in the expansion chamber. Neutral gas (D_2 or H_2) is pumped after the accelerator.

The expansion chamber has rectangular form with 6 mm steel wall and 3 mm drilled water cooled channel inside the wall. For the better heat distribution the inner wall of the chamber is covered with a thick copper layer. A compact form of the source allows easier installation of any external magnetic system. The pressure inside the chamber is kept at low level (about 0.3 Pa) to satisfy the stripping losses criterion [50, 51].

The extractor is constructed by two grids – the plasma grid (PG) and the extraction grid (EG), with a positive potential applied between them, in order to extract negative and repel positive ions. The PG could be positively biased against the plasma reducing the fraction of undesirable co-extracted electrons.

In the ITER configuration each grid is represented as the lattice of 1280 chamfered apertures divided by 16 groups [32]. Each hole of the plasma grid has a conical shape with the inner diameter of 14 mm and chamfered edges with the angle of 45 degrees. The length of the aperture is about 2 mm. The extraction grid hole is much longer than PG (12 mm), because the permanent magnets bars are embedded into the wall in order to dump hot electrons. Moreover, the water cooling pipes are also placed inside this

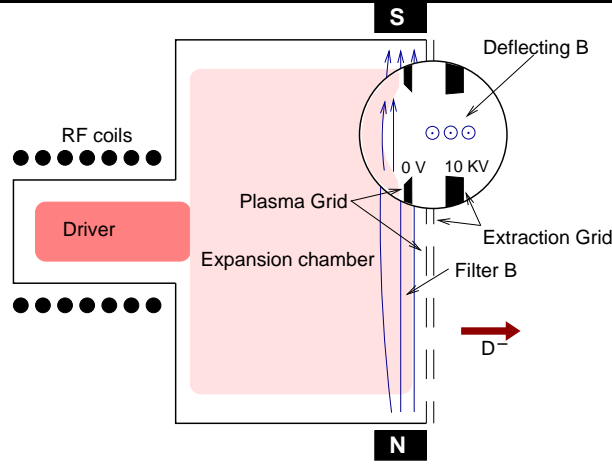


Figure 2.5: Schematic set-up of the prototype radio-frequency negative ion source ITER NBI system

grid. The distance between two grids is 6 mm, whereas the distance from EG to the first accelerating grid is 2.5 mm. The detailed cross section of one single aperture channel of the extractor is presented in Fig. 2.6.

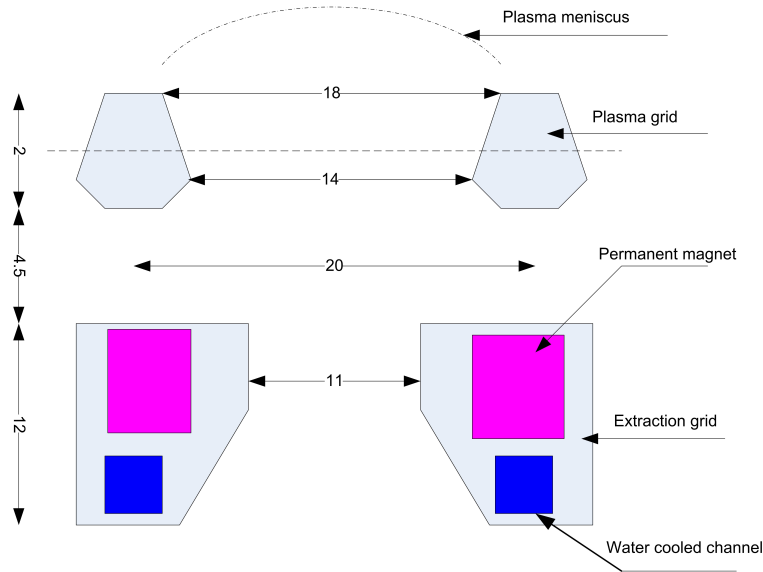


Figure 2.6: Geometry of the single extraction channel at the ITER source [16]

The production of the negative ions in the expansion chamber can take place via the collision of low energy electrons (about 1 eV) with the highly vibrationally excited hydrogen molecules (volume process) [53]:



At the low vibrational levels of H_2 the cross section of the reaction is low to produce sufficient amount of the NI, but starting from the vibration level $v = 5$ it increases by 5 orders of magnitude and becomes constant for higher levels [54].

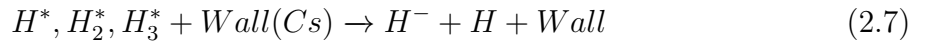
The concept of the negative ions in ITER NBI has been chosen due to their neutralization efficiency at high energy (~ 1 MeV), but on the other hand it makes the task of their production and extraction complicated. However, the life length (mean free path) of NI into the plasma is few centimeters [55] due to the variety of the destruction processes. The electron stripping collision is efficient at low electron temperature (in range of a few electronvolts) [54]:



It can be minimized by the reducing the electron temperature which is already $< 1eV$, but mutual neutralization collision will take occur (Reac. 2.4). Beside aforesaid destruction reactions, the associative and non-associative detachment are also important due to the low threshold value (Reac. 2.5 and Reac. 2.6 respectively) [53]. Consequently, only small amount of the volume produced negative ions can be extracted.



To enhance the NI production, *Cs* atoms are injected in the expansion chamber from the oven mounted at the back wall. The evaporation rate is about 10 mg/h controlled by the temperature of the oven. The cesium atoms will cover the plasma grid surface of the extraction system, therefore the production of negative ion will be fulfilled by the plasma-wall interaction process. The low work function of Cs (about 2 eV) allows increasing the amount of NI produced as backscattering of the positive ions H^+ , H_2^+ , H_3^+ or neutral gas H from the metal surface [53]:



The experiments show that evaporated *Cs* atoms increase negative ion extracted current by about 10 times [51]. The NI produced at the PG surface will move with high axial velocities towards the accelerator due to strong positive potential in this region.

One of the most problematic issues of the plasma source system is the co-extracted electron current. The electrons waste a huge amount of the accelerator power and causes additional heat load on the grid. To avoid electron current, a complex magnetic configuration is installed in the extraction region of the plasma source chamber. The first magnetic field is called "Filter field" and is created by magnets placed above the plasma grid with the strength peak value of about 7 mT. The second field ("Deflecting field") is generated via the magnets bars embedded in each aperture of the extraction grid with $B_{max} = 130$ mT. Both fields form complex orthogonal magnetic configuration that is strong enough to sufficiently trap the electron beam. However, it only slightly disturbs the negative ions trajectories due to their high mass.

2.2.1 BATMAN Experimental 1/8 Size ITER Negative Ion Source Test Bed

The Bavarian Test Machine for Negative Ion was designed and built at IPP Garching in order to prove the feasibility of the ITER requirements in terms of the extracted NI current and current density during short pulse length (~ 4 s) [57, 58]. The BATMAN machine was also used to develop a set of diagnostics for the most important plasma characteristics. Among them: optical emission spectroscopy – to measure density and temperature of the electron, Cs atoms and neutral gas; Langmuir probes – to detect local plasma parameters; laser detachment – to determine density of the negative ion [50, 52].

BATMAN machine has similar structure to the one described in previous section. However, it can use two different extraction systems. The first one is called “CEA”; and was developed at CEA Cadarache, France. The second one is “LAG” (Large Area Grid) [59], and was derived from the NBI positive ion based source machine used on ASDEX Upgrade tokamak [60]. The CEA grid was constructed according to the ITER NBI source design with diameter of the plasma grid aperture of 14 mm. 45 apertures form the total extraction area of about 70 cm^2 . The LAG system has much larger extraction area of 390 cm^2 , and it is composed of 774 small apertures with the diameter of 8 mm. However, the LAG grid was masked down to 74 cm^2 of the extraction area. All apertures are chamfered at the edge in order to increase the efficiency of the negative ion production and extraction from the plasma grid wall.

Several days of machine operation are needed to achieve so called “good Cs condition”, when cesium atoms thoroughly cover the plasma grid surface. Typical results of the extracted negative ion current density and electron/ion ratio from the hydrogen plasma are shown in Fig. 2.7 [52]. The yellow cycles represent the LAG accelerating system, whereas the blue triangle – the ITER like CEA grid. The NI current density reaches the value of about 25 mA/cm^2 in both configurations, which is close to the ITER requirement of 28 mA/cm^2 . The electron/negative ion current ratio is maintained around 1, which also meets the ITER condition.

The other purpose of these experiments was demonstrating that value of the extracted negative ion current does not depend of the aperture size. As it was mentioned above the extracted currents from both system: LAG with 8 mm aperture’s diameter and CEA with $d = 14$ mm are in very good agreement.

The BATMAN test bed machine has shown the possibility of achieving the ITER criterion in terms of high negative ion extracted current at the low pressure plasma (< 0.4 Pa). However, the extraction is limited by the short discharge time (about few seconds) due to technical reasons. Therefore, another source called MANITU has been built to satisfy the ITER requirement of 3600 s of continuous operation. This system will be described in detail in the next section.

2.2.2 The MANITU Experimental 1/8 size ITER Negative Ion Source Test Bed Machine

The short pulse length limitation of the BATMAN test bed machine has been solved via installation of additional cooling systems. The temperature control of all source walls was developed by IPP Garching in new test facility called MANITU. The water cooled

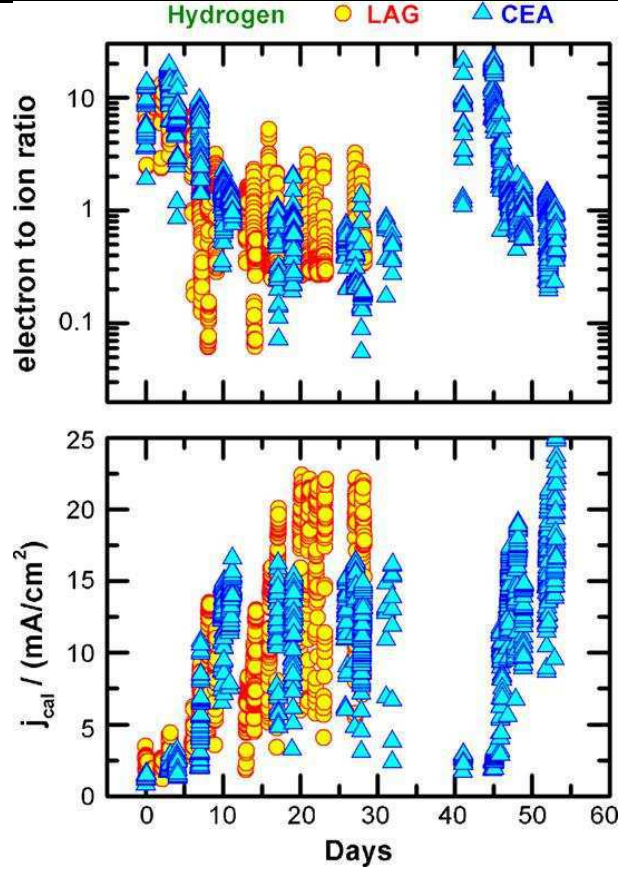


Figure 2.7: Accelerated negative ion current densities via CEA (yellow circle) and LAG (blue triangle) acceleration systems from the hydrogen source plasma (at the bottom). The electron/negative ion current ratio is shown at the top [52]

system was applied to the Faraday shield (used to protect the inner wall against the plasma load), as well as to the driver's backplate. The temperature in this region is held less than 18°C . The temperature of the interior part of the expansion chamber is also reduced by the water tubes located inside the wall ($< 40^{\circ}\text{C}$). The PG of the extractor is cooled by the airflow passing through the grid, allowing to decrease its temperature to 150°C [30]. After the aforesaid modifications the long discharge (~ 1 hour) operation becomes possible without any thermal disruptions.

The Cs evaporation control is another problem of the stable long pulse NI extraction. The production of the negative ions depends on the Cs level inside the expansion chamber. The remote temperature control system was installed in the Cs oven that allowed the adjusting of the injection rate during the long operation.

MANITU test bed uses the same negative ion source as BATMAN, where plasma is produced in the "driver" by inductively coupled radio frequency coils. The magnetic crossed configuration was also derived from the BATMAN machine. However, the plasma grid of the extractor is represented by LAG system with aperture diameter of 8 mm, hence total extraction area is 206 cm^2 . The plasma source operates also at the low pressure plasma (about 0.3 Pa). The MANITU facility is equipped with the diagnostics that was used in BATMAN, but with a data acquisition system, which allows to record long

discharges.

An example of the MANITU long pulse performance is shown in Fig. 2.8 [61]. The pulse duration of about 3600 s satisfies one more ITER requirement. However, due to the high electron current coming to the plasma grid the power of the radio frequency driver has been limited, resulting in small negative ion current density (12 mA/cm^2). Yet, during relatively short discharges ($< 200 \text{ s}$) it can reach the maximum value of 25 mA/cm^2 . The suppression of the electron current is still a challenging task and requires further optimization of the magnetic filter and potential distribution inside the chamber.

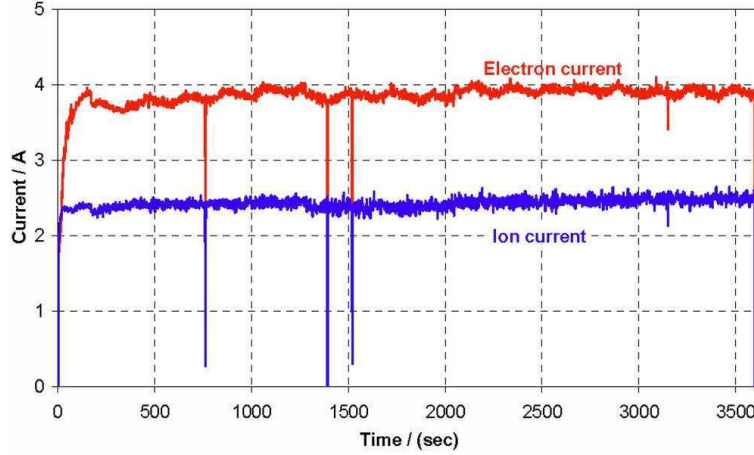


Figure 2.8: The example of 1 h Hydrogen plasma run on the MANITU test bed machine. The blue line shows the extracted negative ion current. The red line corresponds to the co-extracted electron current [61]

2.2.3 RADI – Experimental Source Machine with Large Plasma Area

The extending of the dimensions of the RF plasma source to the ITER requirements was fulfilled in RADI machine. Four driver systems have been combined in RADI, hence the roughly half-ITER size plasma source was constructed. However, the machine does not include the extraction system as previous BATMAN and MANITU test facilities. The RADI source can operate with both hydrogen or deuterium plasma and has possibility for Cs gas seeding. The main purposes of RADI are study of the plasma uniformity and demonstration of the concept of the modular source extension.

Fig. 2.9 presents one of the main result from the RADI experiments. The total positive ion density distribution in horizontal a) and vertical b) directions for different magnetic field intensity is shown. The hydrogen plasma has been studied under the pressure of 0.6 Pa with the power of 40 kW per driver. If we do not take into account the plasma decay close to the edge, the plasma distribution is almost homogeneous along the machine within about 10 percent of the error bar in both horizontal and vertical directions.

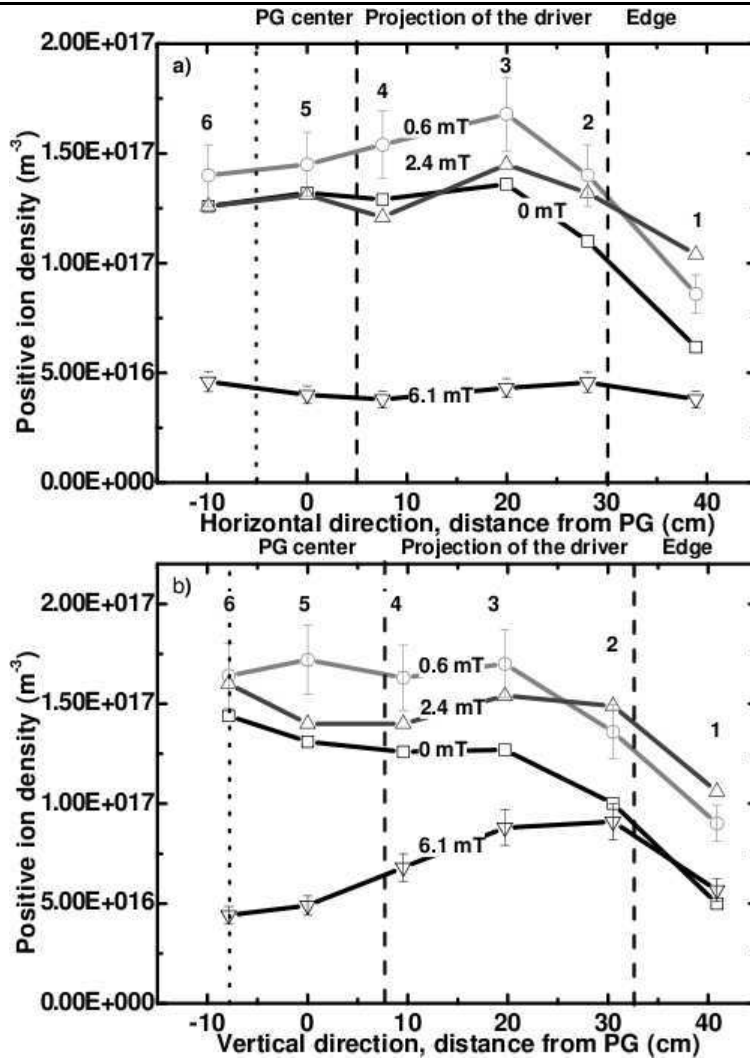


Figure 2.9: a) - Positive ion density distribution in the horizontal direction for different magnetic field strength; b)- Positive ion density distribution in the vertical direction for different magnetic field strength. Pressure of 0.6 Pa and power of 40kW per driver have been used [31]

2.2.4 ELISE – the Half-size ITER Negative Ion Source Test Bed Machine

The ELISE [62] will be the future experimental facility of the negative ion source with a large extraction area including extraction system. The machine is an intermediate step between the existing relatively small BATMAN, MANITU and the full size ITER NBI source under construction at RFX Padova Italy. The main goal of ELISE is to demonstrate the possibility of the negative ion beam formation uniformly distributed over a large extraction area. The suppression of the co-extracted electron current is also an important issue for ELISE.

The machine is designed as half size of the ITER NBI system with are dimensions of $1.0\text{ m} \times 0.86\text{ m}$ and 1000 cm^2 extraction area. The extraction is restricted to 10 s due to

the limitation of the high voltage power supply. The source will be able to operate with both hydrogen and deuterium plasma.

The ELISE's design is similar to that of previous test machines, the advantages of which have been reproduced in this new design on a higher scale. The plasma will be created in 4 cylindrical aluminum drivers with the inner diameter of 30 cm via inductively coupled coils wound around the cylinder. The extractor consists of three grids: the plasma grid, the extraction grid and the grounded grid. The large extraction area of 640 apertures is divided in 8 groups. The plasma grid aperture has 14 mm diameter with chamfered edges of 45° , whereas the aperture of the extraction grid is designed with the diameter of 12 mm. The grids are equipped with a cooling system allowing to reduce of the electrons heat load. Therefore, the highest temperature of the plasma grid should not exceed 200°C , while the extraction grid is referred to 50°C [62]. The water cooling tube is also installed inside the expansion chamber's wall that allows to keep their temperature around 50°C . Such temperature conditions have been chosen to maximize the negative ion yield based on the previous experimental works.

The co-extracted electron beam will be dumped by a complex magnetic geometry. The field will be produced via 8 kA current flowing through the plasma grid [62].

The main characteristics of the ELISE machine together with the parameters of the BATMAN and MANITU facilities are summarized in Tab. 2.1 [50, 51, 52, 30, 61, 62]. The start-up of the new testbed negative ion source is planned for the end of 2011 [63].

Table 2.1: Main parameters of the NBI negative ion source facilities [52, 16]

Parameter	ITER requirements	BATMAN results	MANITU results	ELISE prospect
Extracted current density H^-	280Am^{-2}	$\sim 240\text{Am}^{-2}$	$\sim 200\text{Am}^{-2}$	-
Extracted current density D^-	200Am^{-2}	$\sim 200\text{Am}^{-2}$	$\sim 200\text{Am}^{-2}$	-
Extraction voltage	9kV	9kV	9kV	12kV
Source pressure	0.3Pa	$< 0.4\text{Pa}$	0.3Pa	-
Electron-ion ratio	1	< 1	< 1	-
Pulse length	3600s	$< 6\text{s}$	3600s	$\sim 10\text{s}$
Source dimension	$1.5 \times 0.6\text{m}^2$	$0.32 \times 0.59\text{m}^2$	$0.32 \times 0.59\text{m}^2$	$1 \times 0.86\text{m}^2$
Extraction area	0.2m^2	70cm^2	206cm^2	1000cm^2

2.3 Numerical Approaches for Plasma Source Modeling

The negative ion approach for the formation of the neutral beam still requires understanding the physics of the electronegative sheath, when electrons and NI are pulled out from the plasma. Several numerical studies of the plasma behavior around the extraction region have been published in recent years, including the Monte Carlo transport calculations and 1-3D PIC simulations. Each code was developed to demonstrate particular

physical effects inside the source. Among them: production of the negative ion in the volume and by the plasma-wall interaction process; effect of the external positive potential and magnetic configuration on the extraction of the negative ion and electron currents; study of the aperture geometry and the beam optics. In this section, the recent numerical approaches will be described together with their simulation results.

2.3.1 2D Fluid Simulation of the Plasma Source

The two-dimensional fluid model was developed in the LAPLACE laboratory in Toulouse, France, in order to estimate plasma parameters at the ITER NBI source region [64, 65]. The code is mainly devoted to understand the properties of the plasma in the ICP type source. The model is able to calculate the density and temperatures distributions of different species, energy balance, plasma potential, particles flux to the wall, etc. The simulations based on the transport of the charged particles (e , H^+ , H_2^+ , H_3^+) and neutral gas (H , H_2) were performed at the various initial pressure (0.2 – 0.8 Pa) and power (10 – 80 kW) conditions.

The transport of the charged particles is performed by solving the continuity, the momentum and the energy equations. The Navier-Stokes equation is used to introduce the motion of the neutral gas via the Direct Simulation Monte Carlo (DSMC) algorithm. The potential distribution is self-consistently obtained from the equation of Poisson. The large list of volume reactions is included in the simulation using the Monte Carlo approach. However, the present model does not involve the production of the negative ions from the plasma grid wall. Thus, the code does not resolve the negative sheath in vicinity to the extraction system, which is a subject for future improvement.

The typical results of the density distribution along the simulation domain are shown in Fig. 2.10. Concentration of the electrons and H_2^+ is dominant in the beginning of the simulation volume that corresponds to the source "driver", whereas the densities of the H^+ and H_2^+ in the expansion chamber are nearly the same. The density of the H_3^+ is small everywhere relative to other particles, Fig. 2.10 (a). The distribution of the neutral gas density is presented in Fig. 2.10 (b). The concentration of the hydrogen molecules is shown in two cases: with and without the plasma for the same gas flow. The densities of both H and H_2 in the expansion chamber are significantly lower than close to the driver, when the plasma is turned on. It has been proved that there are mainly 2 mechanisms corresponding to this density drop in the chamber: 1) gas hitting and 2) depletion of the gas density due to high ionization degree [65]. However the simulation results are lower than in the experimental measurements [50, 51].

2.3.2 SLACCAD 2D Monte Carlo Code

The SLACCAD code was derived from the early transport model called SLAC, which is devoted to simulation of the positive ions based plasma source facility [66]. The code is a two-dimensional one; it uses Monte Carlo approach coupled with Poisson Solver in order to estimate the electric field inside the accelerator of the ITER NBI. The developed model is dedicated to the study of extraction beam optics in the presence of the magnetic field [67]. The SLACCAD code is able to follow only the trajectories of the negative ions, thus the electrons behavior is not considered. However, the electron stripping collision is

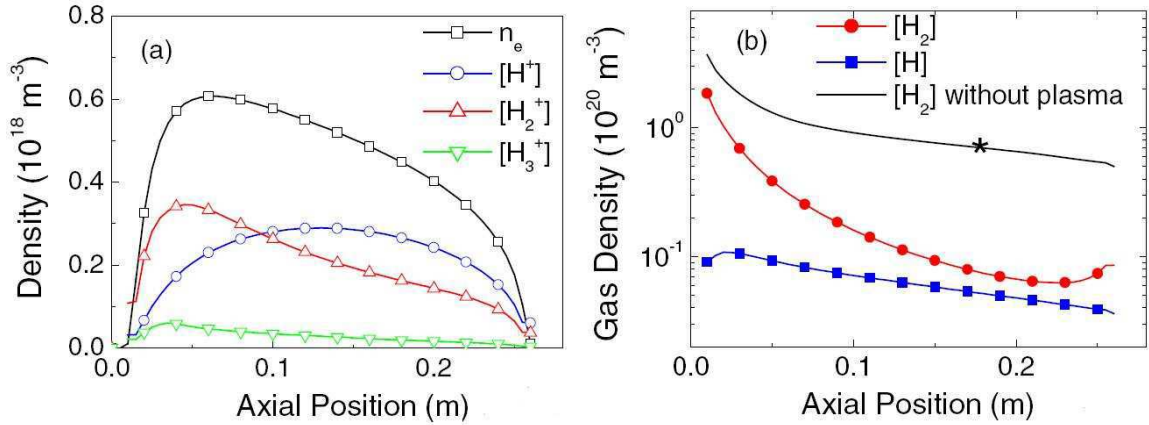


Figure 2.10: The density distribution of the charged particles (a) and the neutral gas (b) along the simulation domain of the NBI plasma source (0 m corresponds to the driver position). The constant values of the pressure – 0.3 Pa and the power 60 kW were used in all simulations [65]

taken into account. Another limitation of the code is the absence of the filter magnetic field in the extraction region and the treatment of only the deflecting one due to the choice of 2D simulation.

An example of the negative ions trajectories is shown in Fig. 2.11 [68]. The aperture of the plasma grid has 14 mm diameter, whereas the extraction grid – 12 mm, as in the ITER NBI source design. The positive potential of about 10 kV is applied between the PG and EG, when the ground plate is set to 100 kV. The simulation gives the maximum extracted H^- current density of 34.2 mA/cm^2 that could pass through EG without any beam destruction.

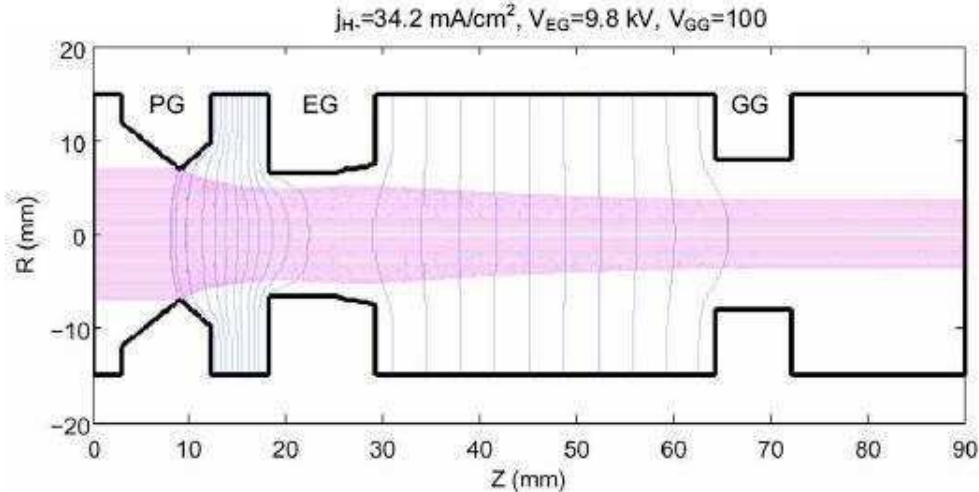


Figure 2.11: The negative ion trajectories (magenta) calculated by the SLACCAD code. Blue lines indicate the external positive potential distribution [68]

The parametric study of the aperture geometry and external potential has been also performed using the SLACCAD code in [69]. The NI extracted current densities have been calculated at the potential of $7kV$ and $5kV$. The different inner diameters of the PG orifice have been tested. The calculation shows that smaller aperture size is the cause of the rise of the negative ion current density. 16, 25 and 35 mA/cm² have been obtained during the simulation of 14, 11 and 8 (mm) aperture's diameter respectively, using 7 kV of the external potential. The same behavior of the extracted NI current density has been demonstrated with 5 kV extraction potential. However, the experimental measurements presented in Fig. 2.7 show no difference of the extracted negative ion current density when the diameter of the aperture is decreased from 14 to 8 mm [52].

2.3.3 EAMCC 3D Monte Carlo Code

The Electrostatic Accelerator Monte Carlo Code (EAMCC) is a three-dimensional relativistic transport code for simulation of the beam trajectories in the accelerator region of the ITER NBI system [35]. The current model does not calculate the electric or magnetic field in self-consistent manner. They are taken as input parameters from the SLACCAD results described above. In the calculation macro particles are launched from the meniscus region close to the plasma grid, thus the code could record full 3D extracted negative ions or co-extracted electrons trace along the accelerator. Each macro particle represents an array of real ions and typically carries on current of about 50 nA. The collisions in the model are resolved via the Monte Carlo approach. Among them: an interaction of the electrons, ions and neutrals with accelerating grids; the stripping and double stripping negative ion reactions; ionization of the background gas.

The main results from the EAMCC modeling are presented in Fig. 2.12 [68]. The NI are injected with the total current density of 34.2 mA/cm^2 [70]. The trajectories of the negative ions and produced species are shown in Fig. 2.12 (a) for a single beam component. The power heat load on each grid from different particles has also been calculated. The total power load of the transmitted beam detected in the end of the extractor, that corresponds to the whole accelerator system with 1280 apertures (see Sec. 2.2), is 6340 kW, including: 5550 kW of H^- + 490 kW of e^- + 10 kW of H^+ . The total back-streaming power of the positive ions at the plasma grid plane is 90 kW composed by 10 kW of H^+ and 80 kW of H_2^+ . The electrons heat load on the extraction and grounded grids is 31 kW and 169 kW respectively.

Fig. 2.12 (b) presents the trajectories of the co-extracted electron beam. Due to the reference ITER value of the electron/NI current ratio ~ 1 [16], the electrons are launched with the same current density (34.2 mA) as the NI in previous calculation. Most of the electrons are dumped onto the extraction grid due to the strong magnetic field in this region. Therefore, co-extracted electron power load on the extraction grid is 632 kW, whereas the grounded grid consumes only 78 kW. The same system behavior has been detected in the experimental measurements where most of the electron deflected onto the EG.

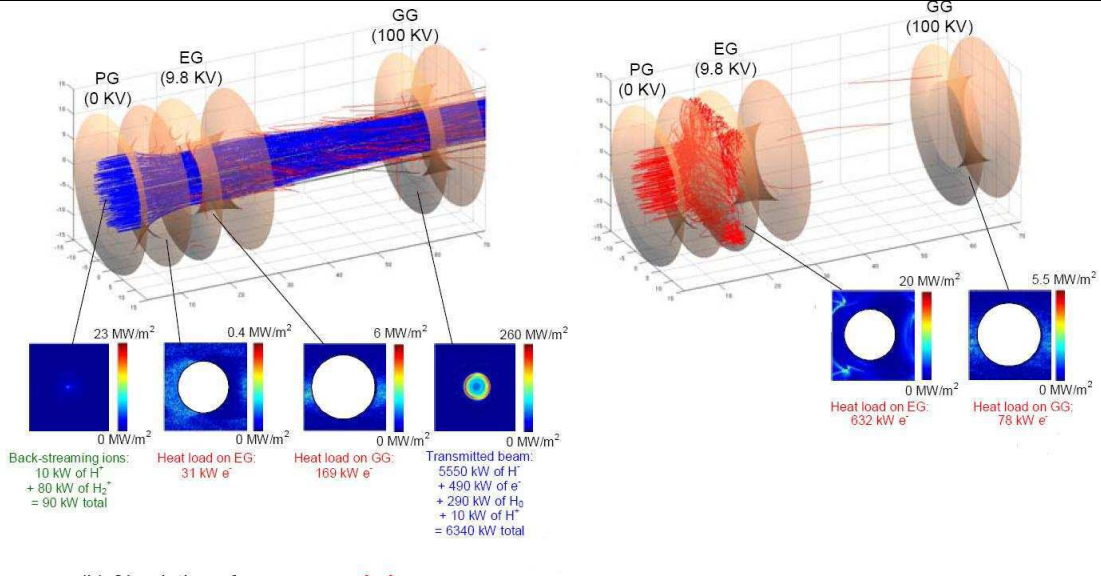


Figure 2.12: Negative ion (a) and electron (b) trajectories calculated by the EAMCC code. The power heat load on each grid corresponding to the whole accelerator system (1280 beamlets) is presented at the bottom [68]

2.3.4 Monte Carlo Code TRAJAN

The other trajectories analysis, the Monte Carlo code TrajAn, was developed in IPP Garching [71, 72, 73]. The code is three-dimensional one and is devoted to simulate the extraction probability of the negative ions and electrons in the extraction region of the NBI plasma source. The simulation domain includes multi set of the plasma grid apertures with the specific chamfered geometry of the LAG extraction system, which was described in the Sec. 2.2.1. The double-crossed magnetic field distribution is taken into account, whereas the electric field component is borrowed from the Ray Tracing KOBRA3 [74] code. The collisions between the particles are resolved via the Monte Carlo path length estimation algorithm. To push the charge species the modified Lorentz equation is solved by the Runge-Kutta method [72].

In Fig. 2.13 (a) the parametric study of the initial negative ion energy is shown in 2 configurations of the plasma grid geometry: with chamfered and flat aperture's edges. The extraction probability of the surface produced negative ions strongly depends on their initial velocities. At the higher starting energies the extracted amount of the negative ions decreases. It is especially visible at the energy less than 3 eV. The low initial velocity is the result of the long retention time of the negative ions close to the plasma grid aperture. This enhances the probability of the elastic collision that could change the particles trajectories towards the expansion chamber. The Fig. 2.13 (a) also presents the benefit of the chamfered aperture's geometry (as in ITER specification) over the flat shape. The extraction probability increases from the bend area due to the redirection processes, which leads to a more efficient ion transport.

The parametric study of the filter magnetic field strength is shown in Fig. 2.13 (b) at different negative ion initial energies. The extraction probability increases at high values of the filter magnetic field. The low initial velocity and strong magnetic field cause the

decrease of the negative ion's gyro radius. The destructive processes are inefficient at the small mean free path in the source plasma; therefore, it enhances the negative ion extraction [72]. The identical simulations were done for two magnetic configurations: with orthogonal magnetic field geometry and with only one - the filter field, when the deflecting one being turned off. The calculations show the absence of influence of the deflecting field on the extraction probability of NI. Because of its short range, deflecting field does not have big contribution of the total number of the redirected ions.

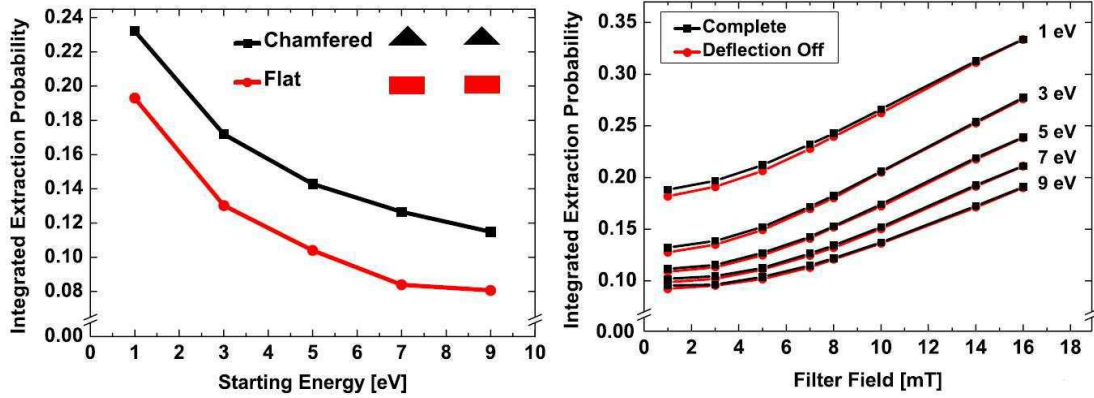


Figure 2.13: Calculated extraction probability versus initial energy of the surface produced negative ions in chamfered and flat configurations of the plasma grid aperture (a). The extraction probability versus the filter magnetic field strength for different starting ion energies (b) [72]

2.3.5 1-2D PIC Simulation of Negative Ion Extraction

1-2D PIC models of the negative ion extraction was developed to simulate the particles dynamics in the plasma source, close to the extraction region. The code is 1 – 2D Particle-in-Cell Monte Carlo Collision [75, 76, 77]. The distribution of the filter magnetic field is applied in the model as an initial parameter, whereas the electric field is calculated in a self-consistent manner. The Boris-Buneman [78] version of the leap-frog methodology is used in order to move the charged particles. The complete list of the particles collision reactions is considered in the simulation, which allows obtaining full picture of the kinetic dynamics in the plasma source. The production of the negative ions is fulfilled via 3 atomic processes: (i) electron dissociative attachment to the vibrationally excited molecules H_2 (the densities of H_2 in different vibrational state are self-consistently calculated in the kinetic part); (ii) interaction of the positive ions with Cs covered plasma grid wall; and (iii) the neutrals impact with the PG.

The study of the bias potential effect that is used to decrease the co-extracted electron current is shown in Fig. 2.14. The densities distribution of the electrons (red lines) and negative ions (green lines) are presented in 2 cases: with 0 V (dashed line) and with 36 V (solid line) applied bias potential. In both calculations the magnetic filter field is considered with $B_{peak} = 4$ mT (different from the experiments ??) . In the simulation with positively biased plasma grid, the electrons density is reduced drastically in vicinity to the extraction orifice, which is in accordance with experimental results [58]. However,

the bias potential causes the simultaneous decreasing of the negative ions density at the distance ~ 1 cm from the PG.

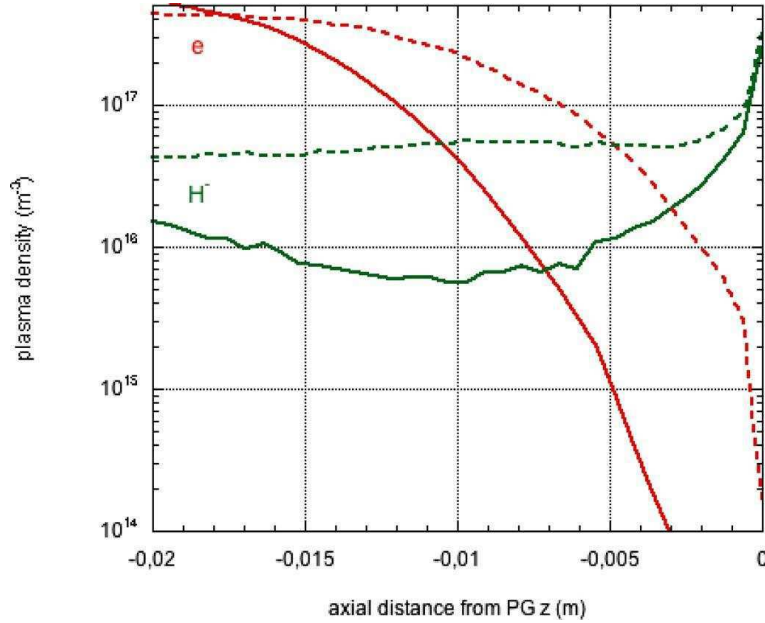


Figure 2.14: Distribution of the electron and negative ion densities close to the plasma grid grounded (0 V - dashed line) and biased (36 V - solid line) [76]

The study of the external magnetic filter field effect is given in Fig. 2.15. The electron and negative ion density profiles are presented without consideration of the magnetic filter field (dashed line) and with $B_{peak} = 4$ mT (solid line). In both cases the plasma grid bias potential is set to the floating. The electron density decreases when magnetic field is switched on, whereas it almost does not have any effect on the negative ion profile. Moreover, the H^- creation in the bulk plasma increases from the electron dissociative attachment collisions due to the reduction of electron temperature by the magnetic field.

However, the low dimensions PIC simulation is not able to bring a quantitative description of the extraction problem. This happens because of the presence of the double-crossed magnetic fields that breaks up the cylindrical symmetry of the system close to the extraction aperture. Moreover, the external positive potential between plasma and extraction grids is not taken into account in the current model. This potential is much higher (~ 10 kV) than the bias one at PG ($\sim 20 - 40$ V) and it plays a crucial role in the “meniscus” formation. Therefore, in order to obtain a realistic simulation of the extractor further optimizations of the model are required.

2.3.6 Three-dimensional PIC Simulation

The first three-dimensional particle-in-cell simulation of the negative ion extraction was implemented in extended TRQR code [79, 80]. It is an electrostatic code, where the electric field is self-consistently calculated each time step. The fixed magnetic filter field distribution is also taken into account in the current model. The electrostatic potential is determined by solving the Poisson equation via the successive over-relaxation method [81].

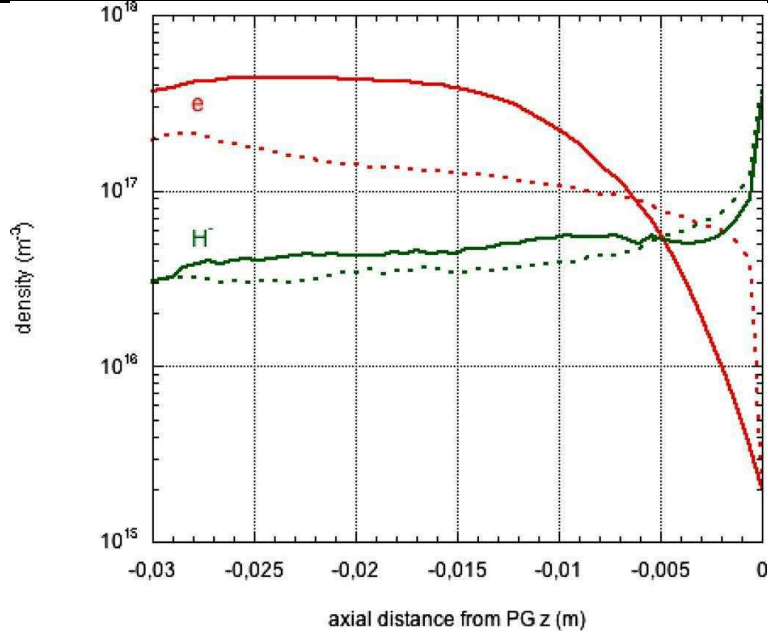


Figure 2.15: The electron and negative ion densities along the extraction axis without (dashed line) and with (solid line) magnetic filter field: $B_{peak} = 4$ mT. PG is grounded in both cases [76]

The motion of the charged particles was fulfilled by the 4th order Runge-Kutta algorithm. The random-walk diffusion routine was installed in the model to reduce nonphysical effect of the excessive electrons accumulation in the magnetic field region. This model focuses on the study of the extracted NI and electron currents using various configurations of the extraction potential and the magnetic field.

The parametric study of the external positive potential versus total extracted negative ion (a), and electron (b) currents is presented in Fig. 2.16 as a function of the simulation time. The results show simultaneous growing of the NI extracted current with the increasing of the extracted potential (Fig. 2.16 a). The same observation has been made for the co-extracted electron current (Fig. 2.16 b). However, the filter magnetic field emphatically traps the electron beam. Therefore, the values of the electron current are smaller in the end of the simulations, when the system is close to the steady-stay regime.

Nevertheless, the description of the aperture geometry in the current model is rather rough, because of the large value of the PIC mesh size used ($\Delta x = 0.1$ mm, $\Delta y = \Delta z = 0.75$ mm [79]). The low plasma density ($n_0 = 10^{16} m^{-3}$ [79]) and the magnetic field configuration used in the simulations are far from those which have been planned for the ITER source. Moreover, the collisions between the particles are not taken into account. Finally, significant modifications of the model are required in order to get realistic plasma description close to the extraction area of the ITER NBI source system.

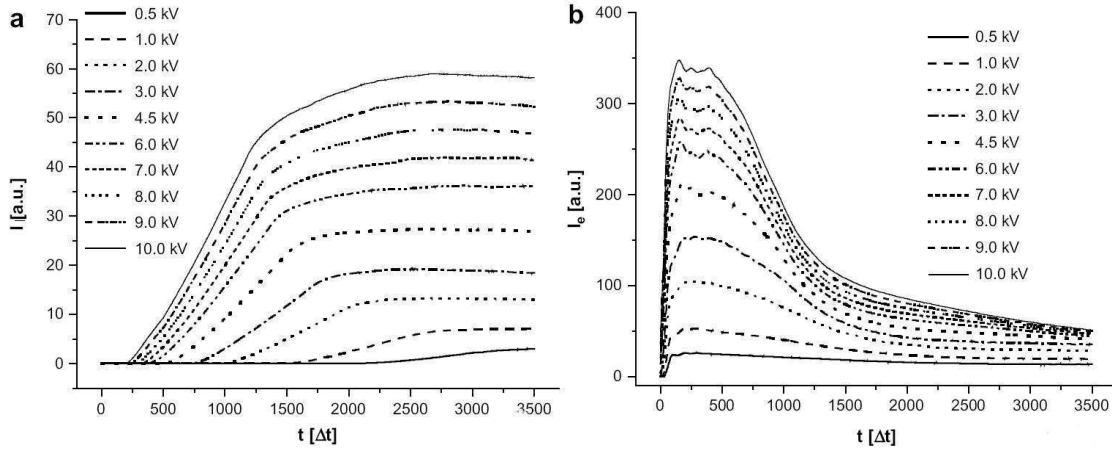


Figure 2.16: The evolution of the total extracted negative ion (a) and electrons (b) currents as a function of the simulation time [79]

Chapter 3

Numerical Approach

An electrostatic full 3D Particle-in-Cell Monte Carlo Collision code has been specifically designed to study negative ion extraction from the electronegative plasma in the Neutral Beam Injector source system. The code is called ONIX – Orsay Negative Ion eXtraction. It is a unique code for such a system that uses realistic descriptions of the applied fields and simulated aperture geometry. The code uses the Cartesian coordinate system and it can deal with a complex boundary geometry of the simulation domain, as it is in the case of the chamfered plasma grid aperture. The developed code is parallelized for distributed memory multi-CPU computers using the spatial domain and particle decomposition method via the Message Passing Interface technique.

This chapter presents the most important numerical approaches used in the ONIX program. The particle movement algorithm, giving the solution of the modified Lorentz equation, is presented. The Precondition Conjugate Gradient (PCG) method that is used for resolving the Poisson equation is explained. The simulation domain, mesh structure, initial plasma parameters, boundary conditions, etc. are shown together with the numerical limitation criteria. In the end of the chapter the code stability and validation results are presented and discussed.

3.1 Extraction Region and Simulation Domain

In the negative ion plasma source the extraction system is composed as the bi-dimensional array of 1280 apertures. However, it is computationally intractable to simulate the whole system, because of considerable need in real time and computer power. Therefore, we restrict the simulation domain to a single extraction orifice of the plasma grid (Fig. 3.1). Periodic boundary conditions are used in y and z directions (as in other similar codes) to model an infinite $2D$ array of the apertures. The transverse dimension of the simulation box is $20\text{ mm} \times 20\text{ mm}$, that corresponds to the distance between the center of adjacent apertures in each direction.

The choice of the simulation box length in axial x direction is a more complex issue. The idea is to use the length large enough to get a valid result, i.e. independent of the box size, but not too large to make the simulation unpractical from the computational point of view. It is assumed that the plasma properties in the expansion chamber are homogeneous, and the presence of the extraction apertures affects only the plasma properties in a small region around the plasma grid. In this region, usually known as the

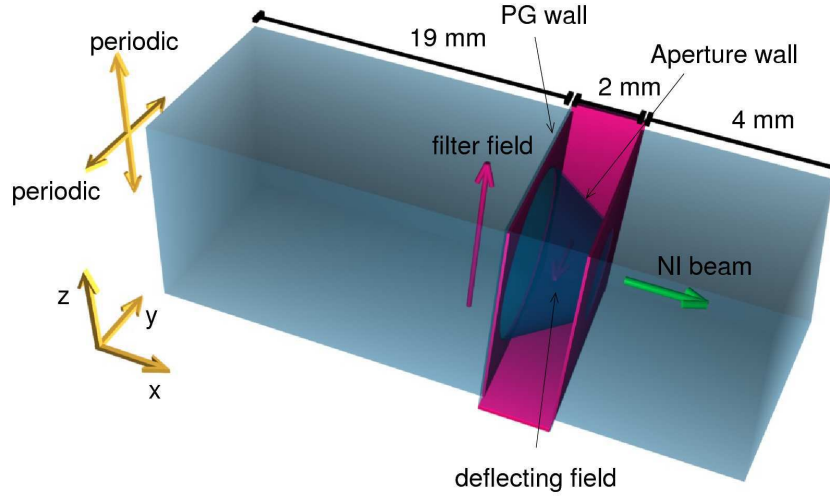


Figure 3.1: Schematic view of the simulation domain. The cross section in (y, z) plane is a square with side-length of 20 mm. The conical aperture has the larger diameter of 18 mm (plasma side - left-hand side) and the smaller diameter of 14 mm (extraction grid side - right-hand side)

”meniscus”, the space charge is significant. Different lengths of the domain have been tested to get a volume large enough on the left-hand side (before the PG) to include the neutral undisturbed plasma region that remains unchanged during the simulation. This region acts as an infinity reservoir. Simulations show that such conditions could be achieved beyond 7 mm inside the expansion chamber. Therefore, the left side of the simulation domain measures 19 mm, where plasma is placed between 0 and 12 mm from the beginning of the domain. The properties of the plasma (density and temperature) are assumed constant, and are taken from the experimental data ($n_e = 10^{17} m^{-3}$, $T_e = 3 eV$) [50, 51].

The cutoff distance of the simulation box after plasma grid is less critical. The border of the simulation domain from the right side is set at 4 mm away of the PG. To determine the potential in this plane to be used as a boundary condition in the Poisson’s solver, the vacuum potential of the whole extraction region (including EG) has been simulated (Fig. 3.2). In this calculation, the potential at EG is 10 kV, whereas the plasma grid is grounded. At the distance of 4 mm from PG, the potential isosurface is roughly flat, and its corresponding value is 6.8 kV. Therefore, the size of the simulation box is 25 mm \times 20 mm \times 20 mm in x, y, z directions (Fig. 3.1). The plasma grid is 2 mm thick and is centered in the $y - z$ plane at $x = 19$ mm.

In the first code version [83, 82] the cylindrical shape of the extraction aperture has been tested. However, its form has been improved to be closer to the real machine. Finally, the extraction aperture in the standard configuration is represented as a cone that corresponds to the chamfered orifice of the plasma grid (Fig. 3.1), with $R = 9$ mm and $r = 7$ mm.

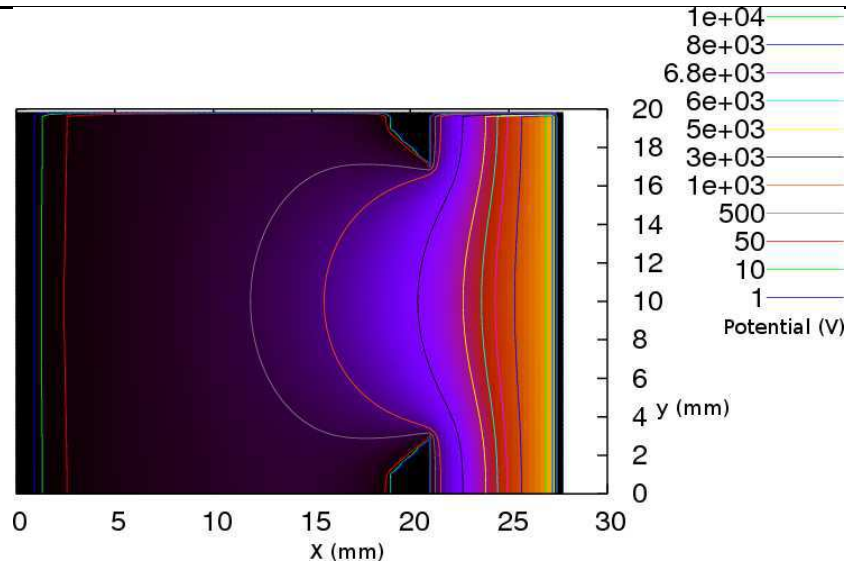


Figure 3.2: The potential distribution along the large simulation domain (including EG) without plasma. The right border plane represents the extraction grid

3.2 General Description of the ONIX Code

ONIX (Orsay Negative Ion eXtraction) is a full three-dimensional Particle-in-Cell electrostatic code in Cartesian coordinates. The code is dedicated to simulate the plasma behavior in vicinity to the PG orifice. It is the first 3D model of the extractor that uses the realistic topology of the magnetic fields. The code includes a simplified kinetics using MC collision approach. Hence, it takes into account the production of the negative ions via the electron dissociative attachment through collisions with the vibrationally excited molecular states $H_2(v)$ in the expansion chamber, as well as the production of the negative ions involving the Cesium layer which covered PG wall (i.e. volume and surface production). The most important negative ion destruction processes are also included in the model. Another specificity of the ONIX code is the possibility to model complex geometrical shapes, as it is in the case of the extraction orifice. In order to perform calculations which need reasonable computation time, the code is parallelized to distribute memory between multi-CPU computers using spatial domain decomposition via the Message Passing Interface protocol.

In the NBI plasma source system, the plasma and extraction grids are constructed with hundreds of small orifices. However, it is computationally intractable to simulate all of them at once. Therefore, a single aperture channel is simulated, with the assumption that neighboring orifices have the same properties. Nevertheless, the asymmetry induced by the complex orthogonal magnetic configuration requires full 3D modeling.

ONIX is an electrostatic code, where electric field is recalculated from the potential difference at each iteration step. The potential is obtained from the Poisson solver via the iterative Precondition Conjugate method [84]. The magnetic field distributions are taken from the experimental results [50] and are used as the constant input function.

The general chartflow diagram of the ONIX code is shown in Fig. 3.3. It is designed to give a basic overview of the numerical technique used in the code. The diagram also

explains the simulation algorithms in general terms. The first step of the process involves the assignment of the input data, allocation of the required memory and initialization of all variables and constants. During the initialization phase the necessary mesh structure and domain geometry are constructed. The initial plasma is loaded in the system. The first stage includes introduction of the MPI multi processor tasks, in particular, the amount of the required processes and their sub-domain boundaries. The boundary condition of the simulation domain is also set up here. The "initial.dat" file controls many input parameters for simulation and it is parsed during this step. After the initialization procedure, the main time iteration loop of the simulation begins.

The first step in this loop is the projection of the plasma particles charge (from the previous step) onto the PIC grid points. A linear interpolation algorithm has been used in order to distribute the particle charge among eight nearest cell nodes (detailed in Sec. 3.7).

The next step involves solving the Poisson equation. The charge density $3D$ matrix from step 2 is used in the Poisson solver to recalculate potential distribution along the simulation domain. A variation of the iterative Conjugate Gradient method is implemented in the model as one of the most suitable algorithms for such matrix size. The auxiliary precondition matrix has been used to speed up calculations (Sec. 3.8.2).

During the next step the electric and magnetic fields are calculated. The electric field is self-consistently calculated from the potential distribution in all three directions: e_x , e_y , e_z . The magnetic field is interpolated to get local value corresponding each particle location from the given constant function (Sec. 3.9).

Next, at each time step all charged particles are moved according to the electric and magnetic fields calculated in the previous procedure. The leapfrog Boris scheme is used in this step to push the particles. The detailed description of this method is given in Sec. 3.10.

The routine of particle interaction with the domain boundaries then follows. According to the simulation boundaries conditions, described in Sec. 3.4, the particles could be absorbed, reflected or extracted from the volume. The production of the negative ions from the Cesium covered plasma grid wall by the positive ion impact is also considered here.

The volume collision events are then calculated. During this phase the production of the negative ions in the expansion chamber is fulfilled. The collision procedure also includes a list of the most important NI destruction reactions and energy transfer collisions. More details about the particle collision module are presented in Sec. 3.11.

The particle migration between MPI processes is performed during the next step. If a particle moves out of a process, this particle will be deleted from this process and transferred to the neighboring one. The details about the MPI technique implemented in the model are discussed in Sec. 3.12.

All electrons and positive ions deleted from the simulation domain (extracted or absorbed in the PG wall) are randomly reinjected with the thermal energy in the initial plasma position range (Sec. 3.6). The production of the negative ions from the PG wall by the neutrals impact is implemented in the program as the given flux from the wall. This procedure is also fulfilled during the current step.

Regularly, in the main time loop, the output files are generated. They contain information about the density distribution of different species, extracted NI and electron

currents, the potential map along the volume, etc. The positions and velocities of all particles are saved each 20000 – 100000 iterations, in order to resume calculation in case of the sudden program shutdown.

Finally, when the specified simulation time elapses, the main loop is terminated and code finalization is executed. During this step the program deallocates all reserved memory and cleans up all temporary variables and files. The final results of the simulation are printed out.

3.3 Computation Parameters

Most of the plasma parameters are self-consistently calculated by the ONIX code. However, some physical characteristics of the plasma in the expansion chamber are required to start the simulation and they are taken from the experimental measurements described in Sec. 2.2.

3.3.1 Initial Plasma Conditions

In the standard configuration plasma fills the first 12 mm of the computation domain, where the same conditions as in the expansion chamber are assumed. Initially, the plasma is composed of electrons and positive ions: H^+ , H_2^+ . The negative ions are not present at the beginning of the simulation, but they are born during the run via various processes (described in details in Sec. 3.11). The properties of the plasma (density and temperature) are constant in this region; they follow the experimental data [50, 51] (Tab. 3.1).

Table 3.1: Main initial plasma parameters

Plasma density $n_e/n_{H^+}/n_{H_2^+}$	$1/0.6/0.4 \times 10^{17} m^{-3}$	[51, 65]
Electron temperature T_e (eV)	$T_e = 3$	[51]
Positive ions temperatur $T_{H^+}/T_{H_2^+}$ (eV)	1/1	[51]
Gas density n_H/n_{H_2}	$0.4/4 \times 10^{20} m^{-3}$	[51, 65]
Density of $H_2(v)$ ($5 \leq v \leq 9$)	$2 \times 10^{18} m^{-3}$	[76]

At $t = 0$, the spatial distribution of the electron and positive ions density is the same ($n_e = n_{H_2^+} + n_{H^+}$), i.e. the plasma is neutral. The primary H^+ density is shown in Fig. 3.4. As it has been mentioned above, the initial plasma is placed between 0 and 12 mm (the plasma grid inner wall starts at $x = 19$ mm). The rest of the simulation domain is empty.

The described initial conditions have been used in the code in most of simulations. However, these parameters have been adjusted for each program run depending on the aim of calculation. The different domain size (from 20 mm to 40 mm) and aperture geometry (conical and cylindrical) have been tested. Some calculations included the negative ions in the initial plasma state from 1 to 10 percents of the bulk density. Several values of the plasma temperature, density and position of the initial plasma "reservoir" have been simulated. The differences with respect to Tab. 3.1 set of values are explicitly indicated in the text, otherwise they have been used.

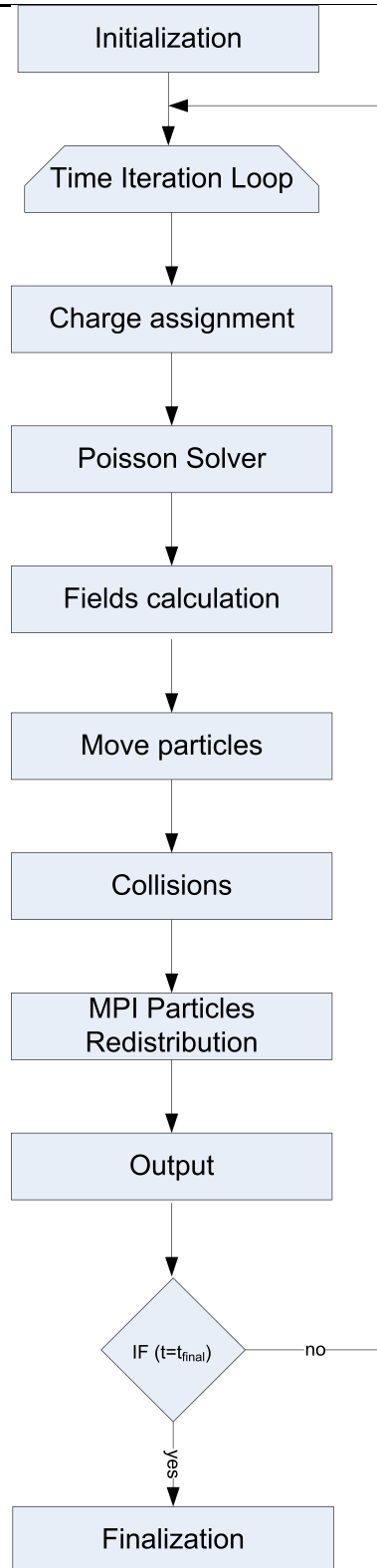


Figure 3.3: Chartflow of the ONIX code

3.3.2 Simulation Units

ONIX code could be adjusted to a variety of physical situations due to flexibility of the input parameters and realistic (not normalized) physical constants. The code simulation

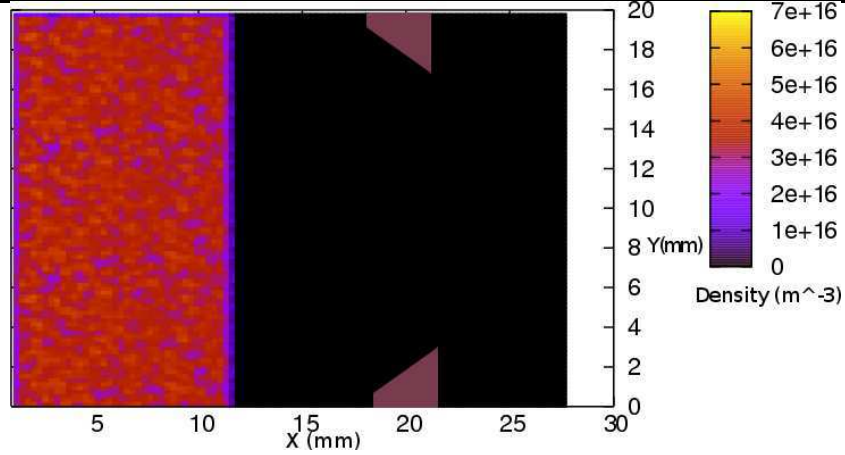


Figure 3.4: The initial positive ion density (H^+) distribution along the simulation domain. The plasma grid is centered at the distance of 20 mm

units are the International System ones and they are summarized in Tab. 3.2.

Table 3.2: Simulation units and physical constants used in the ONIX code

Unit of Length	$[x,y,z]=m$
Unit of Time	$[t]=s$
Unit of Velocity	$[v_x, v_y, v_z]=m/s$
Unit of Temperature	$[T]=K$
Unit of Density	$[\rho]=m^{-3}$
Unit of Charge	$[q]=C$
Unit of Mass	$[m]=kg$
Unit of Potential	$[\phi]=V$
Unit of Energy	$[E]=J$
Unit of Electric Field	$[E_x, E_y, E_z]=V/m$
Unit of Magnetic Field	$[B_x, B_y, B_z]=T$
Boltzmann constant	$[k_b]=1.38 \times 10^{-23} J/K$
Electric constant (Permittivity of Free Space)	$[\epsilon_0]=8.85 \times 10^{-12} A*s/V*m$

3.3.2.1 Length Scale

The smaller length scale in these plasma simulations is the Debye length given by:

$$\lambda_D = \sqrt{\frac{\epsilon_0 k_b T_e}{e^2 n_e}} \quad (3.1)$$

where ϵ_0 is the permittivity of free space, k_b is the Boltzmann constant, T_e is the temperature of electron, e is the electron charge and n_e the electron density. In the standard initial plasma conditions ($T_e = 3$ eV and $n_e = 10^{17} m^{-3}$) λ_D equals about 4×10^{-5} m. Nevertheless, the electron temperature grows fast close to the plasma grid orifice, so the Debye length increases up to 0.3 mm.

In the stable PIC plasma simulation the size of one cell should be smaller than the Debye length. Therefore, huge computer resources are necessary to satisfy the length scale condition in 3 dimensional model of the computation domain shown in Fig. 3.1. Consequently, in order to employ reasonable computation time the uniform simulation mesh of $100 \times 100 \times 100$ cells has been used in our calculation with the distance of $0.00028 \times 0.0002 \times 0.0002$ m between two neighboring points in x , y and z directions, respectively.

3.3.2.2 Time Scale

The estimated length and time scale factors completely satisfy the Courant–Friedrichs–Lewy (CFL) condition [85]:

$$\frac{\mathbf{v}\Delta t}{\Delta \mathbf{x}} \leq 1 \quad (3.2)$$

Taking \mathbf{v} as the maximum velocity that an electron can gain (3.5×10^7 m/s, 6800 V) we set $\Delta t = 3 \times 10^{-12}$ s. Note that this value is much smaller than reverse plasma frequency ω_p^{-1} . It means that electron with maximum possible velocity will not "jump" between PIC nodes, i.e. will be present in one cell at least once for each refresh of the potential map.

In order to prove the validity of the time scale, the simulation with a smaller time step has been performed. In Fig. 3.5 the steady state potential distribution is presented from the calculations using 3×10^{-12} s (red line) and 1.5×10^{-12} s (green line) time step. Both distributions are almost the same, therefore the chosen time scale is applicable for the model. The relative error is $< 2\%$ all along the simulation domain, except the plasma "reservoir" where the statistical fluctuations changing the plasma potential around zero (± 10 V).

3.3.3 Weighting Scheme

If each and every particles will be modeled in our simulation domain (Fig. 3.1) with bulk density of 10^{17} m^{-3} , we will have to track 10 trillion particles. Such enormous number of particles would clearly overcrowd even the best computer's memory capacities. If once assumes that particles could be stored, the amount of required simulation time to compute their trajectories would be unreasonable even when using the best modern computation machines. Therefore, it is important to reduce the number of simulated particles to some reasonable amount.

One of the methods for reducing the number of simulated particles is known as "Super-Particles" or "Macro-Particles". It consists of assigning to a single computational particle a given number of real, physical particles. This technique was used for the first time in [86, 96]. Generally, one macro-particle denotes 10^3 to 10^7 real particles. It has been found that the size of 1 super-particle could be increased up to a certain point without any significant loss of stability. However, when the number of the computation particles per one grid cell becomes too small, the particle statistics gains inaccuracy.

In order to prove the accuracy conservation run tests have been performed increasing the size of macro-particle, with simultaneous decreasing of the particles number per grid cell, two simulations have been performed with different statistical weighting. The first

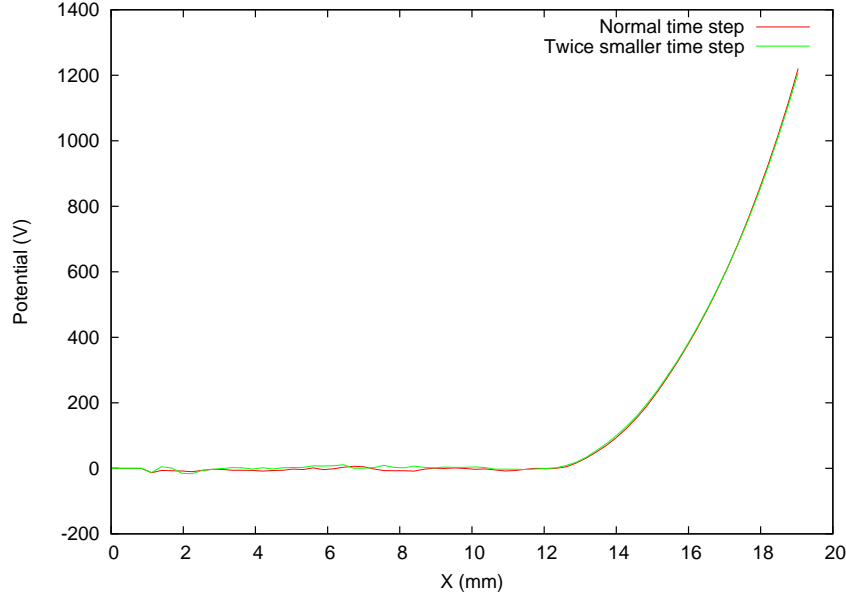


Figure 3.5: The potential distribution along the symmetry axis at $y = 10$ mm $z = 10$ mm plane. Red solid line - simulation with $\Delta t = 3 \times 10^{-12}$ s, green dot line - $\Delta t = 1.5 \times 10^{-12}$ s

one includes 10 super particles in one cell, while the second uses 20 particles per cell for half of the previous weight. The simulation results do not show any significant difference between these two calculations. However, the lower particle's number per cell than 10 could cause the raising of the numerical noise and simulation instabilities. Therefore, 10 particles per cell have been accepted as the standard configuration of the ONIX program and used in most simulations.

3.4 Boundaries Conditions

The boundary condition is one of the major tasks in the numerical physics. On the one hand, it is difficult to define the border's range of the simulation volume. On the other, the applied conditions on the edge of the domain should be carefully chosen according to the physics representing the domain boundary. In this section different types of boundary conditions implemented in the studied model will be outlined.

As it has been mention above, the model includes only one aperture of the plasma grid (Fig. 3.1). Periodic boundary conditions have been applied in y and z directions to simulate a matrix of many the PG orifices (1280 in the real machine). Hence one charged particle which leaves the volume in the vertical z direction from the top, will be injected from the bottom with the same energy distribution. This particle corresponds to particles which come from other aperture placed below. The same technique is implemented in the horizontal y direction.

The choice of boundary conditions in the axial x direction is a more problematic task. The boundary from the left-hand side of the simulation domain should be chosen in such a way, as not to evoke artificial influence on the neutral plasma in this region. Therefore, all charged particles that strike the left border are reflected back towards the plasma

with new thermal velocity. It is assumed, that if a particle leaves the region close to the plasma grid, another particle of the same kind will come there from the expansion chamber. Therefore, the neutrality of the system is saved.

The Poisson solver uses the Dirichlet boundary condition applied to the left edge of the simulation domain in the standard version of the code. The potential in this plane has been set to the constant analytical or experimental potential value varying between $0 < \phi < 50$ V. However, several runs have been also performed with the Neumann boundary condition, where the electric field value at the boundary points has been fixed at 0: $\frac{\partial \phi}{\partial \mathbf{x}} = 0$. More details about boundary conditions involved in the Poisson solver are presented in Sec. 3.8.3.

The plasma grid is represented as a perfect conductor. All positive and negative ions impacting the wall are totally absorbed or neutralized. Nevertheless, the electrons that strike PG could produce secondary electrons. The coefficient of the secondary electron emission by electron impact has been determined *a posteriori*, based on the energy distribution of electrons hitting the wall. This energy distribution has been obtained from the first ONIX simulations. About 90% of electrons have enough energy (> 50 eV) to produce new ones. Consequently, the emission probability for electrons has been chosen as 0.9. The electrons are emitted from the wall with new thermal energy of 3 eV.

A constant potential of 6.8 kV is applied to the right side boundary of the simulation domain in the axial (x) direction. The positive ions and electrons crossing this boundary are reinjected at a random position inside the volume filled by the initial plasma. The negative ions passing through the right boundary of the simulation domain are eliminated from the system and are encountered as the NI extracted current.

3.5 Initial Velocity Distribution

Basically, particles are injected in the simulation domain with the Maxwellian velocities distribution in all directions (v_x, v_y, v_z). The probability of finding a velocity is given by [86]:

$$p(\mathbf{v}) = (\sqrt{(2\pi)}v_{th})^{-1} \exp\left(\frac{-\mathbf{v}^2}{2v_{th}^2}\right) \quad (3.3)$$

where $v_{th} = \sqrt{\frac{k_b T}{m}}$ is the particle thermal velocity. The general method of setting up this distribution is expressed as:

$$c(\mathbf{v}) = \frac{1}{2} \operatorname{erf}\left(\frac{\mathbf{v}}{(2v_{th}^2)^{\frac{1}{2}}}\right) \quad (3.4)$$

where $c(\mathbf{v})$ is a random number in the range $-\frac{1}{2} \leq c(\mathbf{v}) \leq \frac{1}{2}$ and *erf* is the error function defined by:

$$\operatorname{erf}(x) = \frac{2}{\sqrt{\pi}} \int_0^x e^{-x^2} dx \quad (3.5)$$

$c(\mathbf{v}) = (r - \frac{1}{2})$ was set, where r is a random number in the normal range $0 \leq r \leq 1$. Then, solving the equation (3.4) for the required velocity \mathbf{v} :

$$\mathbf{v} = \sqrt{2}v_{th}erf^{-1}(2r - 1) \quad (3.6)$$

Therefore, this method requires the inverse error function erf^{-1} subroutine, or precalculated table of this function. Thus, such subroutine has been developed and integrated in the code. The typical result of the initial electron velocity distribution in x direction is shown in Fig. 3.6, with $v_{th} = 3$ eV.

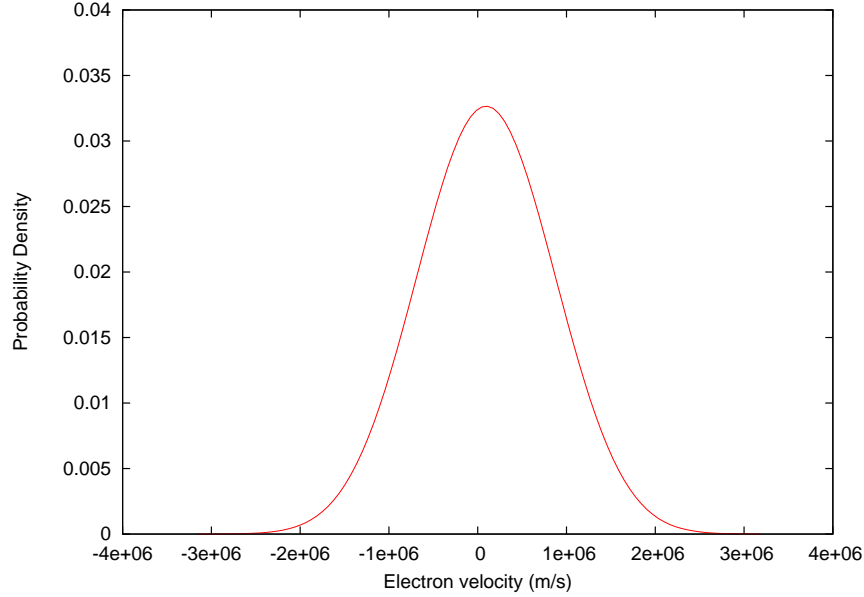


Figure 3.6: The Probability Density Function (PDF) of the initial electron velocity distribution

3.6 Different Types of Plasma Formation

The plasma is neutral inside the expansion chamber of the NBI negative ion source system. The negative charge prevails only close to the plasma grid (1 – 5 mm from PG), where positive ions meniscus is placed. Therefore, it is important to keep neutral plasma in the simulation region corresponding to the expansion chamber. Three methods of plasma formation inside the simulation volume have been implemented and tested in the ONIX program (Fig. 3.7).

The first numerical technique has been partially discussed in Sec. 3.4. The initial neutral plasma ($n_e = n_{H^+} + n_{H_2^+}$) covers the area from 0 to 12 mm of the simulation domain (Fig. 3.7 (left)). If the simulated particle leaves the computation domain (extracted or absorbed in the PG wall) another particle of the same kind will be injected with thermal energy in the region of the initial plasma at random position. The particle, which strikes the left side boundary of the simulation domain, is reflected back in the volume with new initial velocity. It means that if one particle transfers from the extraction region to the expansion chamber, another particle (in the expansion chamber) will come to the extractor. Thus, the plasma is retained neutral in the region of the computation domain that corresponds to the expansion chamber.

The second technique to generate a plasma is the injection of given particle flux from one plane ($y - z$ cross section) of the simulation volume. This method takes place in other 2D code for negative ion extraction [75]. Usually, this plane is located at the left boundary of the domain, or close to it (Fig. 3.7 (center)). The simulated particles are injected at each iteration step with the flux that builds up the necessary plasma density. The full open boundary conditions are considered at the right and left sides of the simulated domain, namely if a particle collides with these boundaries it will be eliminated from the system. Different initial velocity distributions and plane positions have been tested. However, the neutral plasma in the injected plane region has never appeared. The injected particles create excessive electric field there, which artificially accelerates particles towards the extractor. In order to prove the ability of this method to form steady state neutral plasma, one-dimensional transport collisionless code has been developed. In this model particles move only according to their constant initial velocities (electric and magnetic fields are not considered). Even in such humble model the steady state neutral plasma is created only after $400 \mu s$. It proves the quasi-impossibility of using this method in the ONIX code due to intolerably long computation time (2 days of ONIX performance on 20 CPU gives only $1 \mu s$ of simulation time).

The last numerical technique of plasma creation involves a construction of one or a few neutral planes with constant plasma density (Fig. 3.7 (right)). In this method, a given amount of simulated particles is held in each cell of the neutral plane in order to form the necessary density. For instance, if one electron leaves a cell from this plane, another electron will be injected there; and vice versa, if one extra electron comes from the simulation domain to the neutral plane, another one will be eliminated from the system. However, the current method suffers from the same artificial field formation as the previous one, in the transition region from the neutral plane to the ordinary volume cells.

Therefore, taking into account all instability and artifacts of the particles flux and neutral plane methods, the particles reinjection technique has been chosen as the most accurate for such plasma system. Consequently, most of the simulations have been performed using the first particles reinjection technique.

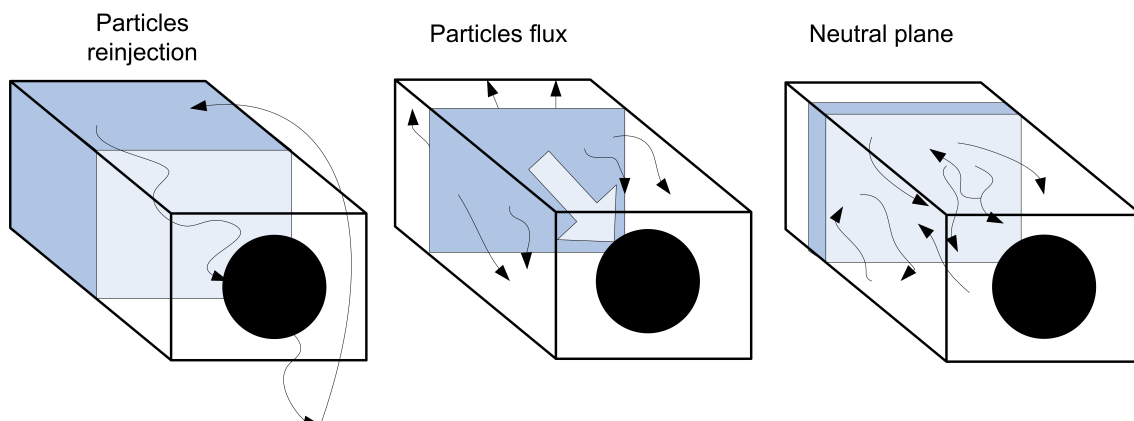


Figure 3.7: Three numerical technique to generate the plasma tested in the ONIX code. The particles re-injection procedure is shown in the left. The particles flux injection is shown in the middle. The particle injection from the neutral plane - in the right

3.7 Particle-in-Cell Method in the ONIX Code

The Particle-In-Cell (PIC) method is used to approach a solution of Vlasov equation (Eq. 3.7). This equation describes the self-consistent acceleration of the electron and ions (time evolution of the distribution function f) in a plasma with long-range interaction. It operates by applying the charge of all particles used in the simulation onto an artificial mesh.

$$\frac{df}{dt} = \frac{\partial f}{\partial t} + \mathbf{v} \cdot \frac{\partial f}{\partial \mathbf{x}} + \frac{\mathbf{F}}{m} \cdot \frac{\partial f}{\partial \mathbf{v}} = 0 \quad (3.7)$$

where $f(\mathbf{x}, \mathbf{v}, t)$ is the particle distribution function, \mathbf{F} is the force acting on the particles, and m is the particle mass. The field distribution is then resolved according to the mesh points. This method was described by Hockney (1988) [86] and Birdsall (1991) [87], and has been widely used in various areas of numeric physical research. The decided advantage of the PIC method is the possibility to follow each charged particle trajectory in self-consistent electromagnetic or electrostatic fields capturing thus the microscoping information on the plasma. For different types of problems the PIC algorithm is nearly the same, and is straightforward to develop. It includes five main steps:

1. Assigning charge of the particles to the mesh.
2. Solving Poisson's equation on the mesh points.
3. Computing forces from the mesh-calculated potential (electric field).
4. Interpolating forces to the particles location.
5. Moving particles (calculating new particle velocities and position according to the computed force).

The first step requires the charge dispatched on the PIC mesh points. There are several schemes of this procedure [86]. The most popular are the Nearest Grid Point (NGP) and the Cloud-In-Cell (CIC) algorithms. NGP is the zero order approximation involving the absolute charge assignment to the nearest node. The second method (first order) deals with eight neighboring nodes in 3D case. A particle charge is divided among eight nearest points relative to the distance to each of them.

The Cloud-In-Cell method requires the use of the interpolation algorithms to project the charge of the particles onto the mesh. There are many interpolation methods; the idea is to exploit the one, which gives sufficiently high accuracy and contributes tolerable to the increase of the simulation time. Our three-dimensional model, where 7000000 – 40000000 real particles (depending on the run) are used, suffers from the real computation time. Therefore, the CIC charge assignment method with the humble first-order linear interpolation algorithm has been developed in the ONIX code. For the sake of clarity this scheme is presented in Fig. 3.8 for the 2 dimensions case. The charge has been distributed onto the mesh points by using Eq. 3.8:

$$\rho(i, j) = q \times (1 - dx) \times (1 - dy) \times weight \quad (3.8a)$$

$$\rho(i + 1, j) = q \times (dx) \times (1 - dy) \times weight \quad (3.8b)$$

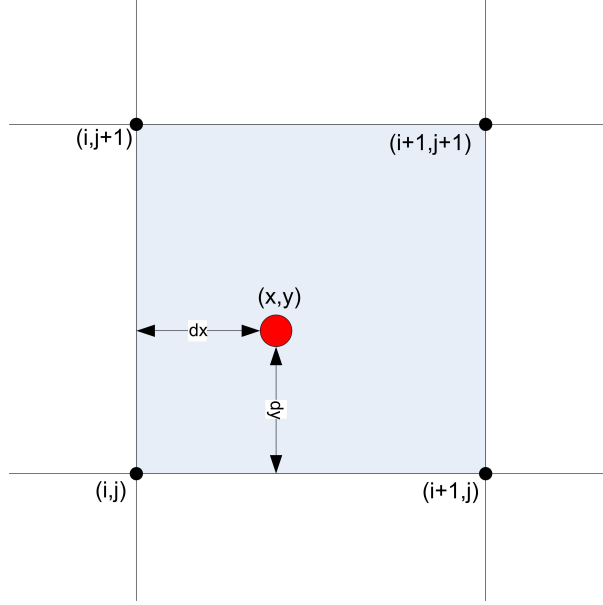


Figure 3.8: Example of linear 2D charge assignment on the mesh points with computational particle located at (x, y) . Eq. 3.8 is used to distribute the charge onto the grid nodes

$$\rho(i, j + 1) = q \times (1 - dx) \times (dy) \times \text{weight} \quad (3.8c)$$

$$\rho(i + 1, j + 1) = q \times (dx) \times (dy) \times \text{weight} \quad (3.8d)$$

where q is the charge of different species that is projected onto PIC nodes, dx and dy distance to the left and bottom boundaries of the cell, respectively, and "weight" describes the number of real particles (see Sec. 3.3.3).

3.8 Poisson Solver

The calculation of the potential distribution inside the simulation domain is one of the cardinal tasks in an electrostatic PIC code. The potential is determined by the solution of the Poisson equation:

$$\nabla^2 \phi = -\frac{\rho}{\epsilon_0} \quad (3.9)$$

where $\epsilon_0 = 8.85 \times 10^{-12}$ F/m (C^2/Nm^2) is the permittivity of free space, ϕ is the electrostatic potential (volts), and ρ is the charge density (C/m^3).

3.8.1 Discretization

In 3D Cartesian coordinate the Poisson equation is expressed as a second order partial differential equation:

$$\frac{\partial^2 \phi}{\partial x^2} + \frac{\partial^2 \phi}{\partial y^2} + \frac{\partial^2 \phi}{\partial z^2} = -\frac{\rho}{\epsilon_0} \quad (3.10)$$

The finite difference method is used in order to get solution of Eq. 3.10. Thus, the first derivative is given as:

$$\frac{\partial \phi}{\partial x} \approx \frac{\phi_{(i+1,j,k)} - \phi_{(i,j,k)}}{\Delta x} \quad (3.11a)$$

$$\frac{\partial \phi}{\partial y} \approx \frac{\phi_{(i,j+1,k)} - \phi_{(i,j,k)}}{\Delta y} \quad (3.11b)$$

$$\frac{\partial \phi}{\partial z} \approx \frac{\phi_{(i,j,k+1)} - \phi_{(i,j,k)}}{\Delta z} \quad (3.11c)$$

where $\phi_{i,j,k}$ is the potential value at the mesh point with coordinate (i, j, k) , and $\Delta x, \Delta y, \Delta z$ are distances between two neighboring nodes in x, y and z directions, respectively. The second derivative is then shown as:

$$\frac{\partial^2 \phi}{\partial x^2} \approx \frac{\phi_{(i+1,j,k)} - 2\phi_{(i,j,k)} + \phi_{(i-1,j,k)}}{\Delta x^2} \quad (3.12a)$$

$$\frac{\partial^2 \phi}{\partial y^2} \approx \frac{\phi_{(i,j+1,k)} - 2\phi_{(i,j,k)} + \phi_{(i,j-1,k)}}{\Delta y^2} \quad (3.12b)$$

$$\frac{\partial^2 \phi}{\partial z^2} \approx \frac{\phi_{(i,j,k+1)} - 2\phi_{(i,j,k)} + \phi_{(i,j,k-1)}}{\Delta z^2} \quad (3.12c)$$

Therefore, using Eq. 3.12, the Poisson equation can be rewritten as follows:

$$\frac{\phi_{(i+1,j,k)} - 2\phi_{(i,j,k)} + \phi_{(i-1,j,k)}}{\Delta x^2} + \frac{\phi_{(i,j+1,k)} - 2\phi_{(i,j,k)} + \phi_{(i,j-1,k)}}{\Delta y^2} + \frac{\phi_{(i,j,k+1)} - 2\phi_{(i,j,k)} + \phi_{(i,j,k-1)}}{\Delta z^2} = -\frac{\rho}{\epsilon_0} \quad (3.13)$$

Finally, the obtained Eq. 3.13 could be easily applied for computer simulations due to the absence of the complex mathematic functions.

3.8.2 Conjugate Gradient Method

There are a number of algorithms for the solution of the second order differential equation (Eq. 3.12). They are restricted to the structure of the equation matrix and require different computation time. If we have to amnange large and sparse matrix, then iterative methods are often to be preferred over the direct methods, because the former help to reduce both the required memory and computing time. The Conjugate Gradient (CG) is one of the successful iterative methods that provides high accuracy using the tolerable simulation time. This algorithm was first introduced in 1952 by M. R. Hestenes and E. Stiefel [88]. The Conjugate Gradient method is an algorithm for finding the nearest local minimum of the function that is also a solution of the system of linear equations. CG is effective for the following system:

$$A\mathbf{x} = \mathbf{b} \quad (3.14)$$

where \mathbf{x} is an unknown vector, \mathbf{b} is a given vector and A is the Symmetric Positive Defined (SPD) matrix:

$$\begin{cases} A^T = A \\ x^T Ax > 0, x \neq 0 \end{cases} \quad (3.15)$$

If A is SPD, then solving Eq. (3.14) is equivalent to the problem of minimizing the quadratic form [89]:

$$f(x) = \frac{1}{2}x^T Ax - b^T x \quad (3.16)$$

One can minimize $f(x)$ by setting $f'(x)$ equal to zero:

$$f'(x) = \frac{1}{2}A^T x + \frac{1}{2}Ax - b \quad (3.17)$$

If A is symmetric, Eq. 3.17 is reduced to the following form:

$$f'(x) = Ax - b \quad (3.18)$$

By setting the gradient to zero, Eq. 3.14 is obtained, which is the linear system that needs to be solved. Therefore, the solution of $Ax = b$ is a minimum of $f(x)$, so Eq. 3.14 can be solved by finding x that minimizes $f(x)$.

In order to find such minimum, we start from the arbitrary value of x_0 (generally $x_0 = 0$) and move down along the function to the minimum value. The series of steps x_1, x_2, \dots, x_n are taken until the solution x is reached. At each step the direction d is chosen, in which $f(x)$ decreases faster. This direction is opposite to $f'(x_i)$:

$$-f'(x_i) = b - Ax_i = d_i \quad (3.19)$$

At the first step ($i = 0$) $d_i = r_i$, where r_i is the residual and shows how far we are from the correct value of b . At each next iteration step point x is chosen as:

$$x_{i+1} = x_i + \alpha d_i \quad (3.20)$$

with α derived in [90] as:

$$\alpha_i = \frac{r_i^T r_i}{d_i^T A d_i} \quad (3.21)$$

The Conjugate Gradient method could be applied for finding the solution of the Poisson equation (3.9), because it is the SPD linear system of the partial differential equations, as in (3.14). The chartflow of the CG algorithm leveraged in the ONIX program is shown in Fig. 3.9.

The convergence rate of the CG method is estimated by the eigenvalues of the equations matrix [91]. In order to accelerate the convergence of matrix A (Eq. 3.14), the precondition technique is frequently used [84]. Suppose that M is the SPD matrix approximating A , meanwhile matrix M is easier to invert. Therefore, we can solve Eq. 3.14 indirectly resolving the following system:

$$M^{-1}Ax = M^{-1}b \quad (3.22)$$

The matrix M can be chosen in such a way that eigenvalues of $M^{-1}A$ are clustered better than those of A . Finally, we can solve Eq. 3.22 much faster than the original

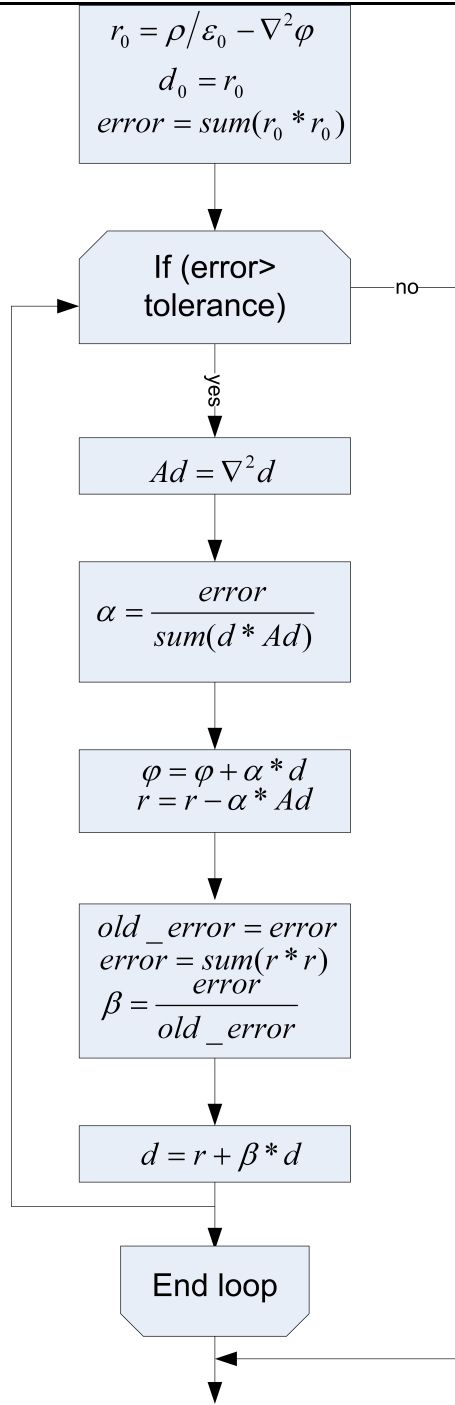


Figure 3.9: Chartflow of the CG method implemented in the ONIX program (Poisson Solver part of Fig. 3.3), where r , ϕ , d , Ad are matrices of equal size $(0 : i, 0 : j, 0 : k)$. The tolerance corresponds to the required accuracy

problem (Eq. 3.14). This acceleration technique has been also implemented in the ONIX code.

Several runs have been performed for estimating the advantage of the precondition method over the humble Conjugate Gradient algorithm. In Tab. 3.3 the required calcu-

lation time necessary for finding the solution of the Poisson equation is collected using both methods. One can see that the PCG method is about three times faster than CG in all precisions.

Table 3.3: The comparison of time performance for solving the Poisson equation using the Conjugate Gradient and the Precondition Conjugate Gradient methods

Precision	PCG (~iteration)	CG (~iteration)	PCG time (s)	CG time (s)
$1E$	104	601	0.25	1.12
$1E^{-1}$	188	637	0.39	1.141
$1E^{-2}$	211	750	0.56	1.7
$1E^{-3}$	235	818	0.6	1.82
$1E^{-4}$	268	870	0.65	1.89
$1E^{-5}$	295	915	0.67	2.1
$1E^{-10}$	397	1130	0.88	2.6

3.8.3 Potential Boundaries Correction

The negative ions created at the Plasma Grid wall organize negative sheath in vicinity to the orifice that plays decisive role in the NI extraction, and has significant influence on the co-extracted electron current (see Sec. 5.4). Therefore, it is important to obtain the realistic potential at the points close to the PG boundaries. The ordinary Poisson solver is not able to calculate the true potential value at boundaries lying between the mesh nodes in the PIC simulations. In order to calculate the potential on the grid points, the potential value of two neighboring nodes has to be used in each direction (Eq. 3.12). There are often points in the simulation domain with irregular boundaries, which have only one neighbor inside the domain. The second neighboring point is usually located outside the border. Fig. 3.10 shows an example of such irregular region [92]. The solid line is the real boundary, and the open circle marks the nearest points of the mesh. For instance, we need to calculate the potential at point $x = 0.6$. According to Eq. 3.12 the potential values at points $x = 0.5$ and $x = 0.7$ are required. However, point $x = 0.7$ is out of the computation domain, thus its utilization will lead to the gridded (stepped) structure of the resulting potential distribution at the boundaries. We can avoid such situation by introduction of new points at the domain border line, and by using the distance from last node ($x_{i,j}$) to the border (x_b) [93]: $\Delta x' = x_b - x_{i,j}$ (Fig. 3.10).

Therefore, when applying this technique to the Poisson solver, the second derivative approximation must be modified to account for the boundaries correction. Eq. 3.12 is then rewritten as [93]:

$$\frac{\partial^2 \phi}{\partial x^2} \approx \frac{1}{\Delta x^2} (\phi_{i+1,j,k} + \phi_{i-1,j,k} - \phi_{i,j,k} (1 + \frac{1}{\alpha x_{i,j,k}})) \quad (3.23a)$$

$$\frac{\partial^2 \phi}{\partial y^2} \approx \frac{1}{\Delta y^2} (\phi_{i,j+1,k} + \phi_{i,j-1,k} - \phi_{i,j,k} (1 + \frac{1}{\alpha y_{i,j,k}})) \quad (3.23b)$$

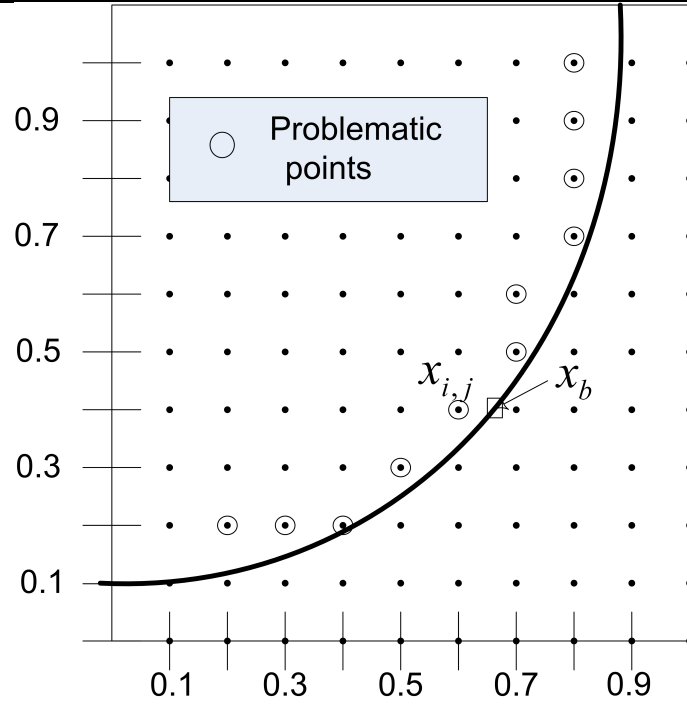


Figure 3.10: The irregular region of simulation domain. The solid line is the real boundary; the open circle indicates the problematic points

$$\frac{\partial^2 \phi}{\partial z^2} \approx \frac{1}{\Delta z^2} (\phi_{i,j,k+1} + \phi_{i,j,k-1} - \phi_{i,j,k} (1 + \frac{1}{\alpha z_{i,j,k}})) \quad (3.23c)$$

where:

$$\alpha x, \alpha y, \alpha z = \begin{cases} 1, \text{ at "correct" points} \\ \frac{x_b - x}{\Delta x}; \frac{y_b - y}{\Delta y}; \frac{z_b - z}{\Delta z} & \text{at problematic points} \end{cases} \quad (3.24)$$

αx , αy and $\alpha z = 1$ are at all "correct" nodes and take value between 0 and 1 at the problematic points. For example, at point $x = 0.5$ (Fig. 3.10) $\alpha x = (x_b - x)/\Delta x = (0.65 - 0.6)/0.1 = 0.5$. If αx , αy , $\alpha z = 1$, Eq. 3.23 will assume the form of general Eq. 3.12.

The improvement achieved using this method can be seen in Fig. 3.11, that shows the potential inside a grounded cylinder created by an arbitrary charge distribution. Without boundary correction (Fig. 3.11.a), the gridded structure is clearly visible on the potential field map. The electric field calculated from this potential is non purely radial, but it presents a large poloidal component in certain points close to the border. This numerical artifact is almost suppressed when using the boundary correction (Fig. 3.11.b) with the same grid. The potential is smoother, and the electric field obtained is almost radial everywhere.

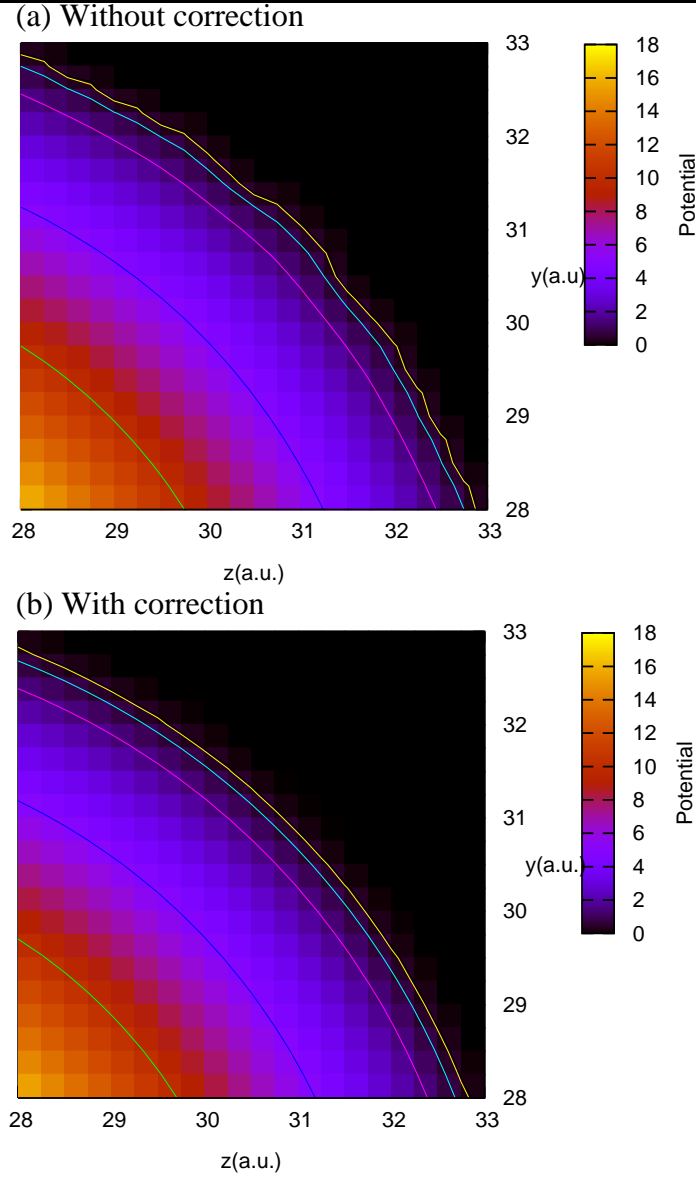


Figure 3.11: Potential created by a given charge distribution inside a grounded cylinder calculated without the boundary correction in the Poisson solver (a) and with the correction (b) Eq. 3.23. In the case without boundary correction (a) the gridded structure is presented at the edges (yellow and blue isolines). This artifact is suppressed when potential boundary correction technique is applied (b)

3.8.4 Potential Boundaries Conditions

It should be remembered, that the simulation model includes only one orifice of the plasma grid with periodic boundary conditions in y and z directions (Fig. 3.1). Such configuration represents an infinite array of the plasma grid apertures. Due to the periodicity, the potential must fulfill a Neumann boundary condition ($\frac{\partial\phi}{\partial y} = 0$, $\frac{\partial\phi}{\partial z} = 0$). Therefore, the electric field in this region vanishes.

The right hand side boundary of the simulation volume uses the Dirichlet condition. The potential at the boundary points is fixed to the constant value (from 4 to 20 kV in different calculations), that represents the local isopotential plane between the plasma and the extraction grid. The left hand side boundary uses both Neumann and Dirichlet conditions depending on the simulation.

In real experiments PG is positively biased against the plasma (10 – 20 V) [50, 51] to reduce the co-extracted electron current. However, for the geometry used here (an infinite array of apertures) the effect of the bias should be less important. This is because in the vicinity of any point of the PG surface the screened extraction field takes significant values in the simulation, while in the experimental device the total aperture area is smaller than full plate electrode (PG). The calculations made with a bias potential of 100 V do not show significant differences with respect to the unbiased case. Consequently, in most of simulations presented here, the bias potential is taken at 0 V (plasma grid is grounded).

3.9 Electric and Magnetic Fields Calculation

The forces in plasma depend not only on the externally applied fields and boundaries conditions, but also on the plasma structure itself. Maxwell's equations control these forces and can be found in any general plasma physics textbook, for instance in [97]. Two major types of the plasma simulation are commonly used in the numeral physics: electromagnetic and electrostatic. The first one assumes that externally produced electromagnetic fields (laser, microwaves, etc.) induced in the plasma are present. This approach requires calculation and interpolation of the full set of Maxwell's equations at every time step, and its computation is usually costly.

The electrostatic approach, which is used in the present ONIX program, assumes that external magnetic field remains constant throughout, and is static in time. This permits to reduce complete set of Maxwell's equations to only one Poisson equation (Eq. 3.9). The electric field is then calculated at each node by taking the gradient of the potential:

$$\mathbf{E} = -\nabla\phi \quad (3.25)$$

The central-differences scheme gives the following expression:

$$E_x = \frac{\phi_{i+1,j,k} - \phi_{i,j,k}}{\Delta x} \quad (3.26a)$$

$$E_y = \frac{\phi_{i,j+1,k} - \phi_{i,j,k}}{\Delta y} \quad (3.26b)$$

$$E_z = \frac{\phi_{i,j,k+1} - \phi_{i,j,k}}{\Delta z} \quad (3.26c)$$

where E_x , E_y , E_z are calculated electric fields at the middle of the PIC nodes in x , y , and z directions, respectively. The linear interpolation algorithm (see Sec. 3.7) is then used to project the electric field onto the particles coordinates for each cell.

Let us remember that external complex magnetic field geometry is applied in the NBI plasma source system in order to decrease fraction of the undesirable co-extracted electron beam. The distributions of both filter and deflecting magnetic fields were taken

from the experimental data [50]. The filter magnetic field is in z direction, with the gradient along x , and given by:

$$B_{z,y}(x) = B_{max} \exp\left(-\frac{(x - x_{max})^2}{2\sigma^2}\right) \quad (3.27)$$

with $B_{max} = 7$ mT, $\sigma = 35$ mm, $x_{max} = 0$ mm. The deflecting magnetic field is oriented in the horizontal y direction, but its gradient is also along x . Its profile is given by Eq. 3.27 with different parameters than B_z , namely $B_{max} = 80$ mT, $\sigma = 6$ mm and $x_{max} = 30$ mm Fig. 3.12 [94].

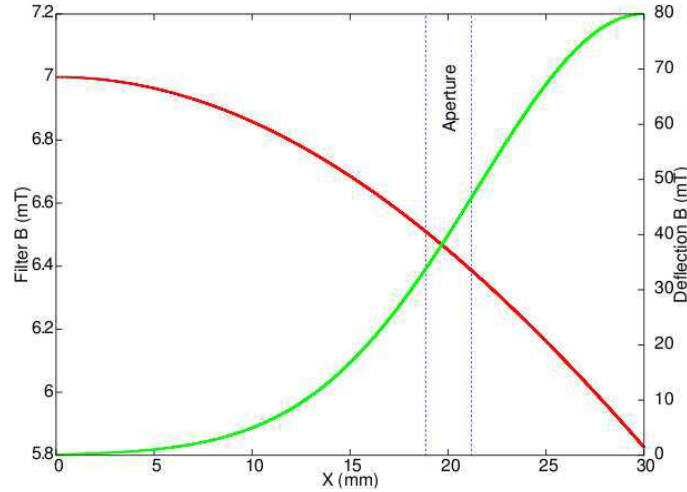


Figure 3.12: Distribution of magnetic field along the simulation domain. Red line represents the magnetic filter field in the vertical z direction, green line – deflecting magnetic field in the horizontal y direction. Plasma grid is located between $x = 19$ mm and $x = 21$ mm (blue line)

3.10 Particle Movement

One of the most important parts of the PIC plasma simulation process is the particles pusher. Even if the weighting macro-particle scheme is used (see Sec. 3.3.3), the total number of simulated particles is $> 10^6$. Commonly, particle motion is the most time consuming part of the PIC model, because it has to be done each time step for each particle independently. The particle movement is a procedure of the particle advancing to a new position in response to the forces acting on them.

The particle motion governing equations are simply the definition of velocity:

$$\frac{d\mathbf{x}}{dt} = \mathbf{v} \quad (3.28)$$

and acceleration:

$$\frac{d\mathbf{v}}{dt} = \frac{q}{m}(\mathbf{E} + \mathbf{v} \times \mathbf{B}) \quad (3.29)$$

The Eq. 3.29 is the Newton's Second Law, with the force being the Lorentz Force. The aim is to integrate this equation in time. There are two numerical schemes usually used for particles movement: implicit and explicit solvers. In the former the particle velocity is calculated from already updated fields, while in the latter only old forces from the previous step are used. The explicit scheme is commonly faster and simpler, but it requires a smaller integration time step.

In the ONIX code the explicit solver is used according to the mesh size, which is usually faster for the simulation with large equation matrix. The typical scheme for discretization of Eq. 3.28, 3.29 is the leapfrog finite-differential algorithm [86]. It is called so because time, at which velocity components and positions are known, are delayed from each other by half a time step. First, velocity is calculated through the time, after the position is updated using the velocity vector (Fig. 3.13). In this method, the particles position and field values are defined at integral time levels ($t = 0, \Delta t, 2\Delta t, 3\Delta t, \dots$), while particles velocities are defined at half-integral time levels ($t = \frac{1}{2}\Delta t, \frac{3}{2}\Delta t, \frac{5}{2}\Delta t, \dots$). The leapfrog finite-differential approximation to Eq. 3.28, 3.29 takes the following form:

$$\mathbf{x}_{n+1} - \mathbf{x}_n = \mathbf{v}_{n+1/2}\Delta t \quad (3.30)$$

$$\mathbf{v}_{n+1/2} - \mathbf{v}_{n-1/2} = \Delta t \frac{q}{m} \left(\mathbf{E} + \frac{\mathbf{v}_{n+1/2} + \mathbf{v}_{n-1/2}}{2} \times \mathbf{B} \right) \quad (3.31)$$

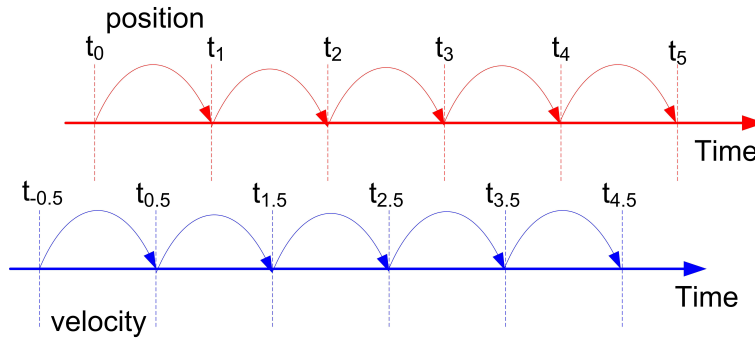


Figure 3.13: The schematic view of the leapfrog method. Particle position is evaluated at integral time step, while the velocity is calculated at half time step

The current version of the simulated code uses the Boris leapfrog algorithm to push charged particles [86, 87, 95]. In this method the electric acceleration terms and the magnetic rotation terms of Eq. 3.31 can be separated by the introduction of two intermediate velocities v^- and v^+ :

$$\mathbf{v}^- = \mathbf{v}_{n-1/2} + \frac{q\mathbf{E}}{m} \frac{\Delta t}{2} \quad (3.32)$$

$$\mathbf{v}^+ = \mathbf{v}_{n+1/2} - \frac{q\mathbf{E}}{m} \frac{\Delta t}{2} \quad (3.33)$$

If we substitute these definitions into the original equation (3.31), we obtain pure rotation:

$$\frac{\mathbf{v}^+ - \mathbf{v}^-}{\Delta t} = \frac{q}{2m}(\mathbf{v}^+ + \mathbf{v}^-) \times \mathbf{B} \quad (3.34)$$

The chartflow diagram of the particle motion subroutine implemented in the ONIX code is shown in Fig.3.14. The validation of the developed subroutine is given in Sec. 3.13.1, where the numerical check-up of all program parts is presented.

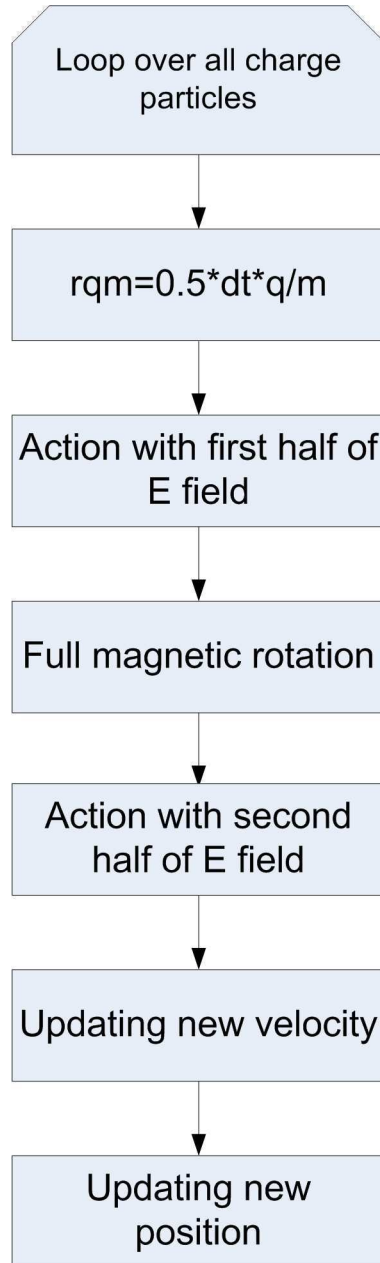


Figure 3.14: Chartflow diagram of the particles motion subroutine using Boris leapfrog methodology (Move Particles part of the general chartflow Fig. 3.3)

3.11 Model for Collision Events

The Vlasov equation (Eq. 3.7) includes a collision term on the right-hand side. This expression is responsible for all collisions between particles in a modeling system, during which they can exchange energy and momentum, produce new species, be eliminated from the domain, etc. The collision calculation between all possible particle pairs of a large volume would be too expensive computationally, even if the "Macro-Particle" acceleration weighting scheme is applied. Therefore, several Monte Carlo (MC) methods have been developed in order to obtain a solution for the particle collision term during relatively short computation time.

Monte Carlo Collision (MCC) method has been used in plasma modeling for the first time in [98]. At present, there are many modified MCC algorithms such as Null Collision Method (NCM) [78], Binary Collision Model (BCM) [99], etc. However, they all mainly use two techniques for collision events. The first one works with a variable time step between collisions, while the second uses a fixed time step [100].

In ONIX code, as well as in many others standard PIC programs, the second method is used. This technique can be easily implemented in PIC codes, because the required fixed time step is already used there to resolve the Lorentz force equation. In this method the probability P of a particle to fulfill a collision during the fixed time dt is estimated. A random number *rand* is then chosen in order to assess if a collision occurs or not in dt . The main drawback of such methodology is that particle could not have multiple collisions during one time step.

In this section the probability theory used in the ONIX code for the particle collision events will be outlined. The collisions between charged particles included in the program, as well as particle collisions with the neutral background gases, will be presented. Plasma-wall interaction procedure, in particular the production of the negative ions from the Cesium covered PG surface, will be explained.

3.11.1 Basic Probability Calculation for Particle Collision Events

In general, the likelihood of realizing a single collision using the Monte Carlo technique is given by the following relation [101]:

$$P = n_{target} * v_{incident} * \sigma * dt \quad (3.35)$$

where n_{target} – is the density of the target particle, $v_{incident}$ – is the velocity of the incident particle, σ – is cross section of the process and dt – is the time step. An uniformly distributed random number is then used in the interval $0 \leq rand \leq 1$ in order to compare it with calculated collision probability P . If the random number is smaller than P , then collision occurs. Eq. 3.35 requires a subroutine or precalculated table of each cross section of reactions, which are included in the code. A full set of the cross-section (σ) data was downloaded from the Internet database ALADDIN [102] in order to calculate P (Eq. 3.35), they depend only of the particle's incident kinetic energy $\sigma = f(E_{kin})$. The auxiliary subroutine has been developed in ONIX to correlate calculated particle energy with the cross-section data. Consequently, the true reaction cross-section value for a relevant energy is obtained.

The target density (n_{target}) in Eq. 3.35 is represented as integral of all target particles in one PIC cell forming a cloud. Thereby, the collision occurs between each incident single particle and the cloud of the target.

The chartflow diagram of the whole cycle of one collision process is presented in Fig. 3.15. During the first step the kinetic energy and mean velocity of the incident particle are calculated. Most of reactions have an energy region (threshold), where the process is not executable. Then follows the energy check statement. The next step involves an estimation of the reaction cross section by using the precalculated table and correlation function. The likelihood of collision realization is further calculated. In the end, a random number is generated. If it is smaller than the collision probability, the reaction occurs and the procedure is finalized.

3.11.2 Volume Collisions

The volume production of the negative ions results from the collision of low energy electrons (about few eV - Fig. 3.17) with the vibrationally excited molecules (Reac. 1, Table 3.4) [53]. For vibrational levels of H_2 with $v < 5$, the cross section of the reaction is negligible, thus a chance to release collision is taken 0. When the vibration level goes beyond 5 the cross section increases by five orders of magnitude [54]. The code does not calculate the population of the vibrational states. We assume total effective density of vibrational excited $H_2(v)$ (with $5 \leq v \leq 9$) taken from calculations reported in [75]. The energy of created negative ions is given as:

$$E_{H^-} = \frac{1}{2}(E_e - 3.994 + E_{H_2(v)}) \quad (3.36)$$

where E_e is the incident electron energy, value 3.994 comes from the difference between the nuclei potential energy at equilibrium internuclear separation ($E_p = 4.748$) and the electron affinity ($E_A = 0.754$ eV) [75], and $E_{H_2(v)}$ is the internal energy of the hydrogen molecules in the vibration level v .

Three volume processes are mainly responsible for the destruction of the negative ions [53]: mutual neutralization in collision with H^+ ions (Tab. 3.4 Reac.5), associative and non-associative detachment (Tab. 3.4 Reac.2 and Reac.3 respectively) in collision with H atoms, and electron stripping collision (Tab. 3.4 Reac.4). The cross-sections of the negative ion destructive processes are shown in Fig. 3.17. The destruction of NI by the electron stripping collision (pink line, Fig. 3.17) can be minimized by reducing the electron temperature to 1 – 2 eV. Hence in this case, the mutual neutralization (blue line, Fig. 3.17) becomes the dominant loss process. The associative (red line, Fig. 3.17) and nonassociative (green line, Fig. 3.17) detachment reactions are independent of the particles energy and they are always effective due to the absence of threshold. Their destruction rates could be reduced only by decreasing H density.

3.11.3 Plasma Wall Interaction Collisions

The production of the negative ion in the volume is limited due to the low density of the $H_2(v)$ in high vibrational states (because of the low pressure requirement close to the extractor ~ 0.3 Pa). Moreover, electron stripping and mutual neutralization collision

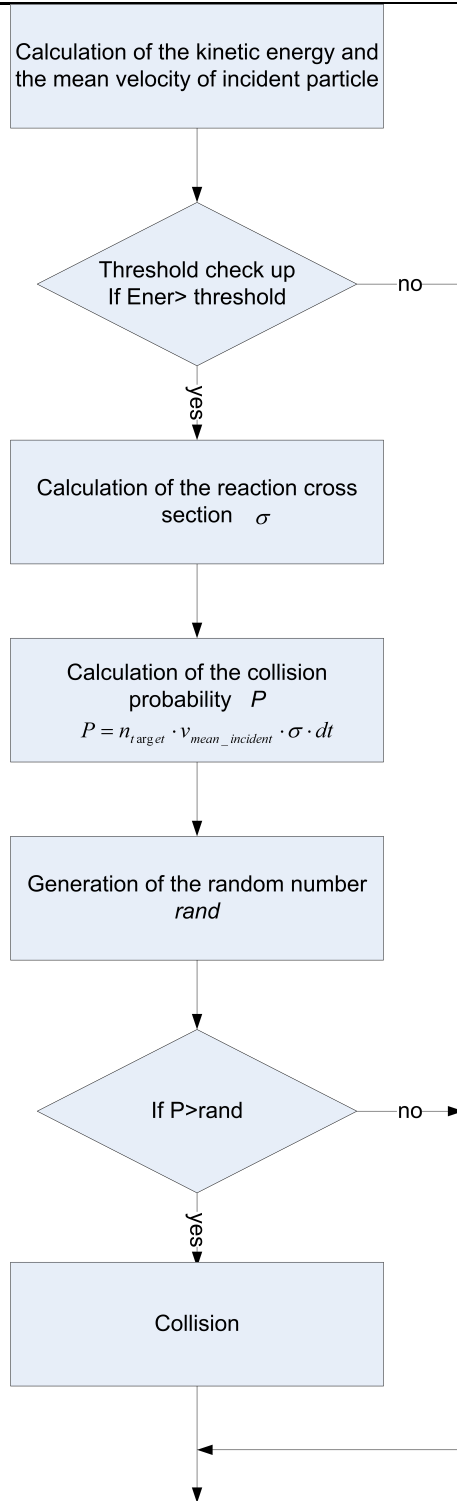


Figure 3.15: Chartflow diagram of the collision event (Collisions part of the general chartflow Fig. 3.3)

will destroy most of the negative ions produced in the expansion chamber before the extraction.

Another important way to produce negative ions (in ITER NBI source system) is from

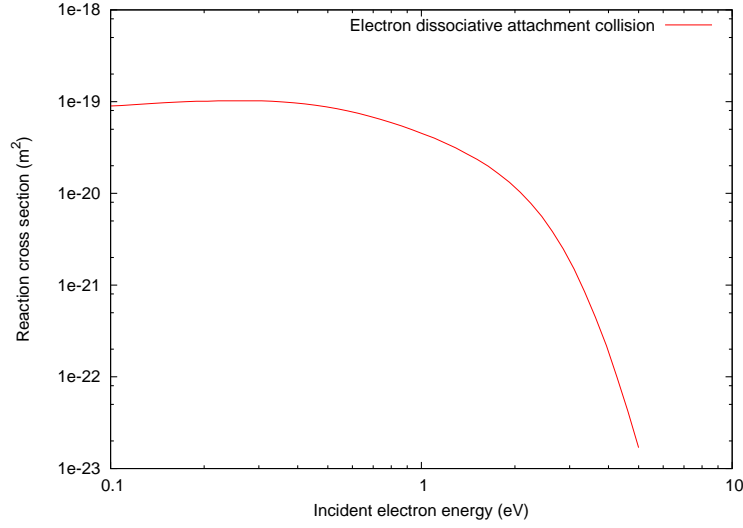


Figure 3.16: Cross section of the electron dissociative attachment reaction

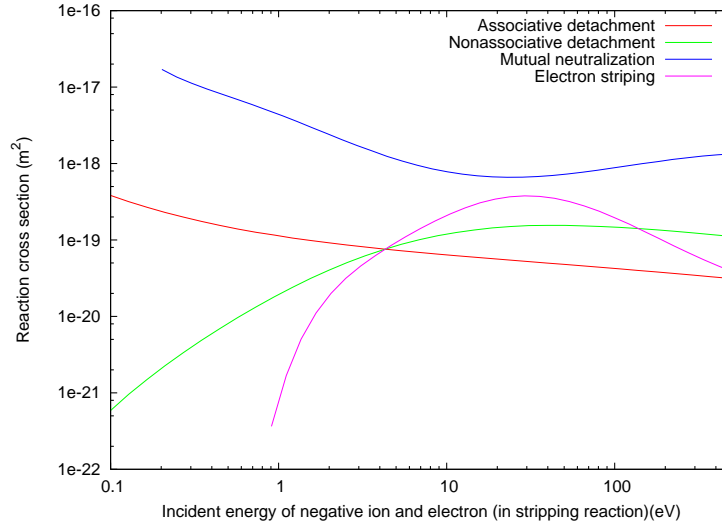
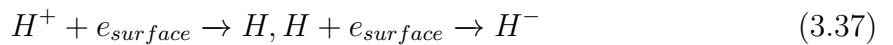


Figure 3.17: The cross-sections of the most important negative ion loss processes [54, 102]

the C_s covered plasma grid surface by the positive ions or neutral gas impact Eq. 3.37 [105]. First, the positive ions are transformed in neutrals by the Auger neutralization effect [106]. Affinity level of neutrals is shifted down and broadened when they reaches the surface. Overlap with metal states causes electron tunneling and negative ion formation [107]. Therefore, the covered materials with the lower work function gives the higher probability of the negative ion formation.

The positive ions (H^+ , H_2^+) which reach the plasma grid wall can produce NI if they get two e^- from C_s :



Seidl has derived universal expression for NI yield $Y(E_{in})$ by combining the electron tunneling and atomic scattering theories [108]. In the his formula Eq. 3.38 the negative

ion yield is completely characterized by two parameters: $R_N\eta_0 = 0.3$ and $E_{th}/R_E = 2$ eV [108] for both H^+ and H_2^+ ions, because most of the molecular ions are dissociated before colliding with the surface. Therefore, the negative ion yield is calculated as the function of the incident positive ions energy:

$$Y(E_{in}) = R_N\eta_0 \left(1 - \frac{E_{th}/R_E}{E_{in}} \right), E_{in} \geq E_{th}/R_E, \quad (3.38)$$

where R_N and R_E are the particle and energy reflection coefficients, η_0 is the height, E_{in} is the incident energy of the positive ion and E_{th} is the threshold energy:

$$E_{th} = \phi - E_A, \quad (3.39)$$

where ϕ is the material's work function (for Cs $\phi \sim 1.5$ eV), $E_A = 0.75$ eV is the electron Affinity of the hydrogen atom. Therefore, for Cs $E_{th} \approx 1.5 - 0.75 = 0,75$ eV.

In our calculation new born negative ions at the PG surface are released from the surface in normal direction with initial energy of ~ 1 eV due to the average energy of the sheath and the energy of the incident particles.

The most important process for negative ion production is the collision of the neutral gas (H , H_2) with the Cs covered surface [105, 109] because they need only one electron. To produce negative ions, neutrals must strike the wall with the energy larger than 2 eV [110] due to the Cs work function described above. However, they usually have not enough energy that leads to increasing the energy in the sheath close to the plasma grid. There are two main processes responsible for the creation of the high energetic neutrals: (i) resonant charge transfer of the atoms and molecular ions (Tab. 3.4, Reac. 7, 8) and electron dissociation (Tab. 3.4, Reac. 9).

The external potential applied between PG and EG penetrates deeply inside the expansion chamber, thus repelling most of the positive particles close to the extraction aperture creating the "meniscus". Eventually, the production of the negative ions by impact of H^+ and H_2^+ with the PG wall (described above) becomes inefficient. However, external positive potential does not have any influence on the neutrals flux onto the plasma grid surface. The neutral particles (H , H_2) colliding with the Cs covered wall could return as atoms or negative ions. The probability of becoming negative ions interacting with the surface is given by the Langmuir-Saha relation [111] that depends on the electron affinity and the surface work function. In our model we do not follow trajectories of the neutrals, but we treat them as a background gas with given density and temperature (Tab. 3.1). Because the calculation of the real flux of NI created by the mechanism described above is a very complex task, which is out of the scope of the present work. A parametric study of this value has been performed. The produced NI particles are launched with the initial energy of 1 eV normal to the surface. The emitted negative ion will move then towards the extraction grid and extracted or reflected back to the plasma grid wall due to the negative sheath in this region (more details of this phenomena will be discussed in the Chapter 5 of this thesis).

Due to the limitation of the real computation time the list of the reactions, that are included in the model, is restricted to the most important negative ion destruction and production processes. The elastic collisions are not taken into account in the present code version. All reactions included in the model are summarized in Tab. 3.4.

Table 3.4: Main volume reactions into the hydrogen plasma. * indicates the reactions included in the simulation model

#	Reactions	Process	Reference
(1)*	Electron dissociative attachment	$e + H_2(v) \rightarrow H + H^-$	[103]
(2)*	Associative detachment with H	$H^- + H \rightarrow e + H_2$	[54]
(3)*	Non-associative detachment with H	$H^- + H \rightarrow e + H + H$	[54]
(4)*	Electron detachment	$e + H^- \rightarrow H + 2e$	[54]
(5)*	Mutual neutralization	$H^+ + H^- \rightarrow H + H$	[54]
(6)*	Charge exchange with H	$H^- + H \rightarrow H + H^-$	[54]
(7)	Proton charge exchange with H	$H^+ + H \rightarrow H + H^+$	[104]
(8)	Proton charge exchange with H ₂	$H_2^+ + H_2 \rightarrow H_2 + H_2^+$	[104]
(9)	Electron dissociative excitation	$e + H_2 \rightarrow H + H + e$	[54]

3.12 Parallelization

The simulation of tens of millions of real particles during hundreds of thousands of iteration steps requires overwhelming computational time. The power of the parallel modeling has been used in the ONIX code for distributing memory among multi-CPU computers. The Message Passing Interface (MPI) was implemented in the program using the domain and particle decomposition methods. The code was run on the parallel machine that includes 24 cores (Fujitsu-Siemens RX600 R4, 48Gb RAM). This supercomputer has been generously granted by "Laboratoire de Physique des Gaz et des Plasmas (LPGP)", University Paris-Sud 11. In this section a brief synopsis of the MPI technique developed in the ONIX code will be outlined. The benefit of the parallel computation will be also presented.

MPI is the application programming interface (API), which allows multi-CPU's to communicate with one another. The communication is performed by sending and receiving messages between the processes. MPI was first realized in 1994 by William Gropp [112], and since then it has been widely used in the area of numerical calculations. The MPI technique is explained in detail in many books [113, 114], and has been successfully applied to many PIC programs.

3.12.1 Initialization

The MPI initialization begins with the introduction of a number of required processors (this number is determined by user manually) that will perform simultaneous calculations. The procedure starts with the following commands:

```
MPI_INIT(ierr)
MPI_COMM_RANK(MPI_COMM_WORLD,rank,ierr)
MPI_COMM_SIZE(MPI_COMM_WORLD,numtasks,ierr)
```

where the *numtasks* variable denotes the amount of required processors used in particular simulation, *rank* is the unique identity number assigned to each processor (from 0 to *numtasks*-1), and *ierr* is the error message in case of initialization failure.

During the next step all processors allocate their own memory for initialization of the calculating matrices and data structures. MPI widens possibilities of the model in terms of the amount of computational particles and domain size. For instance, the maximum number of the allocated particles in one CPU is restricted to the RAM computer memory. In general, about 10 million particles (with data type of double precision) can be introduced in one personal computer with 4 Gb RAM memory. In the parallel version, each CPU will be able to contain this quantity, enabling the total number of simulation particles being 10 millions \times *numtasks*.

The division of the simulation domain then follows. In the ONIX code the simulation domain (Fig. 3.1) can be separated between all processes in three spatial directions (x , y , z). The addition routine has been developed in order to perform automatic domain division between all MPI-CPU. This function defines the size and the boundaries of each processor. In the standard configuration the code has been run on 18 CPU. However, the variety domain division structures have been tested in order to find the most suitable for our model; among them were such as $18 \times 1 \times 1$, $1 \times 2 \times 9$, $2 \times 2 \times 4$, $2 \times 3 \times 3$, etc in x , y , z directions. For efficient calculation, each processor should include a maximum domain volume with a minimum area size. Therefore, the configuration with $2 \times 3 \times 3$ processes has been chosen as the most appropriate for our system.

3.12.2 Particles Injection

Depending on the method of plasma creation, particles could be injected by huge portions during the first iteration, or may need to be injected each iteration step. However, in the former algorithm, when a particle leaves the simulation domain, another particle of the same kind should be added to the system. Moreover, the negative ions flux from the plasma grid wall, that represent production of the NI *via* the neutral gas impact explained in Sec. 3.11.3, causes the regular injection of new particles into the simulation volume.

Usually, parallelization of such particle injection routine is simple in implementation. All CPU execute the same injection function, where the particles "obtain" their position, velocity, identity number and type.

The main disadvantage of this method is that number of particles injected per CPU is unbalanced. For instance, the process which controls injection of NI from the PG wall would contain more particles than the process at the extraction plane. The accumulation of the injected particles in one process could overload CPU, decreasing the global efficiency of the parallelization. This problem has been partially alleviated by the division of the particle injection region between more processors and put less processors in the initially empty domain region.

3.12.3 Charge Assignment and Field Projection

At each iteration step, the charge of all simulation particles is assigned to the eight nearest PIC nodes as detailed in Sec. 3.7. The problem arises during this procedure in parallelization, when particles are located between the boundaries of two or, sometimes, four processors (Fig. 3.18). In this case, the particle purely refers to one process, but its charge should be distributed between several processes. The assignment of full charge to

the paternal process will lead to diminishing stability of the calculation and decreasing of the program accuracy. The problem has been resolved by adding one supplementary external plane to each process from all sides. These planes relate to two neighboring processes and play role of the last plane of the first process and the first plane of the neighboring process. After the charge projection procedure, the neighboring processes exchange with each other by these virtual planes. Thus, the correct profound charge distribution is obtained.

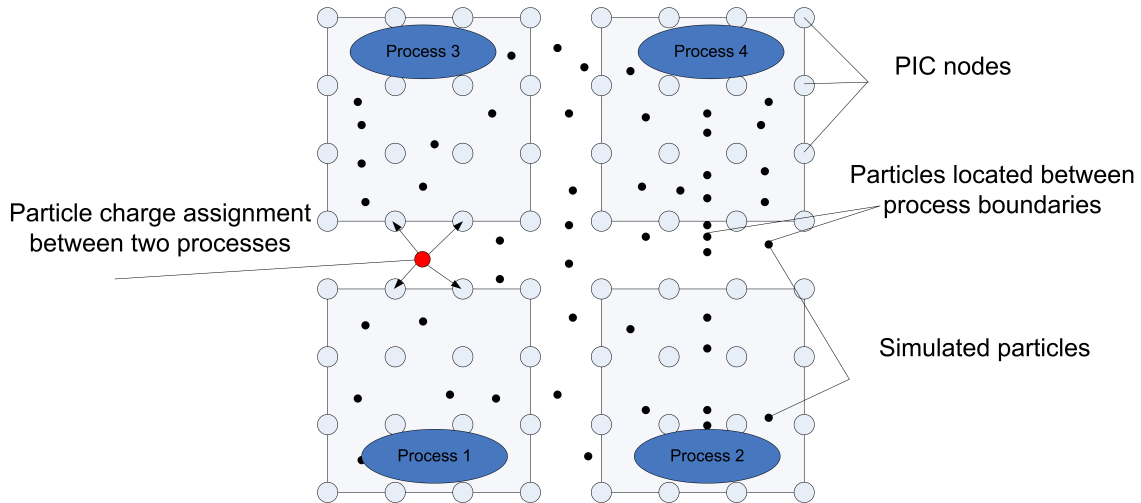


Figure 3.18: Charge assignment procedure of the particles that are located between the processes boundaries

The field projection to the particles is the reverse procedure to the charge assignment routine. Here, the calculated force at the PIC nodes should be interpolated to the particles location. Difficulties appear during the parallelization phase in the same place as in the charge assignment routine, when particles are placed between the process borders (Fig. 3.18 - red particle). The calculated force at the boundaries nodes from two processes must be projected to the particle located in one of them. The virtual auxiliary planes from the charge assignment routine have been used also in the field interpolation procedure. It allows to project full force distributions, thus improving program accuracy.

3.12.4 Poisson Solver

The calculation of the potential distribution involves solving of the Poisson equation. The method for resolving this equation and its discretization is outlined in detail in Sec. 3.8. Let us remember, that in order to calculate the potential value at the PIC node with coordinate $\phi_{i,j,k}$ the descriptions of the next ($\phi_{i+1,j,k}$) and previous nodes ($\phi_{i-1,j,k}$) are required. A problem in parallelization procedure arises again at the boundaries points. The potential calculation at the boundaries node needs the data of the potential value at the first or last plane of the neighboring process. This problem has been eliminated by exchanging the boundaries planes between neighboring tasks (Fig. 3.19). Consequently, all processes will be informed about the boundaries potential distribution of their neighbors in parallel calculations.

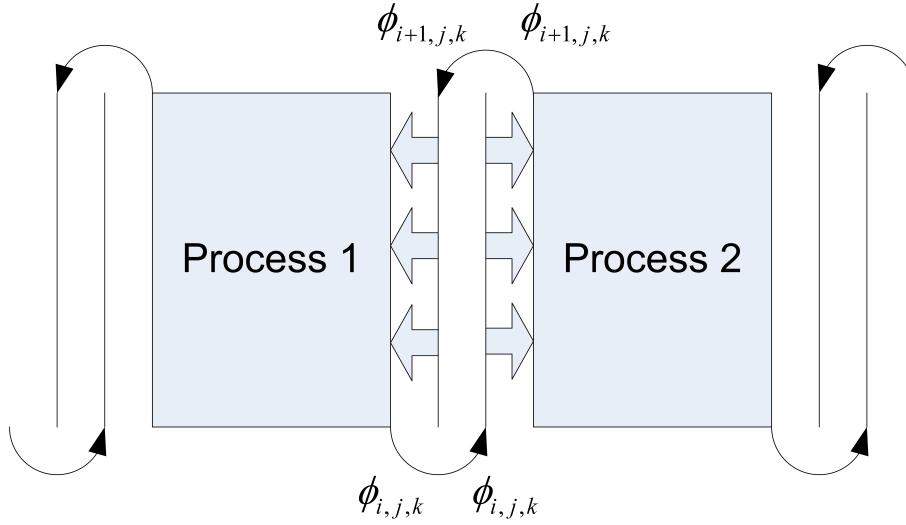


Figure 3.19: Schematic view of the boundaries potential data exchanging between parallel tasks

The iterative conjugate gradient algorithm, which is used for obtaining the solution of the Poisson's equation, requires a calculation of the global error. However, the parallel processes are able to entirely compute the error value only of their chunk. This problem has been simply resolved by a call of the MPI command *MPI_Allreduce*. This function sums up the error value of each individual process and broadcasts a copy of the global error back to each parallel task. The same function has been used in the code in order to estimate the total number of each species at each time step in the simulation domain. The total extracted electron and negative ion currents among all processes at the right boundary of the simulation domain have been calculated by using the same function.

3.12.5 Particle Movement

One of the most important and time consuming steps in the PIC code is the particles motion. During this step position and velocity of each individual particle are updated due to the precalculated electric and static distribution of the magnetic fields. The parallelization of this stage is more or less straightforward; each process governs the particles which are located in its chunk. All processors have full information about the force acting on the particles, geometry of the part of the domain where particles are placed, and other necessary quantities for realizing this procedure. Complications in parallelization of this routine arise when a particle moves from one process to another during one time step.

The modified MPI sending and receiving functions have been leveraged to transfer particles between the processors. Each particle is described by a complex numerical data type structure: 3 variables correspond to the particle positions ($P.x, P.y, P.z$), 3 variables denote the particle velocities ($P.vx, P.vy, P.vz$), the particle type (electron, positive ion ... - $P.sp$) and the particle unique identity number ($P.id$). According to this structure *MPI_SEND* and *MPI_RECV* functions have been slightly updated in order to transfer the correct memory part corresponding to full description of one particle.

Let us remember that periodic boundaries conditions are used in vertical z and horizontal y directions. Therefore, if a particle leaves the simulation domain from the top, it should be injected from the bottom with the same velocity components. Such particles transfer between parallel processors requires knowing of the address and the *rank* of the sending and receiving processes. Usually, one process knows only information about its neighbors (addresses and ID numbers), but does not have any data about the task located at the opposite side of the simulation domain. Therefore, auxiliary routine has been implemented in the ONIX code to precalculate the positions and addresses of the parallel processes that are placed at the periodical boundaries of the simulation volume in all configurations of the domain interface.

In the later version of the ONIX program the particle transmission routine has been modified to increase the computational efficiency. In the first code version each particle that leaves one process is being directly sent to the receiving process. However, this procedure requires excessive computational time. It has been decided that such particle transfers will be performed only once per iteration. All particles, which must be sent to other process, are grouped in special matrix and it is transmitted in the end of the routine. After all particles have been moved, the actual transition occurs. Therefore, the particles are interchanged between neighboring CPU only once per time step. If a process is currently not sending information, it is waiting to receive it. Such modification alleviates communication between the processes and speeds up the simulation.

3.12.6 Parallelization Efficiency

In most cases the ONIX code has been launched on the Fujitsu-Siemens RX600 R4 parallel machine. The benefit from the code parallelization has been estimated by running the same version of the program during 2000 iterations on different number of the working processors. The parallel efficiency is estimated as acceleration of the program execution. The code performance on 1, 4, 8, 12, 18, 24 CPU has been tested. The program acceleration has been then measured and results are represented in Fig. 3.20.

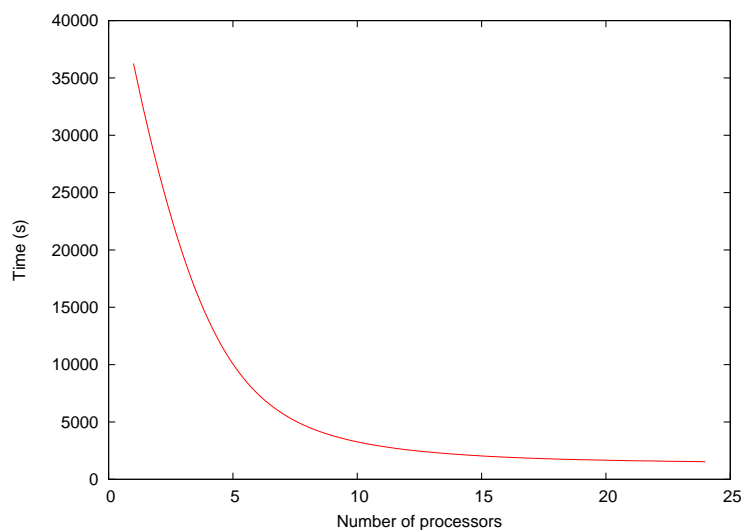


Figure 3.20: Computational time as the function of amount of the processors working in parallel

When more processors are used the acceleration increases to a certain point. After that, starting from 20 CPU, communication between the processes takes more time than the time necessary for the code performance. Therefore, it has been decided to launch the code on 18 processors in the standard program configuration.

3.13 Numerical Check-up

With the successive development of the ONIX program, various tests have been applied to each new module of the code in order to prove their validity. The tests have been done on a basis of an individual module and in combination with other parts of the code. By conducting such tests we obtained important confidence in the accuracy of our code before it was actually applied to simulate the extraction of negative ions in the ITER NBI source system. Therefore, in this section different program tests, starting from simple single particle trajectories for fulfilling field calculation procedure, will be outlined.

3.13.1 Particle Motion Tests in Constant Field

In order to verify the accuracy of the particle motion integrator, a few simple low-level tests have been undertaken. The trajectories of a single computation particle with positive, negative or zero charges have been recorded under the influence of the magnetic and electric fields constant in time. Different mass ratios have also been tested.

The first simple test included the trajectories of 3 particles with negative, positive and zero charges in a three-dimensional mesh. Each particle had the same mass and was placed in the middle of the first box of the computation domain with coordinates $x = 8$ mm, $y = 10$ mm, $z = 10$ mm. Each particle was sent in different direction with the identical initial velocity of 10^5 m/s. The negative particle was pushed in positive axial direction ($v_x = -10^5$ m/s, $v_y = 0$, $v_z = 0$), the positive charge - in negative axial direction ($v_x = -10^5$ m/s, $v_y = 0$, $v_z = 0$), while the neutral particle - in y direction ($v_x = 0$, $v_y = 10^5$ m/s, $v_z = 0$). The magnetic and electric fields were not present in this calculation.

The results of the test are shown in Fig. 3.21. The first important conclusion from the simulation is that the trajectories of all particles remain entirely straight due to the absence of external forces and applying constant initial velocity. Also, it is important to note that all particles traveled exactly the same distance. Therefore, all types of charge are treated in the same way in the case of zero fields. The distance (1 mm), which all particles passed during 1000 iterations also corresponds to the time step used in the simulation ($\Delta t = 10^{-11}$ s).

3.13.2 Particle Motion Test at Constant B Field

Having proved the rightness of the particle motion integrator in the absence of electromagnetic fields in the previous section, now it is important to show the correctness of the particle motion routine in the presence of external forces. The following test involves calculation of the charged particle trace under the effect of magnetic field. The same three particles, as in the test described above, are introduced in the same position. However, the initial velocities $v_x = 10^5$ m/s, $v_y = 0$, $v_z = 0$ are applied to all species. The magnetic

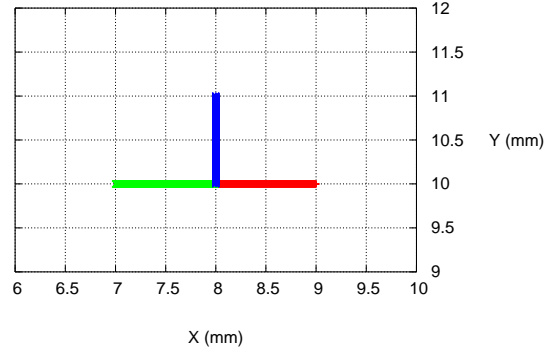


Figure 3.21: Trajectories of three charged particles released from the middle of the computation domain in the absence of electric and magnetic fields. All particles pass the same distance retaining accurately straight trace

field with the constant value of 0.0005 T is installed in the system oriented in vertical z direction, when the electric field is set up to zero. In this test uncharged particle should be unaffected by the magnetic field, while the particles with the negative and positive charges should perform the cyclotron motion with gyration radius given by:

$$r_L = \frac{m * v_{\perp}}{|q| * B} \quad (3.40)$$

where r_L is the gyro radius, m – is the mass of a particle, v_{\perp} is the velocity component perpendicular to the direction of the magnetic field, q is the particle charge and B is the magnetic field strength. The analytical value of r_L with overhead parameters is ~ 0.0011 m. Fig. 3.22 depicts the particle trace for this test. As it has been expected, the charged particles gyrate in the magnetic field, while the neutral ones have straight trajectory. The simulated gyro radii of the positive (green line) and negative (red line) particles are entirely the same and correspond to the precalculated analytical value of 1.1 mm for a particle with charge $q = 1.6e^{-19}$ C and mass $m = 9.1e^{-31}$ kg. From this test, we also have to note that negative charge makes clockwise turn, while the positive charge performs opposite gyration.

3.13.3 Mass Checking

In all previous tests the electron mass was assigned to all simulated particles. It is also important to verify that the particle motion integrator scales the particle trace properly when the mass is scaled. In the current test two negatively charged particles are placed in the same position, as in the tests described above, with coordinate $x = 8$ mm, $y = 10$ mm, $z = 10$ mm. The mass of the first particle is ascribed to the electron mass, while the second particle is assigned to two electron masses. The initial velocity of 10^5 m/s in axial direction is set for both particles. The constant magnetic field distribution of 0.0005 T is oriented in z direction. The analytical Larmor radius is calculated again; for

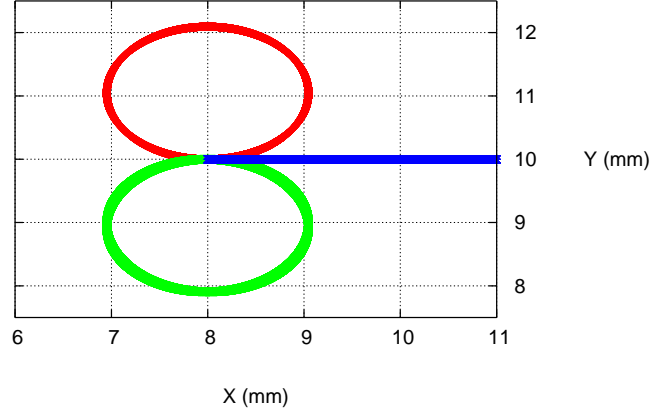


Figure 3.22: Trajectories of three particles with negative charge (red line), positive charge (green line) and zero charge (blue line) in the constant magnetic field of $B_z = 0.0005$ T

a heavier particle it must take the value of 0.0002275 m, while the particle with electron mass must have the radius exactly half of that (~ 0.0001136 m).

The trajectories of the simulated particles are depicted in Fig. 3.24. The green line corresponds to the particles with heavier mass, when the red line represents the particle with electron mass. The computed Larmor radii of both particles are in agreement with the theoretical values calculated above. Thus, the rightness of the scaling factor has been proved using the example of the particles motion with different masses.

3.13.4 Particle Motion Test in Constant $\mathbf{E} \times \mathbf{B}$ Field

In the preceding two sections we have proved the correctness of the particle motion integrator in the presence of magnetic field. The next step is to demonstrate accuracy of the particle trajectories in the electromagnetic field system.

In this test three particles with negative, positive and zero charge are used again. However, their initial position is changed. The negative charge is placed at the bottom of the simulation domain, with coordinates $x = 8$ mm, $y = 1$ mm, $z = 10$ mm, the positive charge is located in the middle of the simulation domain $x = 8$ mm, $y = 10$ mm, $z = 10$ mm, and the neutral one takes position at the top $x = 8$ mm, $y = 11$ mm, $z = 10$ mm. The constant magnetic field of 0.0003 T is used in z direction, while the constant electric field of 1.1 V/m is set in y direction. The velocity distribution of charged particles are left as in the previous test - 10^5 m/s in the axial direction. However, the velocity of the neutral particle is assigned 3667 m/s. This velocity corresponds to the guiding center drift velocity of the charged particles:

$$v_{E \times B} = \frac{E \times B}{B^2} \quad (3.41)$$

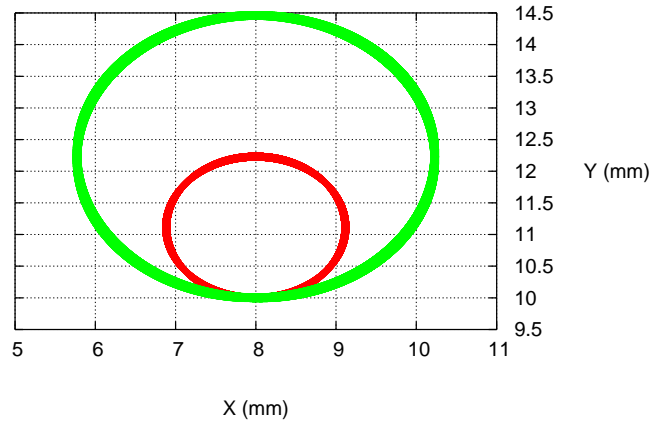


Figure 3.23: Trajectories of the negative charged particles with mass ratio 2 in the constant magnetic field $B_z = 0.0005$ T

The trajectories of the three particles are shown in Fig. 3.24. The charged particles clearly execute $E \times B$ drift as it was expected. In the end of the trace it is seen that positive charge performs clockwise turn, while the negative charge revolves in the opposite clockwise direction, as it should be. Also, it has to be noted that the radii of both charged particles are constant and stable throughout revolving.

The guiding center of the drift motion moves with the same velocity as the neutral particle, as was expected in the beginning. It is also evident from the trajectories length of all particles that they are nearly the same. Therefore, the correctness of the particle motion integrator has been verified and proved in 3 cases: without external force, with constant magnetic field, and under the influence of both the magnetic and electric fields.

3.14 Electric Potential Test

One of the decisive parts of the electrostatic PIC code is the solver of the Poisson equation. In our program potential distribution is calculated by the iterative precondition conjugate gradient method. In this section the accuracy of this algorithm developed in the ONIX code is demonstrated.

In order to verify the potential computed value, a test of the electric dipole potential is executed. Two opposite charged particles are placed in the middle of the computation domain 1 mm separated from each other. We set the particle charge which equals 10^5 elementary electron charges ($1.6 \times 10^{-19} \times 10^5$) for better potential visualization. The analytical value of the electric dipole potential at R distance has been calculated by superposing the point charge potentials of two particles:

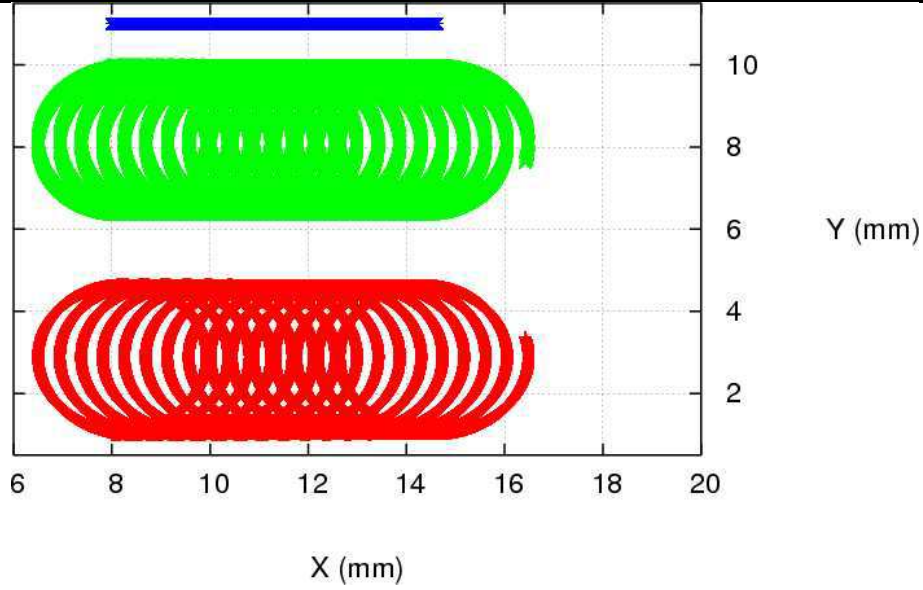


Figure 3.24: Trajectories of the negatively charged (red line), positively charged (green line) and neutral particles under the influence of the $E \times B$ drift

$$\phi(R) = \phi(r_+) + \phi(r_-) = \frac{1}{4\pi\epsilon_0} * q \left(\frac{1}{r_+} - \frac{1}{r_-} \right) \quad (3.42)$$

where $\phi(R)$ is the calculated potential, q is the particle charge, and r_+ and r_- are distances from the calculated potential point to the positive and negative charge respectively.

The simulated potential distribution is depicted in Fig. 3.25. The potential isolines are bended as it was expected in the dipole structure, with 0 V in the center between two charges. The potential value of ~ 0.0384 V was theoretically calculated at the distances of $r_+ = 1.5$ mm and $r_- = 2.5$ mm from the positive and negative charges respectively. From the simulated test the potential value at such distances is almost the same (~ 0.039 V). The reason for such a small difference could be the precision of the Poisson solver or numerical (truncation) error.

The electric field has been also calculated by using the potential distribution shown in Fig. 3.25. In theory, the electric dipole field should form a specific "clover" structure. Fig. 3.26 shows the distribution of electric field in x direction. The strong field is observed between the charges, while the weak field is placed at the edge of the simulation domain. The "clover" structure is clearly visible in the figure. Therefore, these simple tests have shown the correctness of the field solution and validity of the Poisson solver implemented in the ONIX code.

3.15 Plasma Oscillation Test

Considering the rightness of the particle motion and the Poisson solver routines implemented in the program, the next logical step is to demonstrate the accuracy of the code

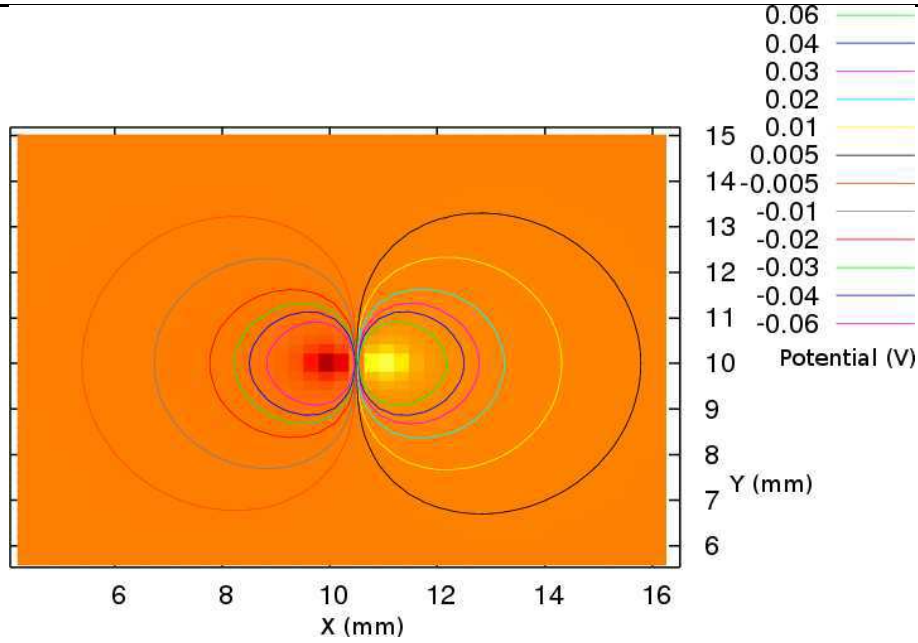


Figure 3.25: The electric dipole potential distribution computing by the Poisson solver implemented in the ONIX code

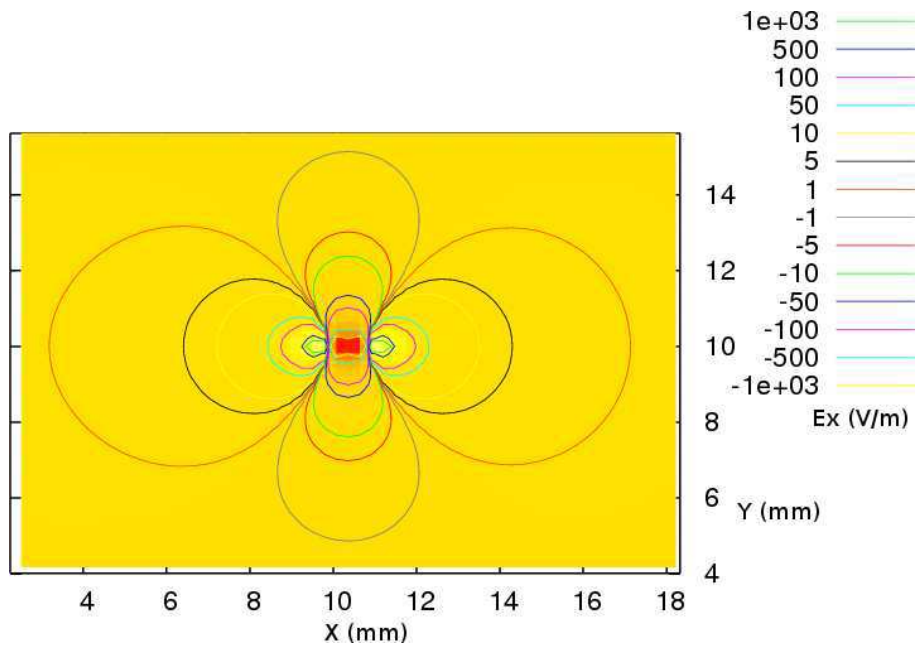


Figure 3.26: The distribution of the electric dipole field in x direction calculated by the ONIX code

performance in a combination of both parts of the program. In order to verify this portion of the code, the cold Langmuir oscillation test was fulfilled.

Langmuir oscillation, also know as the plasma oscillation, is fast periodic oscillation of the electrons in the neutral plasmas. If the neutral plasma is assumed to be in the system, the electron charge will oscillate at the plasma frequency:

$$\omega_{pe} = \sqrt{\frac{n_e * q^2}{m * \epsilon_0}} \quad (3.43)$$

where n_e is the electron density, q is the elementary charge, m is the electron mass, and ϵ_0 is the permittivity of free space.

In this test, particles are placed in the middle of the simulation domain (in $x - y$ plane) forming a square. The density of the electrons and positive ions are the same: $n_e = n_{H^+} = 1.2 \times 10^{17} m^{-3}$. The theoretical value of the plasma period is ~ 300 simulated time steps. The initial velocities of all species are assigned zero. The potential distribution along the simulation volume is depicted in Fig. 3.27, with four different time steps separated by a half of the plasma period. Fig. 3.27 (a) and (c) show two peaks of the plasma potential, while Fig. 3.27 (b) and (d) give two minimums. The electric potential fluctuates at the same rate as the electron charge density, and moves from maximum to maximum during one plasma period.

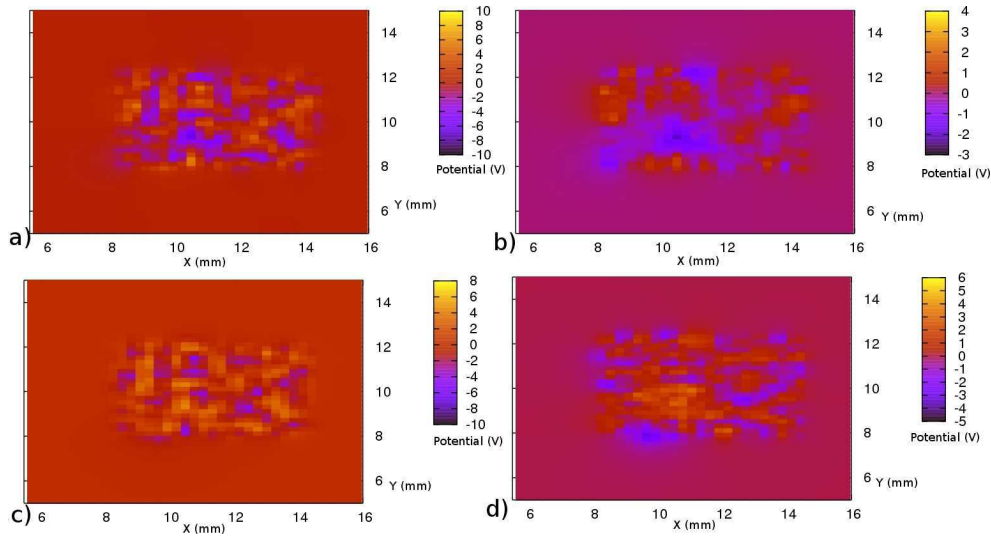


Figure 3.27: Snap shots of the potential distribution at four simulation instants separated by \sim half plasma period

3.16 Parallelization Test

Given that particle motion integrator has been correctly developed in the ONIX code, the next step is to demonstrate the correctness of the particle motion routine in the parallel computation, when the simulated particle moves from one processor to another. The periodic boundary conditions has been also verified during this test.

The electron is placed in the middle of the simulation domain ($x = 10$ mm, $y = 10$ mm, $z = 10$ mm), with the following initial velocities: $v_x = 10000$ m/s, $v_y = 50000$ m/s, $v_z = 100000$ m/s. The magnetic and electric fields are switched off during the test. The simulated domain is divided between 18 processors – $2 \times 3 \times 3$ in x , y and z direction respectively. The electron trajectory is depicted in Fig. 3.28 in the $x-y$ plane. Different

colors show the process through which the electron is currently moving. From this figure one can see that the electron jumps from one CPU to another, preserving straight trajectories. Therefore, it shows correctness of communication between the processes implemented in the ONIX program. Also, we need to note that when the electron attains the domain boundary ($y = 20$ mm) it is reinjected from the other side with the same x and z coordinates. Thus, it proves the accuracy of the periodic boundary conditions applied in the system.

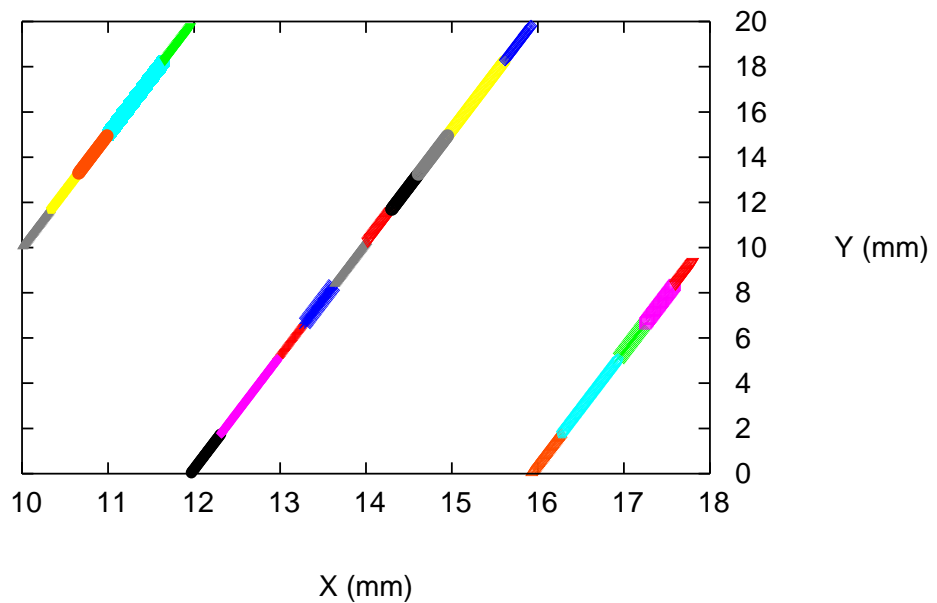


Figure 3.28: Parallel computation of the electron trajectory. Each color indicates different processor corresponding to the domain through which the test electron moves

Chapter 4

Results in Collisionless Approximation

After the numerical model development, implementation and test, the next step is to check the program behavior for the real application such as negative ion extraction from an electronegative plasma. This chapter presents the first results of our code in the collisionless plasma approximation (Collisions between the particles are not included in the model). The necessity of full 3 dimensional model is proved by the symmetry breakup induced by the complex magnetic configuration. In the end of the chapter the first evolution of the extracted NI and co-extracted electron currents are given.

4.1 Self-consistence of the Meniscus Formation

The results presented in this section were obtained with using the simulation model shown in Fig. 3.1. However, a cylindrical shape of the plasma grid aperture was assumed. The simulations were performed using an initial plasma density filling the left region of the simulation chamber, as shown in Fig. 3.1. Between $x = 0$ and $x = 6$ mm we assume that the plasma properties are the same than in the expansion box, and we set the density to $n_e = 10^{17} \text{ m}^{-3}$. Between $x = 6$ mm and $x = 15$ mm we consider a more diluted plasma ($n_e = 0.5 \times 10^{17} \text{ m}^{-3}$), corresponding to the pre-sheath. The negative ions were absent in this calculation, i.e. plasmas includes only electrons and positive ions. Electron and ion temperatures are 3 and 1 eV respectively.

After $0.3 \mu\text{s}$ of the computational time, the system has evolved to a situation close to the steady state (discussed below). At this time, the plasma screens efficiently the external extraction field, adopting the meniscus shape (Fig. 4.1). The denser plasma band at the left side of the simulation box has not been affected by the plasma density redistribution close to the extraction aperture.

The final state of the system is relatively weakly affected by its initial state. For example, if the length of the dilute plasma region is reduced by half, the final shape of the meniscus is only slightly affected (Fig. 4.1 and 4.2). A more detailed comparison requires to continue the simulation to much longer times to truly reach the steady state, specially in the second case of a half length pre-sheath.

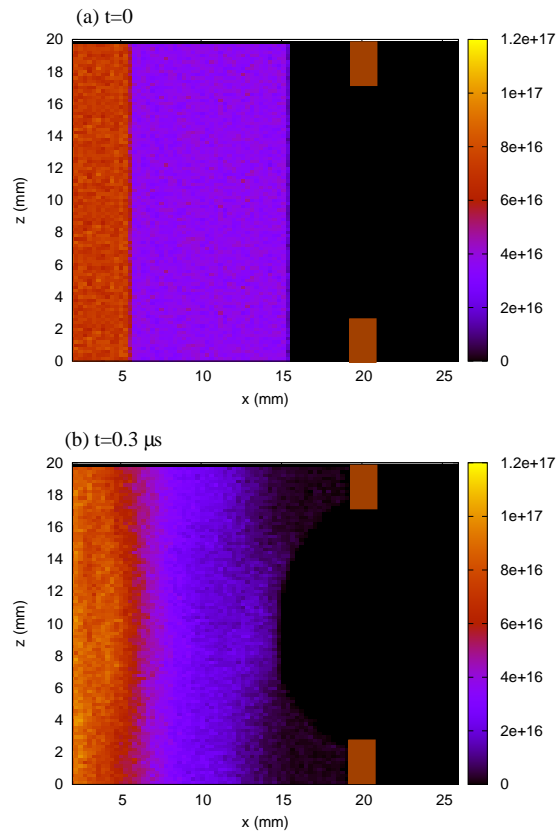


Figure 4.1: Spatial distribution of ion density in the plane $y = 10$ mm at the beginning of the simulation (a) and at $t = 0.3 \mu\text{s}$ (b)

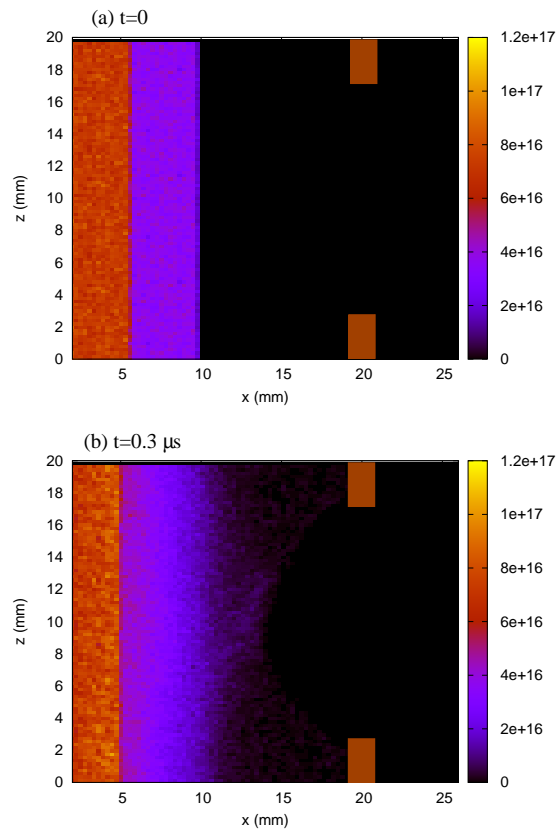


Figure 4.2: Spatial distribution of ion density in the $x - z$ plane at the beginning of the simulation (a) and at $t = 0.3 \mu\text{s}$ (b). The pre-sheath lies from $x = 5$ to $x = 10$ mm

4.2 Calculation of Potential Distribution

Fig. 4.3 shows the electrostatic potential at the beginning of the simulation and after $0.3 \mu\text{s}$. The larger plasma condition, from $x = 0$ to $x = 15$, mm is assumed. At $t = 0$ the external electric field deeply penetrates in the expansion chamber Fig. 4.3 (a). Once that the plasma screening occurs, the iso-potential lines are pushed towards the walls. The potential is constant in most of the volume, meaning that electric field vanishes. Later in the manuscript is described how this affects the extraction of negative ions.

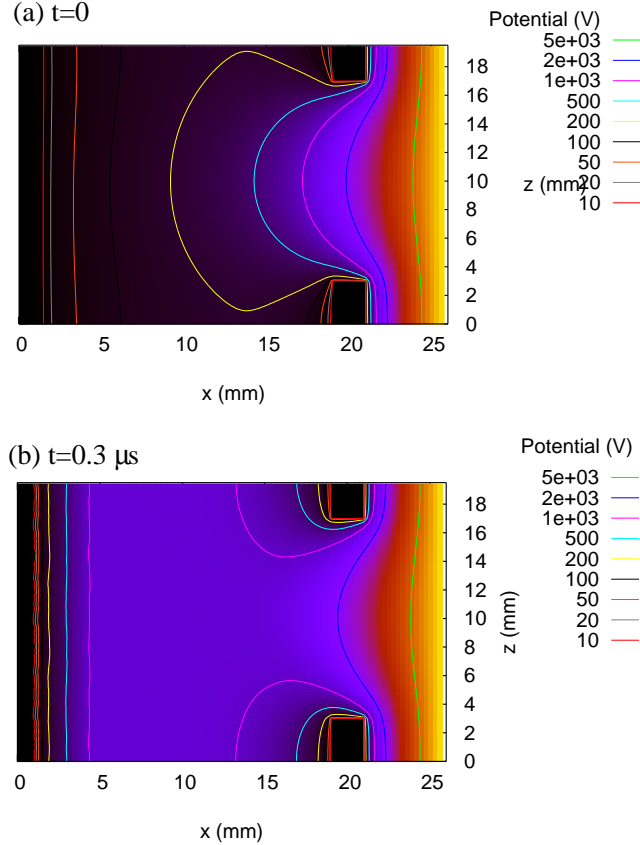


Figure 4.3: Spatial distribution of electric potential in the $x - z$ plane at the beginning of the simulation (a) and at $t = 0.3 \mu\text{s}$ (b) for the "large" initial plasma. The pre-sheath lies from $x = 5$ to $x = 15$ mm

4.3 Extracted Electron Current

As mention above, a significant number of electron is co-extracted together with NI. Fig. 4.4 shows the time evolution of the extracted electron current crossing the right side of the simulation box, that is roughly equal to the current crossing the PG aperture. Here we have to take into account that this current is calculated 4 mm after the PG and it is larger than the electron current entering through the aperture of the extraction grid. Most of the electrons reach the right side of the simulation box with very large transverse velocity due to the deflecting field and they will hit the EG wall or the vessel. At the

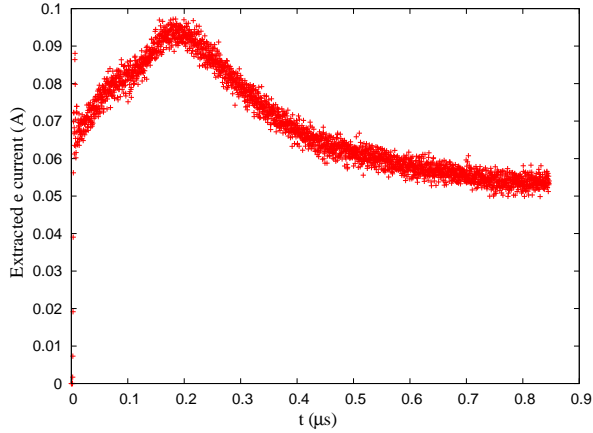


Figure 4.4: Extracted electron current vs. time for an electropositive hydrogen plasma

beginning of the simulation, the electron current grows very fast, because the extraction potential is not screened. The growing of the extracted electron current continues up to $t = 0.2 \mu\text{s}$. At this time, the plasma screening of the extraction potential starts being efficient, reducing thus the fraction of extracted electrons. From this moment there is a smooth decreasing of the electron current, but a real steady state is not reached even at $t = 0.9 \mu\text{s}$. Inspection of the potential distribution shows that the changes in its magnitude are very small ($<2\%$) when the computation time is larger than $t = 0.6 \mu\text{s}$. Consequently, to limit computing cost, simulations are performed up to this time. The longer time evolution of the system could be the subject of future studies.

4.4 Simulation with Negative Ions

In the next simulation negative ions at the first time have been introduced in the model. The plasma included 10% of the negative ions (H^-), 90% of electrons and 100% of H^+ (H_2^+ and H_3^+ ions are not included in this simulation). The potential obtained in this calculation is similar to the one obtained without NI, although the screening is slightly better (Fig. 4.5). On the other hand, the time evolution of the system is very different. Fig. 4.6 shows the extracted electron and negative ion currents for this case. As it can be seen, the steady state is reached much faster than in the electropositive plasma (Fig. 4.4), even if the asymptotic values for the electron current are similar in both cases. The initial overshooting due to a large charge separation caused by the unscreened extraction potential becomes less strong because of the presence of negative ions. The displacement of NI during the initial transient phase is much smaller than for electrons. The charge separation is therefore smaller, allowing the system to approach faster the steady-state. The first negative ions are extracted at $\sim 0.2 \mu\text{s}$. The electron current is roughly 10 times larger than the negative ion current.

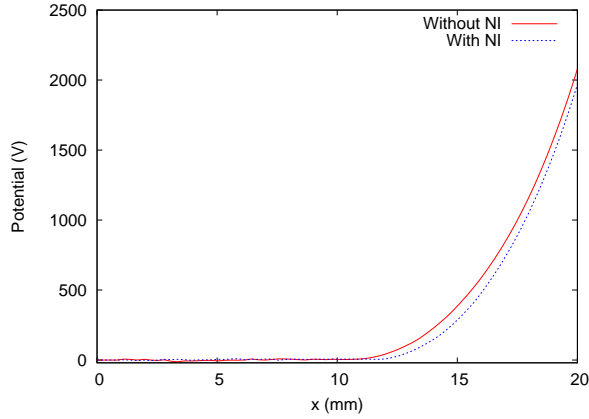


Figure 4.5: Quasi steady-state potential profile at the axis ($y = 10$ mm, $z = 10$ mm) without NI and with 10% of NI in the plasma volume (the figure is cut at point $x = 20$ mm in order to distinguish the potential difference between two cases)

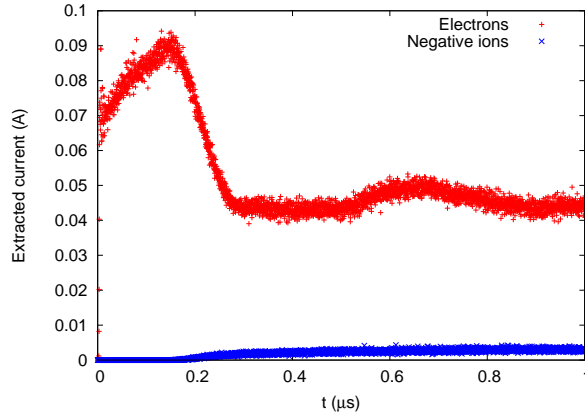


Figure 4.6: Extracted electron and NI current vs. time for the plasma with 10% of negative ions in the plasma volume

4.5 Symmetry Breakup

As mentioned above, the presence of the filter and deflecting magnetic fields breaks the cylindrical symmetry of the problem, making necessary a full three-dimensional description. The combination of the filter field (oriented in vertical z direction) with the extraction field results in $\vec{E} \times \vec{B}$ drift in the horizontal y direction, whereas the drift in the vertical z direction is produced by the deflecting field (oriented in y direction). The asymmetry caused by these drifts is apparent in the spatial distribution of charge. The positive ion charge distribution in the vertical midplane ($z = 10$ mm) and in the horizontal midplane ($y = 10$ mm) are shown in Fig. 4.7, for the plasma without NI. In the first case, we can see that ions pile up in the upper part of the $x - y$ plane. Ions are not magnetized, and therefore they are not subject to the $\vec{E} \times \vec{B}$ drift. Nevertheless, the drift associated with the filter field push electrons to the upper part of the $x - y$ plane. This produce charge separation, creating an electric field that push the ions in the same direction as the electrons. The effect of the drift over the electrons results in

an asymmetric ion spatial distribution, even if ions are not magnetized.

On the other hand, the effect of the drift associated with the deflecting magnetic field, larger than the filter one close to the PG aperture (see Fig. 3.12), is stronger. As it can be seen, in the horizontal midplane (Fig. 4.7.b), the meniscus shape is much more distorted, and the asymmetry is more marked.

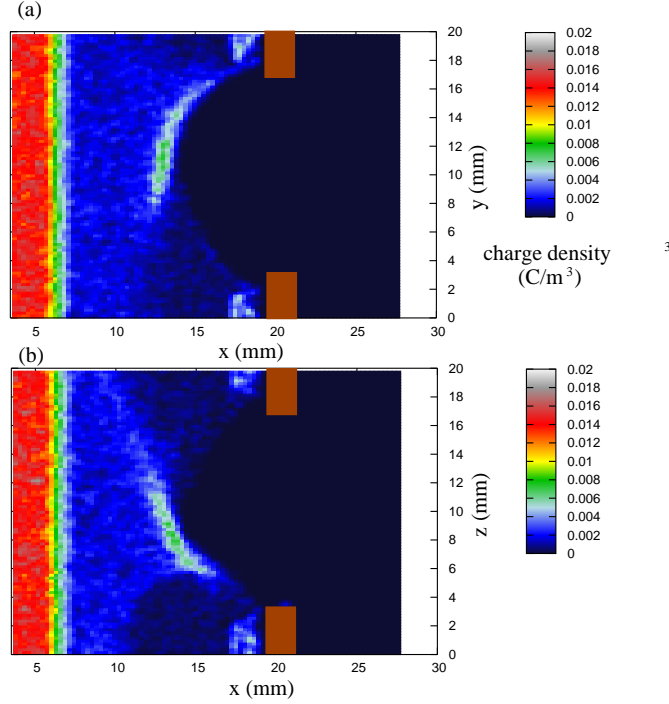


Figure 4.7: Positive ion charge distribution in the vertical midplane (a) and in the horizontal midplane (b). The plasma is composed by the electron and H^+

4.6 Magnetic Fields Effect on the Extracted Electron Current

To illustrate the role played by each field, we performed a simulation using only the filter field. The electronic charge density distribution in the horizontal midplane, shown in Fig. 4.8.a), is similar in the upper and lower regions. In fact, the effect of the drift created by the filter field, in the y direction, is not visible in this plane. Note also that a significant number of electron escape though the aperture, leaving the simulation box by the right side. When the deflecting field is included, the drift produced in z direction changes dramatically the electron density distribution close to the hole. The field is able to deflect most of the electrons (Fig. 4.8.b).

To bring a further illustration of the importance of the symmetry break produced by the magnetic fields, we calculated the trajectories of negative ions (as test particles) in the potential screened by the plasma obtained with the code and in the vacuum external potential (obtained with the code without plasma). In both cases the filter and deflecting magnetic fields are included. Negative ions are initially at rest at $x = 16$ mm, close to the

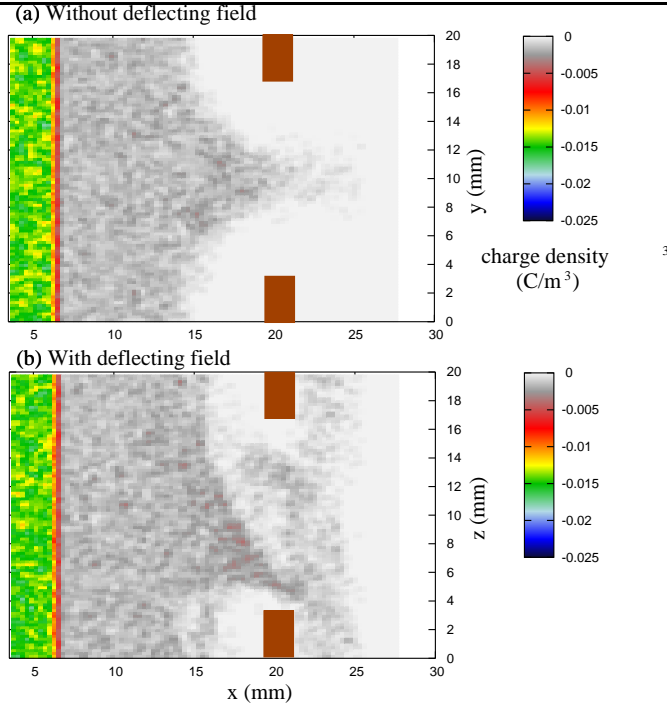


Figure 4.8: Electron charge distribution without (a) and with (b) the deflecting field in two different planes (a:x-y plane, b:x-z plane)

extraction aperture. They are disposed in five rings concentric with the aperture axis. Fig. 4.9 shows the position of the ions when they cross the right side plan of the simulation box, 4 mm away of the PG. Without plasma, the distribution of the extracted NI is still rather circular, with some fluctuation caused by the magnetic fields and numerical noise. When the plasma is present, the distribution is visibly distorted. The number of rings in the extracted beam in this second case is lower than in the first case, even if the initial number of rings is the same. The screening of the extraction field by the plasma destroys the symmetry of the rings. We discuss in the next section the effect of the screening on the NI extraction.

4.7 NI Extraction

To study the efficiency of the screened potential to extract negative ions we integrate the trajectories of NI in the field obtained with the PIC simulation for given initial conditions. In these calculations NI are test particles, they do neither affect the plasma not the fields. This situation corresponds to the case of a low NI density.

In the previous section the extraction aperture have a cylindrical shape. Simulations made show that the extraction of NI created at the surface of the PG is greatly affected by the shape of the aperture. Because of this, in this section we use a conical aperture, similar to the real device [50, 37]. For all the calculation the diameter of the aperture is kept constant ($d_1=9$ mm, $d_2=14$ mm).

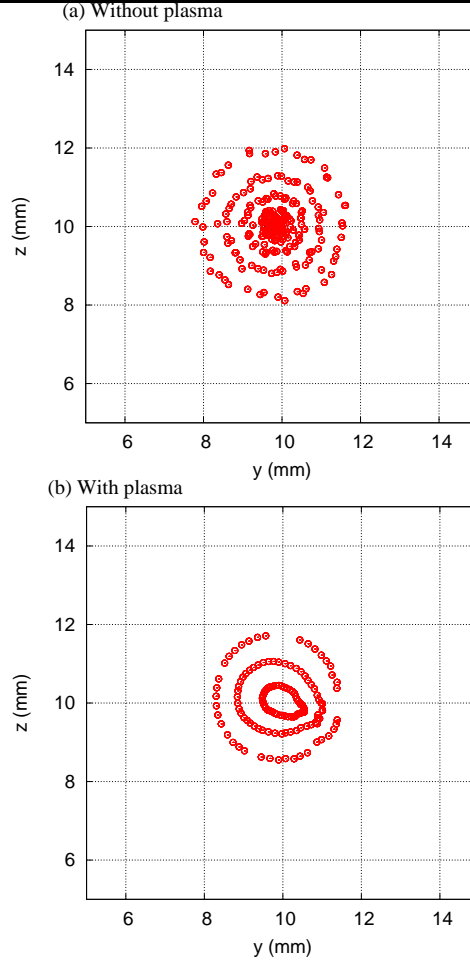


Figure 4.9: Negative ions distribution on the exit plane without (a) and with (b) plasma. Filter and deflecting magnetic fields are present in both simulations

4.7.1 Negative Ion Extraction from the Plasma Grid Wall

Fig. 4.10.a shows the trajectories of NI (as the test particles) created at the inner surface of the aperture - representing NI surface production 3.11.3, for the plasma without negative ions. Initial energy of the NI released from the wall is 1 eV. As it can be seen, all the particles are extracted. Negative ions created on the inner face of the PG are also totally extracted (Fig. 4.10.b). A detailed view of the potential distribution in the vicinity of the PG is shown in Fig. 4.11. The plasma pushes the potential lines close to the PG, creating an electric field perpendicular to the PG wall, i.e. in the x direction. This field accelerates negative ions towards the center of the chamber. The particles pass the maximum isopotential surface, close to $x = 16$ mm, where they start being accelerated in the opposite direction, to be finally driven through the aperture. The parametric study of the initial energy of NI leaving the plasma grid surface has performed. It was detected that from 0.5 to 2 eV all negative ion totally extracted

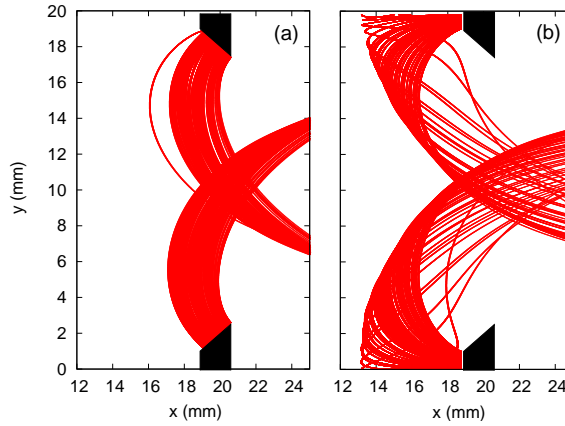


Figure 4.10: Trajectories of NI released from the aperture inner wall (a) and over the PG (b) - surface production. Initial energy 1 eV

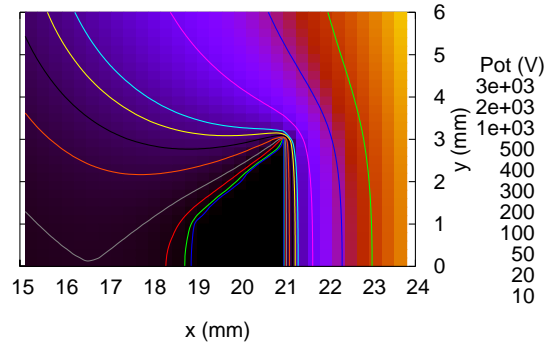


Figure 4.11: Zoom of the spatial distribution of electric potential close to the PG

4.7.2 Negative Ion Extraction from the Volume

Extraction of NI from volume is strongly affected by the plasma screening. Close to the extraction aperture (Fig. 4.12) all the particles are extracted. But the fraction of extracted NI drops quickly as particles are created farther from the PG. This can be seen in Fig. 4.13, that shows the fraction of extracted particles as a function of their initial position along x , with and without plasma. Negative ions are initially randomly distributed in the expansion chamber volume. In the case without plasma, the external potential is not screened and almost all the NI are extracted. Plasma screening reduces strongly the extraction field and, consequently, the extracted fraction. As it can be seen in Fig. 4.13, at 11 mm from the PG ($x = 8$ mm), less than 1% of NI created in the volume are extracted. The extraction efficiency starts dropping at $x \sim 14$ mm, that roughly corresponds to the position of the meniscus point farthest from the PG (Fig. 4.1). Therefore, the extraction from the plasma volume is significant only if the NI are present not far (~ 6 mm) from the meniscus. Otherwise, NI will remain trapped into

the plasma up to being neutralised. This result is in contradiction to results obtained in [115], where mean free paths have been shown for negative hydrogen ion in range from 0.1 to 0.7 m. However, due to the positive charge compensation in the plasma volume most of the negative ion will stay in the volume and not extracted.

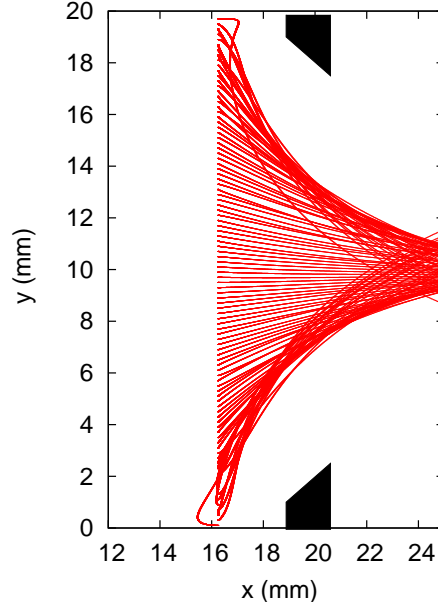


Figure 4.12: Trajectories of NI created in the volume, close to the aperture. Initial energy 1 eV

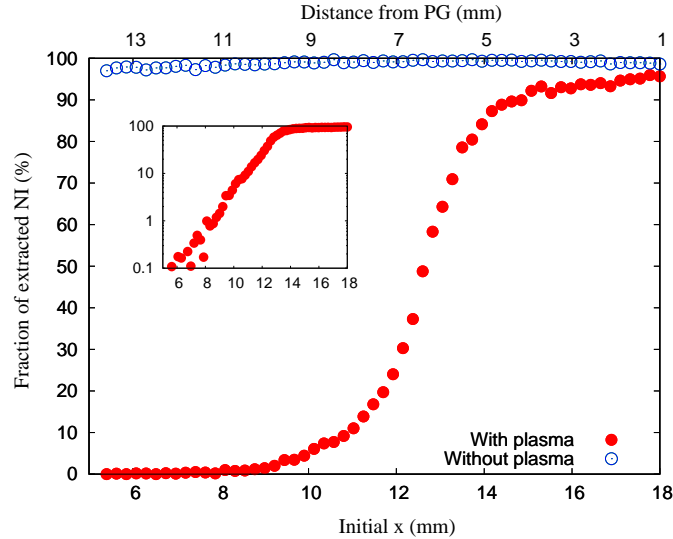


Figure 4.13: Fraction of extracted negative ions created in the volume as a function of the initial x position. The same data in semi log scale is shown in the inset

The results in collisionless plasma approximation were presented in this chapter in order to show the general system behavior in simplified conditions. However, the implementation in the code of a realistic kinetic model is a necessary step to bring quantitative

CHAPTER 4. RESULTS IN COLLISIONLESS APPROXIMATION

predictions of NI current. In particular, reliable data for the negative ion producing yields from the surface is critically needed. Therefore, collision part using Monte Carlo Collision approach has been successfully developed and implemented in the program. The next chapter will present the simulation results that are close to the real experiments, in collision approximation

Chapter 5

Results Including Plasma Kinetics

The previous chapter presents the first simulation results of the plasma behavior close to the extraction region of the NBI source system using simplified plasma. In order to attain more realistic results the kinetic module has been developed and implemented in ONIX. In the modified version of the program, negative ions are created in the simulation domain. The production of the negative ions in the volume has been self-consistently introduced by the electrons dissociative attachment to the Hydrogen molecule in high vibrational states. The NI production from the Cs covered plasma grid wall has been given by the constant flux of the randomly distributed negative ions. The most important negative ion destruction processes have been also implemented in the new version of the code.

According to all these modifications the potential distribution along the simulation domain has been calculated and presented in this chapter. The self-consistency of the positive ion meniscus formation is stressed by recalculating all the parameters including the collision processes. The contribution of the extracted negative ions current of ions born in the volume and at the different sides of the PG is shown. The maximum negative ion extracted current has been found with respect to the optimum emission rate of negative ion from the plasma grid wall. Beyond this optimum, a double layer builds-up by the negative ions charge density close to the grid aperture surface reducing thus the extraction probability, and therefore the extracted current. Finally, the parametric study of the extraction potential and magnetic field magnitudes on the extraction is also discussed.

5.1 General Behaviour

5.1.1 Self-consistency of the Meniscus Formation

The high positive potential applied between the plasma and the extraction grids accelerates the negative particles towards the calorimeter. Simultaneously it repels the positive ions back into the expansion chamber where they organize in a semi-spherical structure called meniscus. The self-consistent meniscus formation was already shown in the previous chapter for the case of an aperture with cylindrical shape. Fig. 5.1 shows the initial and quasi-steady state (at $\sim 0.3\mu s$) H^+ density distributions for an conical shape aperture [50]. Positive ions are pushed by the external potential towards the expansion chamber, forming the meniscus visible in the figure. The meniscus is placed farther from

the plasma grid than in the previous results. The distance from the PG is ~ 6 mm instead of ~ 4 mm in the cylindrical geometry. This is because the extraction field penetrate deeper inside the expansion chamber for the conical aperture, and thus positive ions are pushed farther from the grid.

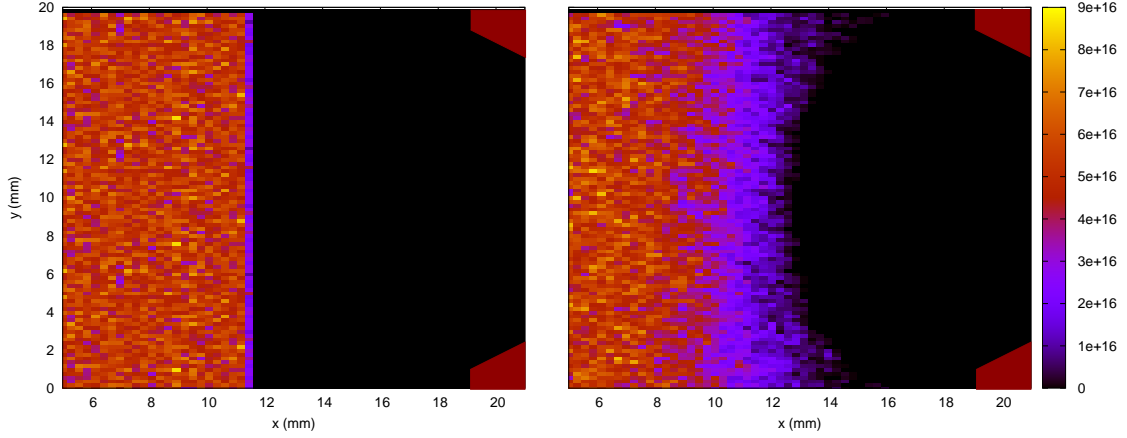


Figure 5.1: Spatial distribution (x,y) of positive ion density in the mid-plane ($z = 10$ mm) of the simulation box at the beginning of the simulation ($t = 0$,left) and close to the steady-state ($t = 0.3 \mu\text{s}$, right)

5.1.2 Potential Calculation

The spatial distribution (x,y) of electrostatic potential at the beginning of the simulation and after $0.3\mu\text{s}$ are shown in Fig. 5.2. At $t=0$, the external electric field deeply penetrates into the expansion chamber. However, once that plasma screening occurs, the iso-potential lines are pushed towards the PG. The neutrality of the system is maintained in the initial plasma region ($0 \leq x \leq 12\text{mm}$). The potential is constant in this region, meaning that electric field vanishes and $\vec{E} \times \vec{B}$ drifts are suppressed.

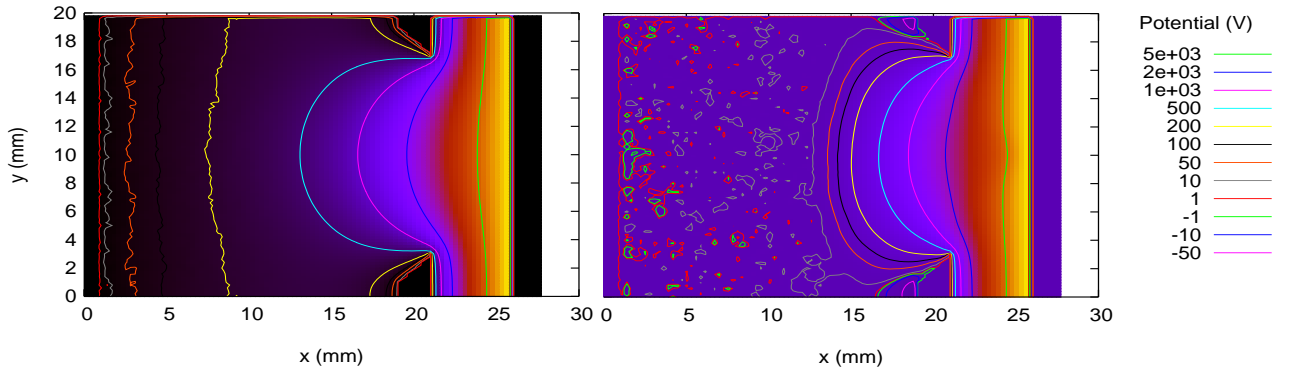


Figure 5.2: Spatial potential distribution for the same situation as in Fig. 5.1

5.2 Evolution of the Extracted Electron and Negative Ion Current

At the beginning of the calculations negative ions are not present into the plasma volume. They are created *via* three different processes: (i) electron dissociative attachment to the vibrationally excited molecules $H_2(v)$ in the volume, (ii) interaction of the positive ion H^+ with the aperture wall and (iii) collisions of the neutral gas H with aperture wall. Fig. 5.3 shows the time evolution of the NI extracted current for each production channel induced by different atomic processes together with the co-extracted electron current. All currents are evaluated at the exit plane (the right side of the simulation domain), $4mm$ far from the PG. One can see first that the electron current grows very fast, because the extraction potential is not screened at the beginning. The growing of the extracted electron current continues up to $t=0.15\mu s$. At this time, the plasma screening of the extraction potential starts being efficient, thus reducing the fraction of the extracted electrons. After this transitory phase, electron and the NI currents stabilize, and the system reaches a quasi-steady state. The achievement of the quasi-steady state is also visible from the potential evolution. For $t > 0.3\mu s$, the local value of the potential presents fluctuations smaller than 1%.

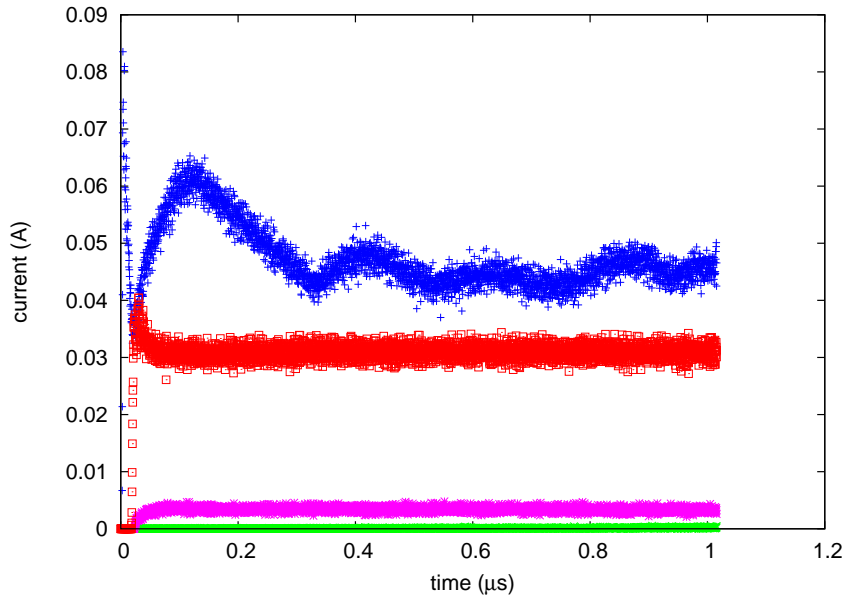


Figure 5.3: Time evolution of the extracted electron and negative ion currents. Blue line(+) - co-extracted electron current. Red line (□)- NI extracted current from the PG inner aperture surface produced by neutrals impact. Pink line (*)- NI extracted current from the PG outer surface produced by neutrals impact. Green line (·) - NI extracted current from the volume, produced *via* electron dissociative attachment collisions

Because of the low density of the $H_2(v)$ in high vibrational states (due to the low pressure in the source $\sim 0.3Pa$), it is not possible to produce a large amount of NI in the volume. Moreover, NI destruction by electron stripping, significant at electron energies of few eV, and by mutual neutralization will destroy most of the negative ions produced in the expansion chamber before being extracted. On the other hand, the efficient screening

of the extraction field by the plasma reduces the region from where NI can be extracted. Therefore the extracted NI current coming from the volume created ions (green line Fig. 5.3) is much smaller than one extracted from the PG surface (red and pink lines Fig. 5.3). This result agrees with the strong reduction of NI current in experiments performed in the Cs-free operation regime [50].

The dominant process of NI surface creation is the collision of neutral molecules with the PG wall. In our simulations the high external potential pushes most of the positive ions far from the PG wall. The extracted NI current coming from interaction of positive ions with PG surface is therefore very low. However the positive ion-neutral conversion is not taken into account in the code. It was assumed that negative ion flux from the PG includes all the mechanisms of the NI production by neutral impact. In this simulation a given value for the emission rate of negative ions from the PG wall has been used, that corresponds to the case of optimum extraction (see next section).

One can distinguish between the contributions to the extracted current of NI originating from the outer surface of the PG (pink line Fig. 5.3) and from its inner surface (red line Fig. 5.3). Due to the double layer formation close to the PG, discussed below, and of the geometry of the screened electric field in this region, the contribution of NI coming from the outer surface of the PG is about 10 times smaller than the one of NI coming from the inner surface of the aperture.

The asymptotic value of the whole extracted current through one aperture obtained in the simulation ($I_{NI_{tot}} = 0.036A$, Fig. 5.3) is in good agreement with experimental results obtained in the BATMAN test bed machine at IPP Garching (1.3–1.6A from 44 apertures extraction system) [50, 51]. The aperture geometry and the magnetic field structures used in the simulations are taken from those used for test facility. A good agreement is also obtained for the electron/NI currents ratio (~ 1.15), close to the experimental value. The NI current density was found equal to $j_{NI} = 234 \text{ A/m}^2$, that also matches the experimental results. In both cases the extracted current density is close to ITER specifications: $j_{NI} = 280 \text{ A/m}^2$, $I_e/I_{NI} = 1$ [16]. The numerical predicted co-extracted electron current is slightly larger than the negative ion one. However we have to take into account that this current, calculated 4 mm after the PG, is much larger than the real electron current entering the accelerator. Most of the electrons cross the right side of the simulation box with very large transverse velocity due to the deflecting field, and they will hit the extraction grid wall or the vessel.

5.3 Saturation of Negative Ion Current

In the previous section we enacted that the extraction of negative ions from the volume is not efficient and its contribution the total extracted NI current is rather small in comparison with that of ions created on the plasma grid surface. Experimental evidence of this fact has been reported in several works [50, 52, 61]. However, the present knowledge of the physics of the NI production by interaction of neutral molecules with a Cs covered surface is limited. Lacking of reliable data, we performed simulations for different values of NI emission rate from the PG surface. Each time iteration step the negative ions are randomly launched from the aperture cone wall and from the flat surface wall of the PG with 1 eV initial velocity. Fig. 5.4 shows the extracted NI current *versus* the negative

ion yield at the surface. The current reaches a maximum at the rate of $2000 A/m^2$, and further subsequent increasing of negative ions production rate results in the smaller NI current. The explanation why the NI extracted current decrease when the higher emission rate is used will be given in the next section.

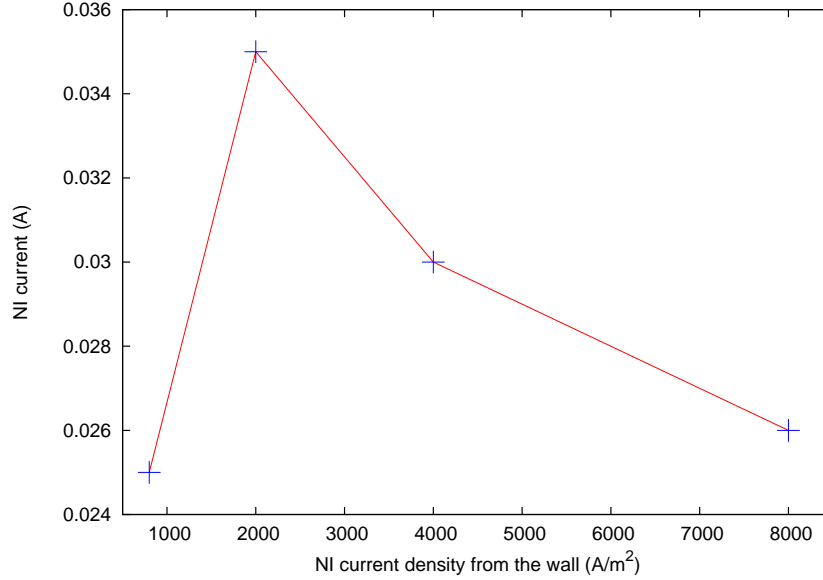


Figure 5.4: Extracted NI current by the surface production mechanism for different emission rates

5.4 Limitation of the Negative Ion Extraction

The reason of such limitation is the formation of a double layer [116, 117, 118], created by the negative ions in the vicinity of the aperture wall. Fig. 5.5 (a) shows the spatial potential distribution close to the PG in the $x - y$ mid-plane. The aperture is located between $x = 19$ mm and $x = 21$ mm. It is clearly visible in this figure the strong double layer behind the plasma grid at $x = 18.5$ mm for NI emission rate of $2000 A/m^2$. Electrons and negative ions flux released from the plasma grid wall is higher than their values into the sheath. Thus, negative particles accumulate in the vicinity to the PG surface creating the double layer structure. In such double layer, electrons and negative ions coming from the wall are decelerated and reflected back towards the surface due to the inversion of the electric field there if their energy is lower than the double layer potential well. Reflected negative ions striking the wall are destroyed, i.e. their extraction is not longer possible. The depth of the double layer is maximum on the inner side of the aperture (source side) (Fig. 5.5 (a)). Fig. 5.5 (b) shows the electric potential transverse profile at three longitudinal positions inside the PG. The curve "A" corresponds to $x = 19.04$ mm, close to the beginning of the aperture (source side). The curve "B" is in the middle of the cone ($x = 20.16$ mm). The curve "C" corresponds to $x = 20.72$ mm, at the end of the aperture. Note that the curves begin at different abscissae because the aperture is conical. As it can be seen, the depth of the double layer is maximum on the inner side of the aperture (curve "A"). The depth of the potential well decreases from $V_A \approx 30$ V at the curve "A"

to $V_C \approx 10$ V for the "C". This reduction is due to the grow of the extracting field with x . For a given value of x , the external extracting field will eventually become able to balance the negative charge pile-up, reducing the depth of the double layer. For $x > 20.5$ mm, the double layer is too weak to reflect negative ions, and most of them are extracted.

For lower emission rates, the double layer depth is less important and it is limited to a smaller region of the plasma grid. Thus, more particles will be able to cross the negative sheath being finally extracted. The reason of such double layer formation close to the plasma grid aperture is not enough of the positive ion flux from the source in this region that will be able to compensate the negative charge of the wall created NI [119].

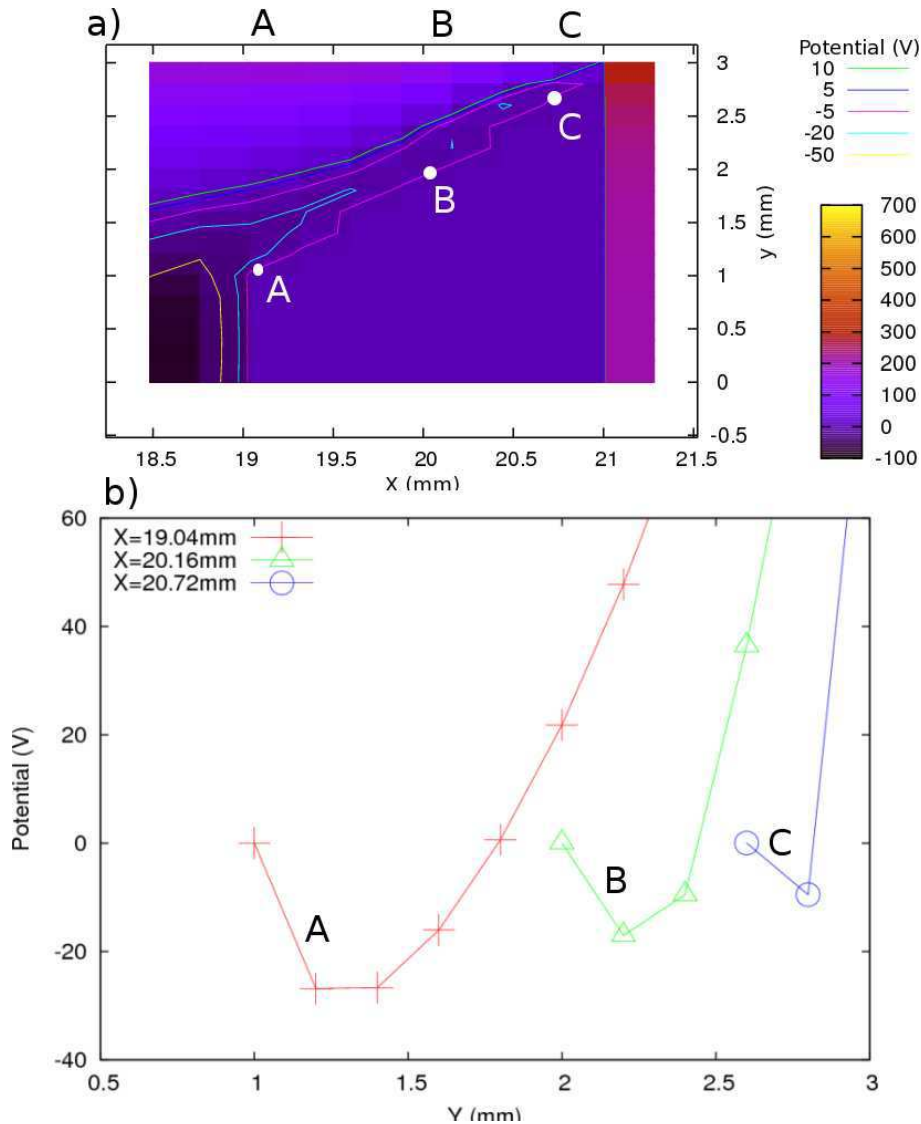


Figure 5.5: (a) Spatial distribution of the electric potential close to the PG (PG is located between $x = 19$ mm and $x = 21$ mm). The optimal emission rate from the PG was used. (b) transverse profile of the electric potential at three different location along the aperture: (A) corresponds to $x=19.04$ mm, (B) $x=20.16$ mm, (C) $x=20.72$ mm

The presence of the double layer reduces the “effective surface” of PG from where produced negative ion will be able to be extracted. This effective area can be inferred from

Fig. 5.6, that shows the number of extracted ions as a function of the axial coordinate x corresponding to the NI born position (along PG surface), for several emission rates. For an emission rate of 800 A/m^2 , particles are extracted from almost the whole range of x values, that is, the effective area is equal to the area of the aperture wall. For a rate of 2000 A/m^2 , the emission region is strongly reduced, but the integrated number of extracted particles is larger than for 800 A/m^2 , because of the larger rate. For higher rates, the area decreases faster than the rate grows, and the resulting total number of extracted particles becomes smaller (this is also visible in Fig. 5.4). Note that in the optimum case (2000 A/m^2), only particles created beyond $x = 20.5 \text{ mm}$ are extracted, i.e. the “effective extraction” area covers only a small part of the PG aperture surface.

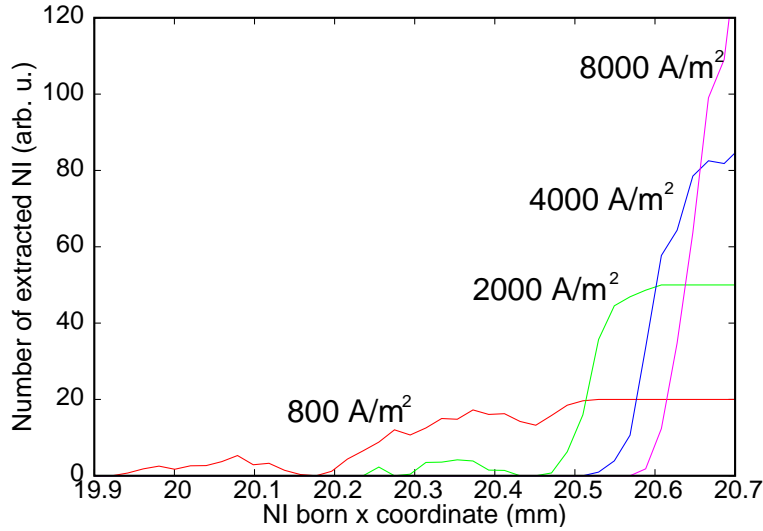


Figure 5.6: Number of extracted NI as a function of the born axial position (along PG surface) for different emission rates. The plasma grid goes from $x = 19 \text{ mm}$ and $x = 21 \text{ mm}$

5.5 Effect of the External Positive Potential on the NI Extraction

We present in this section the effect of the extraction potential on the total extracted NI current. Simulations with potential of 4 kV , 6 kV , 10 kV and 20 kV were performed with the optimum emission rate of NI from the surfaces, discussed above. In order to benchmark our results with experimental data, extracted current was calculated from 44 apertures as in configuration of the BATMAN test bed facility [50]. Fig. 5.7 shows the total extracted NI current *versus* external potential applied in the system. Up to 20 kV the NI current grows with the applied potential. In the present design of the NI extractor for ITER NBI, the extraction potential is $V \sim 10 \text{ kV}$. The calculated NI current for this potential is about 0.036 A , that satisfied ITER requirements of 40 A current for 1280 apertures assuming that the simulated aperture is representative for all the others. However, higher extracted currents can be obtained by raising the external potential above 10 kV . However, the co-extracted electron current also increases with

higher potential value. Experiments performed in Garching show a similar trend ([50] - Fig. 23). The simulation results are in a good quantitative agreement with these experiments, showing the validity of our simulation model.

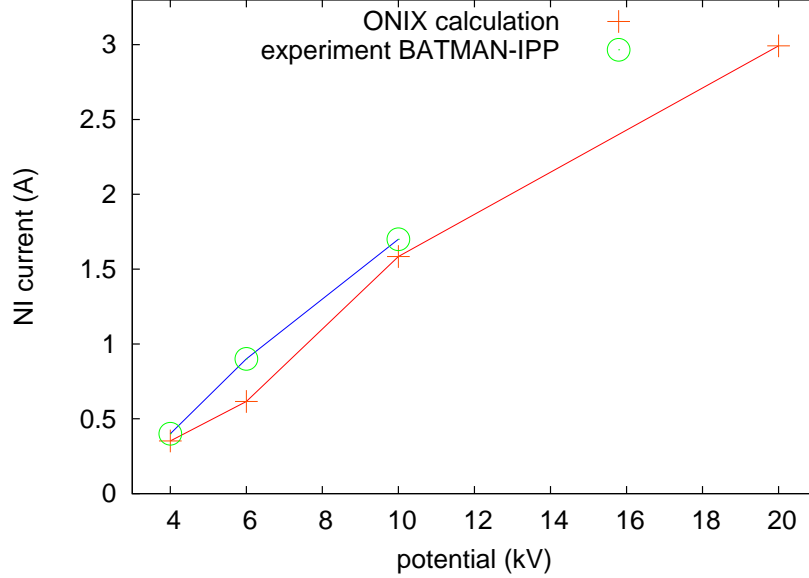


Figure 5.7: Total extracted NI current vs. positive external potential. Red line - ONIX calculations, blue line - experimental BATMAN results [58]

As it was mentioned above, a significant number of electrons are co-extracted with negative ions. The reduction of the electron co-extracted current is an important issue for the NBI operation. Fig. 5.8 shows the ratio of the negative ion electron extracted current for different extraction potentials. For lower potentials (4 kV and 6 kV), the NI current is dominant (6 and 1.5 times higher than electron one respectively). This is in contradiction with the already mentioned experimental results [50], and requires further studies of the method implemented in the code to reinject electrons and ions, that could affect the estimated value of the total extracted electron current. But, we have to note here that the electron current obtained from ONIX calculations has been measured at the distance 4 mm from the PG could be different from the experimental electron current measured at the EG. However, for the potentials $V \geq 10$ kV the NI/electrons ratio remains around 1, in agreement with experimental results. In addition, this value, fulfills ITER requirements as well [16].

5.6 Effect of the Magnetic Field on the Electron Extraction

A relatively complex magnetic field topology is used in the negative ion source system in order to filter the electrons. This magnetic field should be high enough to trap plasma electrons, but not as high to disturb the negative ions trajectories. All previous simulations were done with the magnetic field distribution that is shown in Fig. 3.12, hereafter

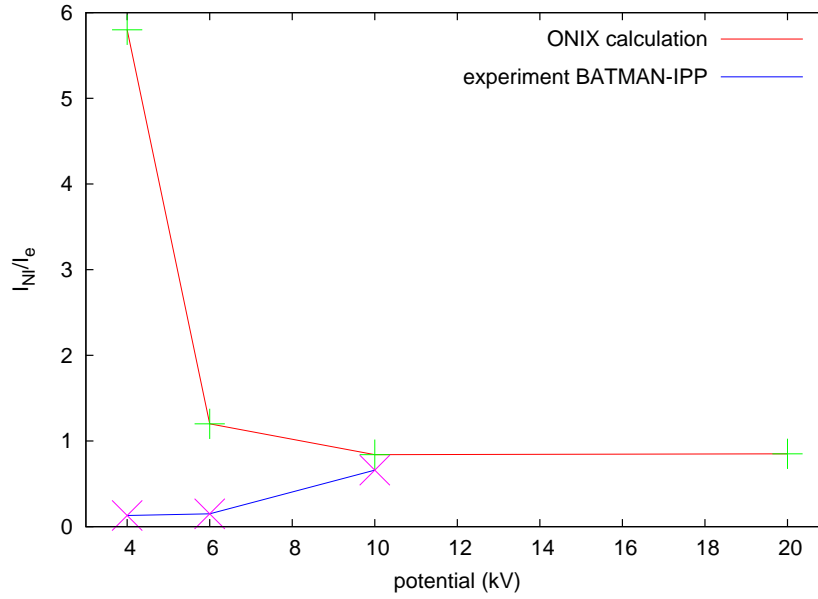


Figure 5.8: Negative ion current/electron current ratio vs. positive external potential. Red line - ONIX calculations, blue line - experimental BATMAN results [58]

named the standard magnetic configuration. In this section we multiply the filter and the deflecting fields by the scalars γ_f and γ_d respectively.

5.6.1 Study of the Deflecting Field Effect

The electron and negative ions extracted currents for $\gamma_f = \gamma_d = 1, 1.5$ and 2 are shown in Fig. 5.9. In the standard configuration the electron current is slightly larger than the negative ion one. Remember that this current is calculated in a plane 4 mm far from the PG, and the presence of the deflecting magnetic field close to the EG results in a lower current farther this plane. Configuration with the magnetic fields multiplied by a factor 1.5 leads to a more efficient electrons trapping, decreasing ~ 8 times the electron current. For the strongest configuration tested ($\gamma_f = \gamma_d = 2$), the electron current almost vanishes even at the distance of 4 mm from the PG. The increment of the field strength does not affect visibly the NI beam, because of their higher mass. However, the negative ion current is slightly smaller for the stronger magnetic field configurations. The ratio electron/negative ion currents takes much smaller value for higher magnetic field configurations. The electron current suppression in these simulation causing mostly by the high configuration of the deflection magnetic field, while the high configuration of the filter magnetic field decreases electron current by 10 – 25%.

5.6.2 Study of the Filter Field Effect

For technical reasons, it is difficult to increase the strength of the deflecting field. The permanent magnets that create this field are embedded inside the extraction grid, that has a limited size and that includes a water cooling system to evacuate the heat load. Hence, we made simulations keeping the standard value of the deflecting field (shown in

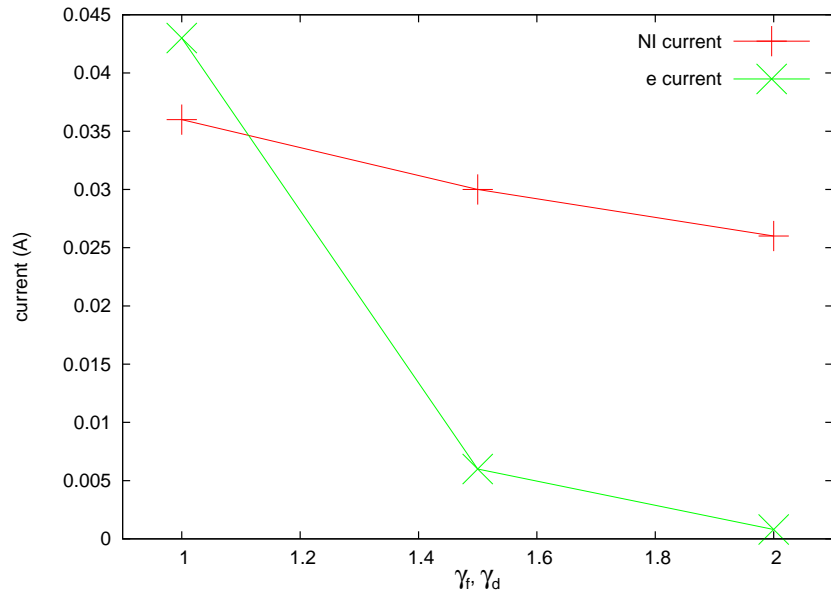


Figure 5.9: Electron (\times) and negative ion ($+$) currents vs magnetic fields strength

Fig. 3.12, with $\gamma_d = 1$) and changing only the strength of the filter one (γ_f). Fig. 5.10 shows the co-extracted electron current for different values of the filter magnetic field strength. If this field is suppressed, the electron current passing through one aperture rises up to 0.07 A, about 1.5 times bigger than in the standard configuration. For larger values of the field strength, the electron current decreases. However, the electron current continues to be remains significant (0.03 A) even for a field twice stronger.

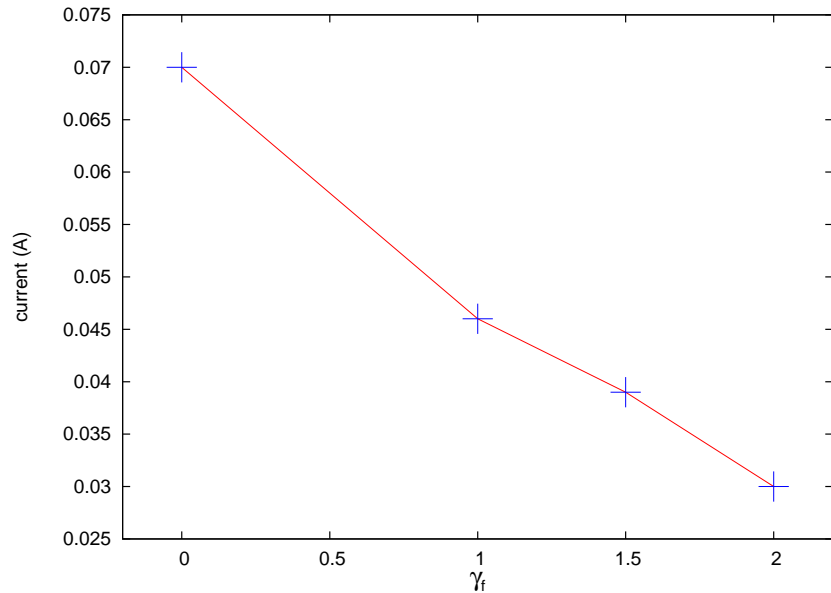


Figure 5.10: Electron current vs. magnetic filter field strength γ_f

5.6.3 Halo of the Negative Ion Beam

In the previous chapter was demonstrated how the plasma screening effect and $\vec{E} \times \vec{B}$ drift of the magnetized electrons (in the sheath region) disturb the symmetry of the model. In the next studies we want to show the role of the magnetic fields on the trajectories of the negative ions produced at the plasma grid surface. In this simulation the NI are test particles as in the Sec. 5.4 (Fig. 5.6). Fig. 5.11 shows the intensity of the extracted NI at the exit plane a) with and b) without magnetic fields. The standard distribution of the magnetic fields (Fig. 3.12) could not magnetized NI, however it slightly disturbs their trajectories and changes the angle of the extracted NI beam. In the Fig. 5.11 a) the center of the beam is shifted in z (vertical) direction compare to the Fig. 5.11 b) - where the center of the beam is located exactly in the middle of the simulation box ($y = 10$ mm, $z = 10$ mm). The difference between two beams is also visible at the left bottom from the centers of the figures, thus the magnetic fields affect the NI trajectories and slightly diverge center of the beam. The asymmetry of the beam is present on both figures (due to the plasma screening effect) that also prove the necessity of the 3D model for such simulations.

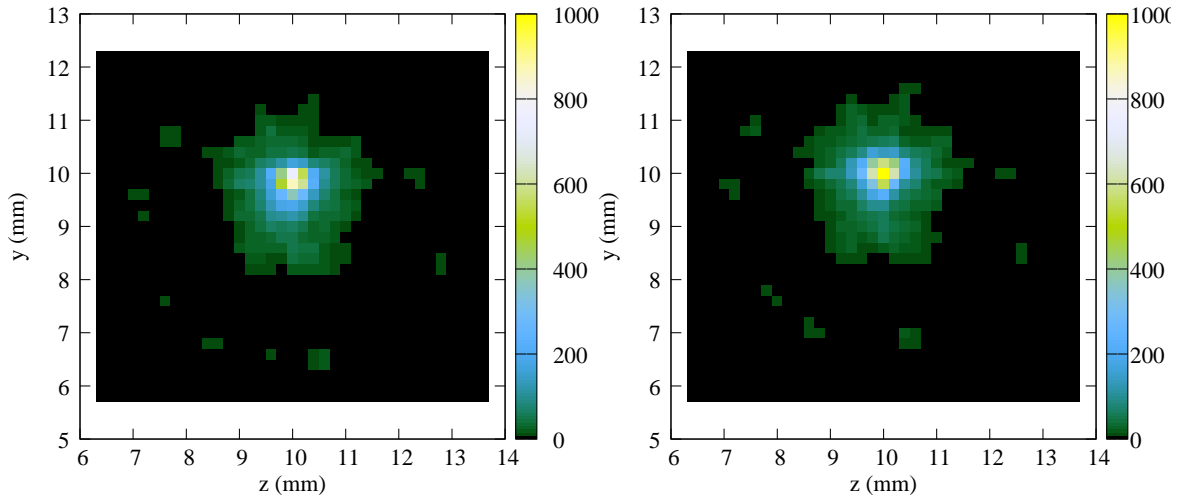


Figure 5.11: Intensity of the extracted NI at the exit plane ($y - z$) with a) and without b) magnetic fields

5.7 Suppression of Electron Current by Production of NI From PG Wall

The injection of the Cs atoms in the plasma source system increases the extracted negative ion current. Meanwhile, it causes the decreasing of co-extracted electron current. This phenomenon has been detected in many experiments, for instance in [50] during the discharges with evaporated Cs atoms and Cs free regime.

In order to understand the reason of such electron current suppression, two simulations have been conducted. First one does not include the emission of the negative ions from the plasma grid surface, i.e. corresponds to the Cs free experiments, while the second run has

been performed with the production of NI at the PG wall – experimental situation with evaporated *Cs* gas. The electron current of 0.0062 A has been measured in the simulation without negative ions, when in the case with the injection of *Cs* atoms electron current decreases by ~ 30 percent (in agreement with experimental currents behavior) and takes value of 0.0042 A.

The explanation of this phenomenon is given in the Fig. 5.12, where the potential distribution is shown from two simulations: a) – without, b) – with NI. The flux of negative ions from the plasma grid surface changes the potential isolines in vicinity to the aperture. In the case without NI the external potential penetrates deeper inside the expansion chamber, thus repulses the meniscus depthward. Therefore, the electrons retention time in the volume grows causing the depletion of the extracted electron current.

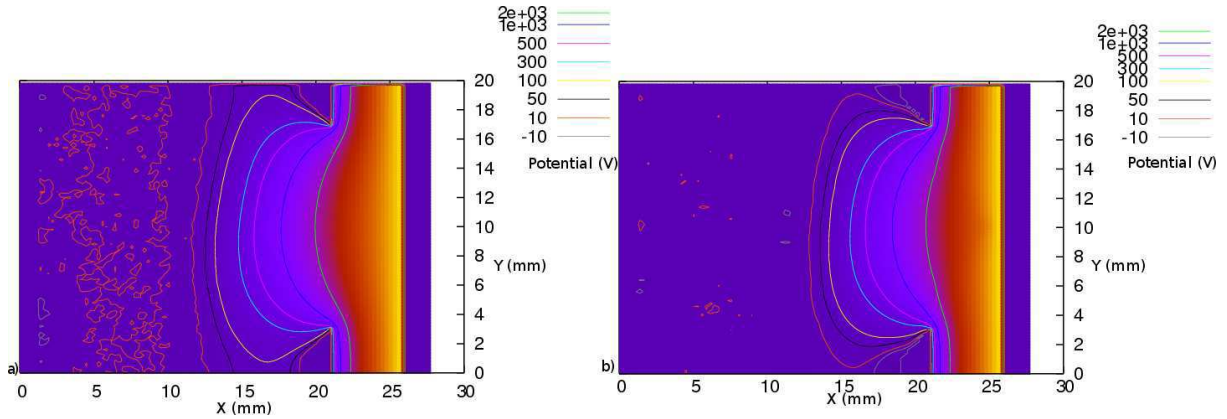


Figure 5.12: The potential distribution along the simulation volume in two cases: a) – without negative ions production from the PG surface (corresponds to *Cs* free experimental regime) and b) with NI emitted from the PG wall

Chapter 6

Conclusions and Future Work

This thesis has described the development and the implementation of full 3 dimensional PIC-MCC model for simulation of the negative ion extraction from the NBI plasma source system for future thermonuclear experimental reactor ITER. The ONIX code has been parallelized to distribute memory between multi-CPU computers to reduce the real computation time. The primary results from the preceding chapters are summarized here and possibilities for future work are presented.

6.1 Unique Numerical Tool

The developed program is the first 3D PIC model for NI extraction from hydrogen plasma source that uses realistic description of the geometry of the grids and externally applied fields. In order to accurately calculate the potential distribution in the vicinity to the plasma grid orifice the special technique of the boundaries correction was implemented in the Poisson's solver routine. Our code is able to deal with complex boundaries geometries and thus with the boundaries lying between PIC nodes. It gives a wide flexibility to describe complex simulation geometries as it is in the case of the plasma grid aperture.

The kinetic module in the code includes the relevant volume reactions occurring in the ICP type of plasma source. The plasma parameters are all taken from experimental previous works and they are defined in the International System giving thus a large flexibility of the code performance possible to be extended to other topics of plasma physics.

The ONIX program is fully parallelized using domain and particles decomposition approach. The benefit from the parallelization procedure is obvious; the elapsed time necessary for one complete program run is reduced ~ 15 times on 20 CPU with respect to one sequential code run and it takes about 4 – 5 days.

6.2 Summary of Results

The following summarizes the main results obtained by running the ONIX program:

- The electron, positive and negative ions transport together with plasma properties have been studied in the extraction region of negative ion plasma source of

ITER NBI. It is shown the "meniscus" formation corresponding to the positive ion arrangement in the front of the PG aperture.

- The intrinsic three-dimensional nature of the problem induced by the presence of the filtering magnetic fields is visible in the plasma spatial properties as well as in the screened potential map. Its asymmetry affects strongly the geometric properties of the extracted negative ion beam breaking its circular symmetry.
- It has been shown that the plasma screening of the external extraction field is very effective, producing a deleterious effect over the extraction capability of this device. The extraction of negative ions created in the volume is actually reduced to a very small region around each extraction hole. As expected, the better extraction efficiency corresponds to negative ions created in the meniscus region, specially over the plasma grid surface. However, the extraction there appears to be strongly dependent with the details of the aperture geometry.
- The simulations have shown that the main contribution to the extracted negative ion current comes from ions created in the inner surface of the plasma grid (roughly 90% of the extracted current). The contribution of the volume created negative ions is very small.
- The code is able to simulate the co-extracted electron current, founded value is close to the NI one, in agreement with experimental results.
- An optimum of the extracted NI current with respect to the rate of negative ion emission from the plasma grid wall has been found. For lower or larger emission rates than this optimum, the extracted NI current decreases.
- The NI current limitation is caused by the formation of a negative sheath (double layer) close to the plasma grid surface. For larger emission rates, the negative charge close to this surface produces the inversion of the electric field, pushing back the negative ions to the surface, avoiding thus their extraction.
- Parametric studies on the value of the extraction potential and on the magnetic field strength were performed. It has been found that the NI current can be enhanced by raising the extraction potential. The use of stronger magnetic field does not affect the negative ion current, whereas it can reduce significantly the co-extracted electron current. Larger negative ion current with smaller electron/NI current ratio can be obtained by increasing both values: of the extraction potential and the magnetic fields strength.
- The performance predicted for the extractor fulfills the ITER NBI requirements, in terms of extracted NI and electron currents and current densities for the hydrogen discharge. Such estimation has been done by the multiplication of the total current obtained from single simulated aperture by the number of apertures in ITER NBI configuration (1280). However, in large source the extracted current is not homogeneous and prediction from ONIX code could be different from experimental results.

6.3 Future Plans

Several plasma simulations had been successfully conducted by using the ONIX code. However, there are still open challenging tasks concerning the production and extraction of the negative ions, which can be addressed in the future. Moreover, new ways are opened by the large set of possibilities shown from the simulations presented in this thesis. Some items that require future investigation include:

- *Detailed analysis of the double layer structure.* The formation of the double layer has been detected and described in this thesis. However, the further optimization of the negative ion extraction requires to know the contribution of all negative particles involved in this double layer formation. Among them the electrons that come from the expansion chamber, the electrons secondary emitted from the plasma grid, negative ions created in the volume and negative ions produced at the PG surface.
- *Theory of the fast negative ions.* The limitation of the negative ion current has been presented in the manuscript. It had been shown that extracted NI current from the PG wall saturates at a certain emission rate and further increasing of the NI yield will be the result of a smaller extracted current due to the reverse negative sheath close to the PG. However the effect of the initial NI velocity has not been studied. More energetic negative ions could overcome the negative sheath and than could be extracted from the system.
- *Suppression of the co-extracted electron current.* One of the most critical issues of the NBI plasma source system is the trapping of the electron beam. More simulations with a different position and geometry of the filter and deflecting magnetic fields must be done in order to find the optimum configuration at which the extracted electron current attains its minimum.
- *Study of the aperture geometry.* The shape of the extraction and plasma grid apertures has a significant effect on the extracted negative ion and electron currents. The potential distribution in vicinity to the plasma grid changes drastically when the form of the aperture is modified. In this thesis only rough comparison between conical and cylindrical shapes has been performed. The future study should include the simulation with different diameters and bands of the PG aperture. The double chamfered aperture shape, as in the ITER specifications, must be also considered.
- *Deuterium simulations.* The NBI system for the future tokamak ITER should operate with both Hydrogen and Deuterium ions. The most of the results presented in the thesis have been obtained by performing simulations with Hydrogen plasma. The particles and plasma behavior have to be also studied when Deuterium ions are extracted.
- *Complete composition of the experimental results.* The initial plasma parameters in the simulations have been taken from the experimental data. However, some quantities are not well described when the parametric study was performed. For instance,

the study of influence of the Cs evaporation rate on the co-extracted electron current. Cs induces the changing of the electron density and temperature. All these quantities must be adjusted for each independent simulation in order to obtain the full description of the system behavior. The current installation of several new diagnostics at the BATMAN experimental machine allows to measure simultaneously for first time all plasma parameters. The complete data set of the experimental results will give the possibility to perform the more realistic calculations.

Although ONIX code is capable performing wide variety of the plasma situations, some program parts require additional work. The list of the possible improvements for the ONIX code includes:

- *Self consistent NI production from the PG wall.* Implementation of the self consistent NI production from the Cs covered PG surface. In the current version of the ONIX code, negative ions created at the plasma grid wall represented as the given arbitrary flux of the NI. Future version of the program must include the dynamics of the energetic neutral atoms responsible for the birth of NI and self-consistent negative ion production at the PG surface.
- *Extension of the modeling region.* At present, simulation domain includes only one aperture from the plasma grid. The introduction of the second aperture is necessary in order to simulate complete distribution of the magnetic fields that play decisive role of the electron beam suppression. The deflected magnetic field has different direction between two neighboring orifice, thus full path of the electrons dynamic will be detected, when the second aperture will be included in the simulation model.
- *New mechanism of the plasma formation.* The current method that is used to build-up and to keep neutral simulated plasma is forcing the system by reinjection of eliminated particles in the region where the initial plasma was placed. Especially the system suffers when new particles are injected close to the plasma grid. Two other methods (the particles flux and the neutral plane) of plasma constructing have been also tested, but they had even more artificial influence on the system then reinjection procedure. Therefore, the new mechanism of the plasma formation should be found and implemented in the code in order to avoid numerical artefacts.

Bibliography

- [1] J. Ongena and G. Van Oost "Energy for Future Centuries - Prospects for Fusion Power as a Future Energy Source", *Transactions of Fusion Science and Technology* **49**, 3-15 (2006)
- [2] H.A. Bethe, "Energy Production in Stars", *Phys. Rev.* **55**, 434 (1938)
- [3] Stefano Atzeni, Jurgen Meyer-Ter-Vehn "The Physics of Inertial Fusion", *Oxford Science Publication*, book, (2004)
- [4] B.H. Duane, "Fusion cross-section theory", in *Annual Report on CTR Technology* Rep. BNWL-1685 (1972)
- [5] E. Bretscher and A.P. French, "Low Energy Cross Section of the D-T Reaction and Angular Distribution of the Alpha-Particles Emitted", *Phys. Rev.* **75**, 8 (1949)
- [6] A. Peres, "Fusion cross sections and thermonuclear reaction rates", *J. Appl. Phys.* **50**, 5569 (1979)
- [7] R.L. Hirsch, "Inertial Electrostatic Confinement of Ionized Fusion Gases", *J. Appl. Phys.* **38**, 4522 (1967)
- [8] J.A. Maniscalco, "Inertial Confinement Fusion", *Annual Reviews* **5**, 33-60 (1980)
- [9] B. Lehnert, "On the confinement of charged particles in a magnetic field", *J. Nucl. Energy, Part C Plasma Phys.* **1**, 40 (1959)
- [10] T. Ohkawa, "Multipole magnetic field configurations for stable plasma confinement", *IL Nuovo Cimento Series* **22**, 784-799 (1961)
- [11] V.P. Smirnov, "Tokamak foundation in USSR/Russia 1950–1990", *Nucl. Fusion* **50**, 014003 (2010)
- [12] M.G. Haines, "The Joule Heating of a Stable Pinched Plasma", *Proc. Phys. Soc.* **76**, 250 (1960)
- [13] J.A. Hoekzema, "Electron cyclotron waves", *Transactions of Fusion Science and Technology* **41**, 191 (2002)
- [14] Sante Cirant, "Overview of electron cyclotron heating and electron cyclotron current drive launcher development in magnetic fusion devices", *Fusion Scien. and Techn.* **53** (2008)

BIBLIOGRAPHY

- [15] Andrew Seltzman and John-Patrick Floyd II, "Plasma Waves, Heating and Current Drive", *NRE6102 textbook Stacey, Fusion Plasma Physics* (2006)
- [16] R. Hemsworth *et al*, "Status of the ITER heating neutral beam system", *Nucl. Fusion* **49**, 045006 (2009)
- [17] J.R. Gilleland *et al*, "ITER: Concept definition", *Nucl. Fusion* **29**, 1191 (1989)
- [18] R. Aymar, "Overview of ITER FEAT - The future international burning plasma experiment", *Nucl. Fusion* **41**, 1301 (2001)
- [19] N. Holtkamp, "An overview of the ITER project", *Fusion Engineering and Design* **82**, 427–434 (2007)
- [20] N. Holtkamp, "The status of the ITER design", *Fusion Engineering and Design* **84**, 98–105 (2009)
- [21] ITER Joint Central Team and Home Teams, "Review of the ITER Technology R&D", *Submitted to the Fusion Engineering and Design* http://www.naka.jaea.go.jp/ITER/official-J/Fusion_Engineering_and_Design/1-2_Design_Overview.pdf
- [22] J. Pamela *et al*, "Overview of JET results", *Nucl. Fusion* **43**, 1540 (2003)
- [23] J. Jacquinet *et al*, "Steady-state operation of tokamaks: key experiments, integrated modelling and technology developments on Tore Supra", *Nucl. Fusion* **45**, S118 (2005)
- [24] Presented by the ITER Director, "Summary of the ITER Final Design Report", *G A0 FDR 4 01-06-28 R 0.2*, http://fire.pppl.gov/iter_summary_FDR2001.pdf, (2001)
- [25] H.P.L. de Esch, *et al*, "The optimization of neutral beams for ignition and burn control on next-step reactors", *Fusion Engineering and Design* **26**, 589-604 (1995)
- [26] P.S. Krstic, D.R. Schultz, IAEA-APID-8 (1998)
- [27] T. Inoue, *et al*, "Design of neutral beam system for ITER-FEAT", *Fusion Engineering and Design* **56-57**, 517–521 (2001)
- [28] T. Oikawa *et al*, "Benchmarking of neutral beam current drive codes as a basis for the integrated modeling for ITER", *Proc. 22nd Int. Conf. on Fusion Energy*, Vienna,2008, IAEA, <http://www-naweb.iaea.org/napc/physics/FEC/FEC2008/html/index.htm>
- [29] B. Schunke *et al*, "Status of the Negative Ion Based Heating and Diagnostic Neutral Beam for ITER", *1st International Symposium on Negative Ions, Beams and Sources*, Aix-en-Provence, AIP conference proceedings **1097** 480 (2009)
- [30] Yasuhiko Takeiri, "Negative ion source development for fusion application", *Review of Scientific Instruments*, **81**, 02B114, (2010)

BIBLIOGRAPHY

- [31] L. Schiesko *et al*, "Investigation of the plasma parameters and homogeneity on a negative ion source for fusion", 30th *ICPIG conference*, Belfast, UK
- [32] Presented by the ITER Director, "ITER EDA Final Design Report, ITER technical basis, Plant Description Document", *G A0 FDR 1 01-07-13 R1.0, IAEA EDA documentation 24*, www-pub.iaea.org/MTCD/publications/PDF/ITER-EDA-DS-23.pdf, (2002)
- [33] T. Inoue *et al*, "1 MeV, ampere class accelerator R&D for ITER", *Nucl. Fusion* **46**, S379-385 (2006)
- [34] H.P.L. de Esch, *et al*, *Fusion Engineering and Design* **73**, 329 (2005)
- [35] G. Fubiani, *et al*, "Modeling of the secondary emission processes in the negative ion based electrostatic accelerator of the international thermonuclear experimental reactor", *Phys. Rev. Special Top* **11** 014202 (2008)
- [36] M. Taniguchi *et al*, "Development of 1 MeV H^- Accelerator at JAEA for ITER NB", *1st International Symposium on Negative Ions, Beams and Sources*, Aix-en-Provence, AIP conference proceedings **1097** 335 (2009)
- [37] H.P.L. de Esch *et al*, "Results of the SINGAP Neutral Beam Accelerator Experiment at JAEA", *1st International Symposium on Negative Ions, Beams and Sources*, Aix-en-Provence, AIP conference proceedings **1097** 353 (2009)
- [38] L. Svensson *et al*, "Experimental results from the Cadarache1 MV test bed with SINGAP accelerators", *Nucl. Fusion* **46**, S369–S378 (2006)
- [39] M. Kashiwagi *et al*, "R&D progress of the high power negative ion accelerator for the ITER NB system at JAEA", *Nucl. Fusion*, **49** 065008 (2009)
- [40] V.A. Zhiltsov *et al*, "The development of a negative ion beam plasma neutralizer for ITER NBI", *Nucl. Fusion*, **40** 509 (2000)
- [41] L.R. Grisham *et al*, "Lithium Jet Neutralizer to Improve Negative Ion Neutral Beam Performance", *1st International Symposium on Negative Ions, Beams and Sources*, Aix-en-Provence, AIP conference proceedings **1097** 364 (2009)
- [42] W. Chaibi *et al*, "Photo-neutralization of Negative Ion Beam for Future Fusion Reactor", *1st International Symposium on Negative Ions, Beams and Sources*, Aix-en-Provence, AIP conference proceedings **1097** 385 (2009)
- [43] Elizabeth Surrey *et al*, "Gas heating in the neutralizer of the ITER neutral beam injection systems", *Nucl. Fusion*, **46** S360–S368 (2006)
- [44] Elizabeth Surrey *et al*, "Beam Induced Effects in the ITER Electrostatic Residual Ion Dump", *1st International Symposium on Negative Ions, Beams and Sources*, Aix-en-Provence, AIP conference proceedings **1097** 402 (2009)
- [45] L. Rossi *et al*, "Study of plasma formation within the electrostatic residual ion dump proposed for the HNB injectors of ITER", *Nucl. Fusion*, **49** 015002 (2009)

BIBLIOGRAPHY

- [46] T. Minea *et al*, "OBI-3 Code Description and Self-consistent simulation of the neutralizer and E-RID for ITER", *Fusion for energy report*, F4E-2009-GRT-032, Task 6-2, (2011)
- [47] P.L. Mondino *et al*, "ITER neutral beam system", *Nucl. Fusion*, **40** 501 (2000)
- [48] D. Boilson *et al*, "Long pulse operation of the KAMABOKO III negative ion source", *Review of Scientific Instruments*, **73**, 2, 1093 (2002)
- [49] R. Hemsworth *et al*, "Development of the long pulse negative ion source for ITER", *Proc. AIP Con.*, **763**
- [50] E. Speth *et al*, "Overview of the RF source development programme at IPP Garching", *Nucl. Fusion*, **46** S220–S238 (2006)
- [51] U. Fantz *et al*, "Spectroscopy—a powerful diagnostic tool in source development", *Nucl. Fusion*, **46** S297–S306 (2006)
- [52] A. Staebler *et al*, "Development of a RF-driven ion source for the ITER NBI system", *Fusion Engineering and Design*, **84** 265–268 (2009)
- [53] M. Bacal "Physics aspects of negative ion sources" *Nucl. Fusion* **46**, S250-S259, (2006)
- [54] R.K. Janev "Elementary Processes in Hydrogen-Helium Plasma", (1987)
- [55] D. Riz and J. Pamela, "Modeling of negative ion transport in a plasma source", *Review of Scientific Instruments*, **69**, 2 (2002)
- [56] R. Gutser and D. Wunderlich, "Overview on Modelling Activities at IPP", *Padua, 23/03/09, CCNB meeting*, (2009)
- [57] P. Franzen *et al*, "Status and plans for the development of a RF negative ion source for ITER NBI", *Fusion Engineering and Design*, **74**, 351–357, (2005)
- [58] E. Speth *et al*, "Development of a RF source for ITER NBI: First results with D^- operation", *Fusion Engineering and Design*, **74**, 279–282, (2005)
- [59] B. Heinemann *et al*, "Large-area high-transparency extraction system for negative ion", *Proceeding of the 20th Symposium on Fusion Technology*, Marseille, (1998)
- [60] O. Vollmer *et al*, "Commission and performance of the new ASDEX Upgrade neutral beam injector", *Proceeding of the 20th Symposium on Fusion Technology*, Marseille, (1998)
- [61] W. Kraus *et al*, "Long pulse large area beam extraction with a rf driven H^-/D^- source", **79**, 02C108, (2008)
- [62] B. Heinemann *et al*, "Design of the half-size ITER neutral beam source for the test facility ELISE", **84**, 915–922, (2009)

BIBLIOGRAPHY

- [63] W. Kraus *et al*, "The development of the RF driven negative ion source for neutral beam injectors", *Proceeding of the 14th International Conference on Ion Sources*, Giardini Naxos, Italy (2011)
- [64] G.J.M. Hagelaar *et al*, "Model of an inductively coupled negative ion source: I. General model description", *Plasma Sources Sci. Technol.* **20**, 015001, (2011)
- [65] J.P. Boeuf *et al*, "Model of an inductively coupled negative ion source: II. Application to an ITER type source", *Plasma Sources Sci. Technol.* **20**, 015002, (2011)
- [66] W.B. Hermannsfeld *et al*, "Electron Trajectory Program, SLAC Report", *Stanford Linear Accelerator Center*, SLAC-226, (1979)
- [67] J. Pamela *et al*, "A model for negative ion extraction and comparison of negative ion optics calculations to experimental results", *Rev. Sci. Instrum.*, **62**, 1163, (1991)
- [68] V. Antoni *et al*, "Optimization of the Accelerators for the ITER Neutral Beam Injector Project", *Plasma and Fusion Research: Regular Articles*, **5**, S1014, (2010)
- [69] H.P.L. de Esch *et al*, "Aperture Size Effect on Extracted Negative Ion Current Density", *1st International Symposium on Negative Ions, Beams and Sources*, Aix-en-Provence, AIP conference proceedings **1097** 309 (2009)
- [70] P. Agostinetti *et al*, "Design of a low voltage, high current extraction system for the ITER Ion Source", *1st International Symposium on Negative Ions, Beams and Sources*, Aix-en-Provence, AIP conference proceedings **1097** 325 (2009)
- [71] R. Gutser *et al*, "Simulation for the generation and extraction of negative hydrogen ions in RF-driven ion sources", *1st International Symposium on Negative Ions, Beams and Sources*, Aix-en-Provence, AIP conference proceedings **1097** 297 (2009)
- [72] R. Gutser *et al*, "Negative hydrogen ion transport in RF-driven ion sources for ITER NBI", *Plasma Phys. Control. Fusion*, **51** 045005 (2009)
- [73] R. Gutser *et al*, "Transport of negative hydrogen and deuterium ions in RF-driven ion sources", *Plasma Phys. Control. Fusion*, **52** 045017 (2010)
- [74] P. Spadtke and S. Wipf, *GSI Report*, 89-09, (1989)
- [75] F. Taccogna *et al*, "Negative-Ion-Source Modeling: From Expansion to Extraction Region", *IEEE Trans. Plasma Sci.* **36**, 1589 (2008)
- [76] F. Taccogna *et al*, "Modeling of a negative ion source II. Plasma-gas coupling in the extraction region", *Phys. Plasmas* **15** 103502 (2008)
- [77] F. Taccogna *et al*, "Plasma structure in the extraction region of a hybrid negative ion source", *1st International Symposium on Negative Ions, Beams and Sources*, Aix-en-Provence, AIP conference proceedings **1097** 65
- [78] C.K. Birdsall and A. B. Langdon, "Plasma Physics via Computer Simulation", McGraw-Hill, New York, (1985)

BIBLIOGRAPHY

- [79] M. Turek *et al*, "Simulations of negative ion extraction from a multi-aperture ion source in the presence of the magnetic filter", *Vacuum* **83** S256–S259 (2009)
- [80] M. Turek *et al*, "Numerical model for extraction of ions from plasma", *General Experimental Techniques* **52** 90-98 (2009)
- [81] A. Pyszniak *et al*, "Extraction of Ions from a Plasma Source and Formation of Beams", *Laboratory techniques* **50** 552-556 (2007)
- [82] S. Mochalsky, A. Lifschitz and T. Minea, "3D modeling of negative ion extraction from a negative ion source", *Nucl. Fusion* **50** 105011 (2010)
- [83] S. Mochalsky, A. Lifschitz and T. Minea, "Modeling of the negative ions extraction from a hydrogen plasma source. Application to ITER Neutral Beam Injector", *19th International Symposium on Plasma Chemistry - Proceedings*, Bochum (2010)
- [84] E.F. Kaasschieter, "Preconditioned conjugate gradients for solving singular system" *J. of Comput. and Appl. Math.* **24** 265-275 (1988)
- [85] R. Courant, K.O. Friedrichs, and H. Levy, "Über die partiellen Differenzgleichungen der mathematischen Physik", *Math. Ann.*, **100** 32–74 (1928)
- [86] R.W. Hockney, J.W. Eastwood, "Computer Simulation Using Particles", *IOP Publishing book*, (1988)
- [87] C.K. Birdsall, "Particle-in-cell charged-particle simulations, plus Monte Carlo collisions with neutral atoms, PIC-MCC", *IEEE Transactions on Plasma Science*, **19** 65–85 (1991)
- [88] M.R. Hestenes and E. Stiefel, "Methods of conjugate gradients for solving linear systems", *J. Research Nat. Bur. Standards*, **49** 409–436 (1953)
- [89] D.N. Arnold, "A concise introduction to numerical analysis", *Lecture Notes, Penn State, MATH 597I–Numerical Analysis*, (2001)
- [90] J.R. Shewchuk, "An Introduction to the Conjugate Gradient Method Without the Agonizing Pain", *unpublished*, (1994)
- [91] A. Van der Sluis and H.A. Van der Vorst, "The rate of convergence of conjugate gradients", *Numer. Math.*, **48** 543-560 (1986)
- [92] Z. Jomaa and C. Macaskill, "The embedded finite difference method for the Poisson equation in a domain with an irregular boundary and Dirichlet boundary conditions" *J. Comput. Phys.* **202** 488 (2005)
- [93] F. Gibou *et al*, "A Second-Order-Accurate Symmetric Discretization of the Poisson Equation on Irregular Domains", *J. Comput. Physics* **176** 205 (2002)
- [94] R. Gutser, "Overview on Modelling Activities at IPP", *Padua*, 23/03/2009
- [95] J. Boris, *Proc. the 4th Conf. on Numerical Simulation of Plasmas*, Washington DC, NRL 3–67 (1971)

BIBLIOGRAPHY

- [96] D. Potter, "Computational Physics", London, (1973)
- [97] F. Chen, "INTRODUCTION TO PLASMA PHYSICS AND CONTROLLED FUSION", *Plenum Press*, (1984)
- [98] P. Burger, "Elastic Collisions in simulation one-dimensional plasma diodes on the computer", *Phys. Fluids* **10**, 658-666 (1967)
- [99] T. Takizuka and H. Abe, "A binary collision model for plasma simulation with a particle code", *Journal of Computational Physics*, **25** (3), 205–219, (1977)
- [100] K. Nanbu, "Probability theory of electron-molecule, ion-molecule, molecule-molecule, and Coulomb collisions for particle modeling of materials processing plasmas and cases", *IEEE Transactions on Plasma Science*, **28** (3), (2000)
- [101] J. M. Rax, "Physique des plasmas", *Paris*, (2005)
- [102] <http://www-amdis.iaea.org/ALADDIN/collision.html>
- [103] R. Celiberto *et al*, *Atomic Data and Nuclear Data Tables* **77** 161–213 (2001)
- [104] C.F. Barnett *et al*, *Atomic Data for Fusion. Volume 1: Collisions of H, H₂, He, and Li Atoms and Ions with Atoms and Molecules*, ORNL-6086 (1990)
- [105] Yu. Belchenko *et al* "A powerful injector of neutrals with a surface-plasma source of negative ions" *Nucl. Fusion* **14** 113 (1974)
- [106] Elke Taute, "Auger Neutralization of Fast Ions at Surfaces", *Physica Status Solidi (b)*, **142**, 2, 437-443 (1987)
- [107] Marthe Bacal, "Effect of positive ions incident on the caesiated converter of a negative ion source with energy of tens of eV", 14th *International Conference on Ion Sources*, 12-16 September, Giardini Naxos, Italy, (2011)
- [108] M. Seidl *et al*, "Negative surface ionization of hydrogen atoms and molecules", *Appl. Phys.*, **79**, 2896 (1996)
- [109] Yu. Belchenko *et al*, "Negative ion production in multicusp sources", *Rev. Sci. Instr.* **64** 1385 (1993)
- [110] R. Gutser *et al*, "Work function measurements during plasma exposition at conditions relevant in negative ion sources for the ITER neutral beam injection", *Rev. Sci. Instr.* **82** 023506 (2011)
- [111] J. Pelletier *et al*, "Negative surface ionization: Intense halogen ion source" *J. Appl. Phys.* **50** 4517 (1979)
- [112] Message Passing Interface Forum. MPI: A Message-Passing Interface Standard, *Technical report* ver. **1.1**, www.mpi-forum.org, (1995)
- [113] M. Snir *et al*, "MPI – The Complete Reference, Volume 1, The MPI Core (second edition)" , *Cambridge, MA: MIT Press* (1998)

BIBLIOGRAPHY

- [114] P. Pacheco *et al*, "Parallel Programming with MPI", *Morgan Kaufmann; 1st edition* (1996)
- [115] M. Bacal *et al*, "The Negative Ion Mean Free Path And Its Possible Implication", *Second International Symposium on Negative Ions, Beams and Sources*, Takayama, Japan, (2010)
- [116] L.P. Block "A double layer review", *Astr. and Space Sci.* **55** 59-83 (1978)
- [117] E. Ahedo, "Theory of a Stationary Current-Free Double Layer in a Collisionless Plasma", *Phys. Rev. Lett.* **103**,135002 (2009)
- [118] A. Meige *Ph.D Thesis* "Numerical modeling of low-pressure plasmas: applications to electric double layers", Australian National University (2006)
- [119] F. Taccogna *et al*, "Modeling of a negative ion source. III. Two-dimensional structure of the extraction region" *Phys. of Plasmas* **17** 063502 (2010)

Internet sites:

1. <http://www.ipp.mpg.de/ippcms/eng/index.html>
2. <http://www-fusion-magnetique.cea.fr>
3. <http://www-amdis.iaea.org/ALADDIN/collision.html>